DEVELOPMENTS OF ATOMIC MAGNETOMETER AND APPLICATIONS IN MAGNETIC RESONANCE IMAGING

A Dissertation
Presented to
the Faculty of the Department of Chemistry
University of Houston

In Partial Fulfillment
of the Requirements for the Degree
Doctoral of Philosophy

By
Songtham Ruangchaithaweesuk
August 2013

DEVELOPMENTS OF ATOMIC MAGNETOMETER AND APPLICATIONS IN MAGNETIC RESONANCE IMAGING

_____

Songtham Ruangchaithaweesuk

APPROVED:

_____

Dr. Shoujun Xu, Chairman

Department of Chemistry

_____

Dr. Angela Moeller

Department of Chemistry

_____

Dr. Allan Jacobson

Department of Chemistry

_____

Dr. Steven Baldelli

Department of Chemistry

_____

Dr. Haibing Peng

Department of Physics

_____

Dean, College of Natural Sciences and Mathematics

Acknowledgements

I would like to thank my advisor, Assistant Professor Dr. Shoujun Xu for his continuous support, suggestions, assistance, encouragement, and kindness throughout my graduate career. His knowledge and ideas have been a great resource and inspiration.

I am grateful to Faculty members at the Department of Chemistry, College of Natural Science and Mathematics, University of Houston for providing the great knowledge in chemistry and made me feel that University of Houston is a great place to study in. I am thankful to the staff of the chemistry department for all the time and effort they have spent supporting my research and easing my work, in particular, Mark Bushman, for all the pieces that I could not machine myself.

I would like to express my appreciation to all of my great colleagues that I have been working with. Dr. Li Yao, a postdoc, has always been there to help me out even though we worked on different projects for most of the time. All the help from him is priceless to me. I would like to acknowledge other former and current members of my research group for their collaborate, support and good-fellowship over the years, including Nissa Garcia, Dindi Yu, Bian Hu, Nebiyu Sermollo, Lashan DeSilva, Vasudeva Chintamsetti, Lecheng Zhang, Yi-Ting Chen, Te-Wei Tsai and Qiongzheng Hu.

Finally, my love and thanks go to my parents, my brother and my aunts for their love, support and encouragement throughout my life. Nothing that I have accomplished would have been possible without them, and I dedicate this dissertation to them.

DEVELOPMENTS OF ATOMIC MAGNETOMETER AND APPLICATIONS IN MAGNETIC RESONANCE IMAGING

An Abstract of a Dissertation
Presented to
the Faculty of the Department of Chemistry
University of Houston

In Partial Fulfillment
of the Requirements for the Degree
Doctoral of Philosophy

By
Songtham Ruangchaithaweesuk
August 2013

Abstract

We report the design and optimization of a highly sensitive cesium atomic magnetometer with a sensitivity of 80 fT/(Hz)$^{1/2}$ for dc magnetic fields. Quantitative measurements using optically detected magnetic resonance imaging (MRI) for flow inside porous metals will be demonstrated. Flow profiles and images were obtained for a series of porous metals with different average pore sizes. The signal amplitudes and spatial distributions were compared. A clogged region in one of the samples was revealed using optically detected MRI but not optical imaging or scanning electron microscopy. These applications will significantly broaden the impact of optically detected MRI in chemical imaging and materials research. However, MRI in an ultralow magnetic field usually has poor spatial resolution compared to its high-field counterpart. The concomitant field effect and low signal level are among the major causes that limit the spatial resolution. A novel imaging method, a zoom-in scheme, will be demonstrated to achieve a reasonably high spatial resolution of 0.6 mm × 0.6 mm without suffering the concomitant field effect. This method involves multiple steps of spatial encoding with gradually increased spatial resolution but reduced field-of-view. This method takes advantage of the mobility of ultralow-field MRI and the large physical size of the ambient magnetic field. We also demonstrate the use of a unique gradient solenoid to improve the efficiency of optical detection with an atomic magnetometer. The enhanced filling factor improved the signal level and consequently facilitated an improved spatial resolution.

Contents

Chapter 1 1

Introduction 1

Chapter 2 4

Atomic magnetometry 4

2.1 Linear magneto-optical effects 5

2.1.1 Faraday effect 5

2.1.2 Macaluso-Corbino effect 7

2.2 Nonlinear magneto-optical effect 9

2.2.1 Optical pumping 9

2.2.2 Radiation trapping and quenching 11

2.2.3 Spin exchange relaxation 11

2.3 Atomic magnetometers 12

2.4 Sensitivity of atomic magnetometers 17

Chapter 3 22

Cs atomic magnetometer instrumentation 22

3.1 Cs atomic magnetometer instrumentation 22

3.1.1 Paraffin-coated Cs vapor cells 23

3.1.2 Magnetic shields 25

3.1.3 Internal coils 26

3.1.4 Diode laser and optical layout....26
3.1.5 Laser lock....28
3.1.6 Signal detection, electronics and communications system....31
3.2 Characterization of the instrument....33
3.2.1 Absorption of Cs....33
3.2.2 Nonlinear magneto optical resonance....35
3.2.3 Instrumental calibration....36
3.3 A new design of atomic magnetometer....37
3.3.1 Divider....37
3.3.2 Cs cell....37
3.3.3 Magnetic shields and internal coils....40
3.3.4 Characterization of the instrument....41
3.4 Detection schemes for NMR and MRI....43
3.4.1 Remote detection....43
3.4.2 Radio frequency (RF) detection scheme....44
3.5 Remote detection setup....45
3.5.1 Encoding region....46
3.5.1.1 RF excitation coils....47
3.5.1.2 Gradient coils....48
3.5.1.3 Pulse sequences....51
3.5.2. Detection region....53
3.5.2.1 Piercing solenoid, bias magnetic field and sample polarization....53

Chapter 4 56
Applications of optically detected MRI for penetration in metal 56
4.1 Motivation of the study 56
4.1.1 Remote detection scheme 59
4.2 Basic concepts of MRI 61
4.2.1 Nuclear magnetic resonance 61
4.2.2. Relaxation time constants: T_1 and T_2 63
4.2.3 Detection of an NMR signal 65
4.2.4 Encoding spatial information in MRI 66
4.3 Experimental methods 69
4.4 Results and discussion 69
Chapter 5 77
High–resolution optically detected MRI in an ambient magnetic field 77
5.1 Motivation of the study 77
5.2 An Image artifact in very low field MRI: Concomitant effect 78
5.3 Experimental methods 80
5.4 Results and discussion 84
Chapter 6 95
Selective polarization and nuclear spin relaxation for different fluids 95
6.1 Selective polarization 95
6.1.1 Motivation of the study 95
6.1.2 Experiment 96
6.1.3 Discussion 102
6.2 Nuclear spin relaxation for different fluids in porous materials 102

Chapter 7 105

Conclusion 105

Appendix A 107

MATLAB codes 107

A1. Flow profiles 107

A2. 1D- and 2D-Imaging 111

A3. 2D-Movies 119

A4. Off-axis magnetic field (parallel) 127

A5. Off-axis magnetic field (perpendicular) 130

Appendix B 132

Off-axis field of a current loop 132

Bibliography 134

List of Figures

Figure 2.1 Faraday effect. When linear-polarized light interacts with a medium in the presence of a longitudinal magnetic field, its polarization is rotated by an angle φ. 5

Figure 2.2 An F=1 → F' = 0 atomic transition. F, F' are the total angular momenta of the lower and upper states of the transition, respectively. In the presence of a longitudinal magnetic field, the different circular components of the linearly polarized light field couple to different ground state Zeeman sublevels. For this reason, the Zeeman effect creates a difference in the indices of refraction for the circular components -leading to a phase shift between the circular components of the light and consequently optical rotation of linearly polarized light. 8

Figure 2.3 Optical pumping of the electronic spins of the alkali atoms (neglecting the hyperfine ($F = I + J$) couplings between the electronic and nuclear spins of the alkali metal atoms). 11

Figure 2.4 Electronic states of Cs atoms with hyperfine structure (not to scale). Shown above are the ground state $^2S_{1/2}$, and the two lowest excited states, $^2P_{1/2}$ and $^2P_{3/2}$. In the presence of a magnetic field, each hyperfine F level generates $2F$+1 sublevels (Zeeman splitting). 15

Figure 2.5 Schematic of a typical atomic magnetometer. Atomic magnetometers determine the intensity or polarization change of a laser (probe) beam after it interacts with spin-polarized alkali atoms in the presence of a magnetic field. The polarization of the laser is a function of its modulation frequency, which corresponds to the magnetic field to be measured. 16

Figure 3.1 Optical layout for Cs atomic magnetometer 22

Figure 3.2 Cs cells and magnetic shield. 24

Figure 3.3 Double-pass arrangement. 27

Figure 3.4 DAVLL box 29

Figure 3.5 a) The schematic of a DAVLL system is illustrated. A small portion of the laser beam is directed to the locking apparatus where the Cs vapor cell is located inside. The light then passes through the quarter-wave plate followed by a polarizing prism which separates the right and left circular polarized beams. These are directed to the two photodetectors (PD) to analyze the intensity of the laser power of the polarized beams.. 30

Figure 3.6 Magneto-optical rotation in DAVLL.....30

Figure 3.7 LABVIEW interface for GPIB communication and frequency modulation. 32

Figure 3.8 Absorption of Cs sensor of the D1 transition. 34

Figure 3.9 The resonance signals, in-phase and out-of-phase, of two Cs magnetometers. 35

Figure 3.10 Square wave signals ranging from -0.1 V to 0.1 V for signal calibration. 36

Figure 3.11 a) The photo of 4-layer magnetic shields. A plastic divider separates two regions of the shield. b) The Cs vapor cell is mounted on a platform located at the center of the magnetic shield. 38

Figure 3.12 a) A new built atomic magnetometer with new features. b) Internal magnetic caps with different port shapes. 39

Figure 3.13 Schematic of the design for a coil holder located inside the magnetic shield. 40

Figure 3.14 Magneto-optical resonance profiles for calibrating magnetic fields.....42

Figure 3.15 The sensitivity of the atomic magnetometer. 42

Figure 3.16 Remote detection of MRI with an atomic magnetometer. 43

Figure 3.17 RF detection scheme with atomic magnetometer. A long solenoid provides a leading field B_0 for the sample nuclei, whereas the alkali atoms do not experience this field. A tunable ac field B_b is applied to the atomic magnetometer so that the atomic precession matched the nuclear precession in order to observe resonance. 45

Figure 3.18 a) An excitation coil. b) Direction of current flow. 47

Figure 3.19 Maxwell coils to produce a linear field gradients in B_0 along the z-axis. 48

Figure 3.20 Golay coils to produce a linear gradient field in B_0 along the x- and y-axes.....49

Figure 3.21 Gradient coils wound around an acrylic tube. Length and dimensions are measured based on the efficiency parameters.....49

Figure 3.22 a) Tecmag LF1 Apollo unit for sending rf pulses and phase encoding. b) RF amplifier model HP 461A. 51

Figure 3.23 Pulse sequences. a) π pulse is used to invert the spins of the sensor medium to obtain the flow profile. b) Phase encoding pulse sequence for 1D and 2D imaging.....52

Figure 3.24 Detection region of the remote detection scheme. The piercing solenoid (top) generates the leading field (B_{leading}). Detection axis is defined by a bias field (B_{bias}). The two Cs cells experience the magnetic field introduced by the sample (B_{sample}). The copper sample holder (bottom) has two tubes inserted, for the detection of nuclear magnetization. 53

Figure 3.25 Remote detection setup. The fluid sample driven by a micropump (not shown) flows continuously through three consecutive regions: Prepolarization magnet, encoding region, and detection region. The sample is recycled to the reservoir. 54

Figure 3.26 Pulse sequences for MR imaging of remote detection experiment.....55

Figure 4.1 Remote detection of MRI. 59

Figure 4.2 Zeeman Energy Splitting. Interaction between protons and the external magnetic field B results in splitting the energy levels. For a large number N of protons, $N\uparrow$ will have s = -½, and $N\downarrow$ will have s = ½, leading to corresponding energies $E\uparrow$ and $E\downarrow$. In the equilibrium state, the ratio of the number of protons populating the two energy levels $N\uparrow/N\downarrow$ is governed by the Boltzmann distribution.....62

Figure 4.3 (a) The three-dimensional motion of the magnetization vector. B_0 is the static magnetic field along the z direction, M_0 is the thermal equilibrium state of M and M_L^0 and M_T^0 represent longitudinal and transverse components of M at time t = 0, respectively. (b) The components of the magnetization vector as functions of time.....66

Figure 4.4 After each excitation, the magnetic resonance signal is acquired as a function of time and recorded as a row of numbers in a data array known as k-space. The process is repeated with phase-encoding gradients of incrementally different amplitudes, and each time the

signal is recorded as an adjacent line in k-space. After all of the k-space data have been collected, the image is extracted by means of a 2D Fourier transform. 68

Figure 4.5 Optical images (a-d) and SEM images (e-h) of the four porous metals. 70

Figure 4.6 Flow profiles for the porous steel samples and the blank sample..... 71

Figure 4.7 MR images of the flow inside the blank and 100-μm steel samples. (a) The pulse sequence (b) 2D Images. The inset in grey depicts the axes and flow direction. 72

Figure 4.8 One-dimensional images for the blank and 100-μm steel samples at 0.7 s (a) and 1.2 s (b). 74

Figure 4.9 Optically detected MRI depicts a clogged region in the 0.5-μm steel sample. 75

Figure 5.1 Experimental details: (a) Schematic of the zoom-in method. The Left panel shows the ordinary imaging method with no zoom-in. The Right panel shows the zoom-in method, which consists of two 10 × 10 grids that achieve the same spatial resolution as the ordinary 100 × 100 grid, but only for a region of interest (in green). (b) The coil stack is mounted on a two-dimensional translation stage; the orientation of the coil stack is aligned with the ambient magnetic field B_0. (c) Scheme showing the optically-detected ultralow-field MRI of the flow. 81

Figure 5.2 Imaging phantom and pulse sequence: (a) Drawing of the phantom with two flow channels with 0.6 mm edge-to-edge spacing. Unit: mm. (b) Pulse sequence. $G^{PE}(x, y)$: Phase encoding gradient field along x- and y- axes. The atomic magnetometer measures the magnetization downstream, as indicated by the red line. 83

Figure 5.3 The gradient solenoid used to improve the detection efficiency. 84

Figure 5.4 Results of using the zoom-in method for ultralow-field MRI in an ambient magnetic field: (a) MR image before zoom-in, in which the green box indicates half of the FOV. (b) Zoom-in MR image after the coil stack was moved to the left by 2 mm and the gradient field on the horizontal axis was doubled. The scale bars indicate 1 mm. 85

Figure 5.5 Zoom-in MR image acquired by doubling the gradient field along both axes, with scale bars indicating 1 mm. 86

Figure 5.6 MR image to show the concomitant field effect, with gradients 7 μT/cm for both axes, with scale bars indicating 1 mm. 87

Figure 5.7 Improvement of the detection efficiency with a gradient solenoid: (a) magneto-optical resonance profiles with and without the gradient solenoid; (b) water flow profile measured by the atomic magnetometer with a gradient solenoid. 90

Figure 5.8 Magnetic field mapping of a plane parallel to the gradient solenoid. The estimate amplitude at the atomic sensor, on the center right edge, is 3 nT. 91

Figure 5.9 Magnetic field mapping of a plane perpendicular to the gradient solenoid. This map exhibits consistent estimate amplitude at the atomic sensor (at the center). 91

Figure 5.10 Comparison of the filling factors for (a) a piercing solenoid and (b) a gradient solenoid. The blue bars indicate the average distances between the sample and the atomic sensor. The detection axis is determined by the indicated propagation direction of the laser. 93

Figure 6.1 Selective polarization. 96

Figure 6.2 The sample holder consists of two input channels and one output channel. Polarized water was flown through channel 1, whereas nonpolarized water was flown through the side way, channel 2. The flow direction is along *z*-axis.. 97

Figure 6.3 MR images along (a) *yz*- and (b) *xz*-planes of selectively polarized water in the sample holder with bypass channel. 99

Figure 6.4 MR images along (a) *xy*- and (b) *xz*-planes of selectively polarized water in the sample holder with bypass channel with 100-μm porous steel sample. 100

Figure 6.5 MR images of selectively polarized water along *xy*-plane in (a) original sample holder (b) bypass holder and (c) bypass holder with 100-μm porous steel sample. 101

Figure 6.6 Flow profiles of water and hexane in a porous steel sample. 104

List of Tables

Table 4.1 Void volume, porosity, and average pore size of the porous metals 71

Table 6.1 Comparison of signal amplitudes of the sample holder, the sample holder with bypass channel and with 100 μm porous steel sample inserted. 98

Table 6.2 Water and hexane signals vs. pore size.....103

Chapter 1

Introduction

Detection and measurement of magnetic fields have been used extensively in a wide range of applications, including medicine, mineral and oil exploration, fundamental and advanced physics experiments. Detection of nuclear polarization, i.e., nuclear magnetic resonance (NMR) and magnetic resonance imaging (MRI) have been developed to overcome limitations in order to achieve optimal sensitivity.

Conventional NMR and MRI involve high magnetic fields and intense radio frequency (rf) pulses produced by superconducting magnets. However, measurements performed using bulky superconducting magnets, one of the major components of traditional MR devices, are impractical or inconvenient for experiments conducted in remote areas. Alternatively, measurements can be implemented at the low-field regime (<~1 mT), which will eliminate the need for a large magnet for detection [1, 3]. Low-field MRI is advantageous compared to high-field in terms of portability, sample size, magnetic susceptibility effects and power consumption.

The consequence of using a low magnetic field for MRI is that a sensitive detection technique must be implemented. Conventional Faraday-induction detection using a radio frequency coil has a poor sensitivity in low-field because the sensitivity is proportional to the magnetic field strength [4-9]. Using inductive coils, which usually have a small number of turns, is not preferable in a low field regime.

Superconducting quantum interference devices (SQUIDs), which measure magnetic flux passing through the superconducting loop and operate at liquid helium temperature (4 K), have been used for ultralow-field MRI by several research groups [10–14]. SQUID magnetometers have enabled NMR experiments as ultrahigh-sensitive magnetic field detectors with high sensitivity ~1fT/$(Hz)^{1/2}$ [15, 16]. Many applications of SQUID magnetic field sensors have been used in biomagnetic research works to detect weak magnetic fields produced by human brain (magnetoencephalography, MEG) [17], or other organs. However, SQUIDs require cryogenics, to maintain the superconducting state to generate strong magnetic fields which also leads to high cost and limits the portability to remote areas. An anisotropic magnetoresistive (AMR) detection technique has also demonstrated NMR detection at low magnetic field [18]. It provided poorer sensitivity, on the order of 100 pT/$(Hz)^{1/2}$, at frequencies above 1 kHz. However, a sensitivity of 32 pT/$(Hz)^{1/2}$ was achieved when cryogenic was used to couple with AMR [19]. In addition to SQUIDs, sensitive magnetic field sensors using diamonds with nitrogen-vacancy defects have also been reported [20-22].

Alternatively, atomic magnetometry has long been used for precise measurement of magnetic fields and fundamental physics parameters [23, 24]. The application scope for atomic magnetometry has been significantly expanded in the

past several years following a sensitivity boost to the femtotesla range and beyond [25–28]. The magnetic field due to sample nuclear polarization is directly measured, with a theoretically projected sensitivity on the order of 0.01 $fT/(Hz)^{1/2}$ under optimal conditions [26]. Disciplines that can use sensitive atomic magnetometers include magnetic resonance imaging (MRI) [29, 30], nuclear magnetic resonance (NMR) [31-34], nuclear quadrupole resonance [35], magnetoencephalography [36, 37], and magnetocardiography [38-40]. Furthermore, several new techniques based on atomic magnetometry have recently been developed, including scanning magnetic imaging and force-induced remnant magnetization spectroscopy, which have extensive applications in molecular and cellular imaging [41–43]. Atomic magnetometers have the advantages of operating at near ambient temperatures [44-46]. With the aforementioned advantages of low-field detection, atomic magnetometry is therefore a promising MR detection technique.

In this dissertation, the design and optimization of the magnetometer using cesium atomic sensors in the earth's field (low-magnetic field) to study flow in porous materials will be presented. A significant portion of my work in improving detection sensitivity for magnetic resonance imaging (MRI) in order to overcome some of the limitations associated with high-field NMR/MRI instrument will be discussed.

Chapter 2

Atomic magnetometry

In this chapter, basic concepts of atomic magnetometry, which include the mechanisms contributing to magneto-optical rotation, linear and nonlinear magneto-optical effects, are presented. Other important information, which include optical pumping, radiation trapping and quenching, spin exchange relaxation, and the sensitivity of atomic magnetometers are also discussed.

2.1 Linear magneto-optical effects

2.1.1 Faraday effect

The Faraday effect, discovered by Michael Faraday in 1845, was the first experimental indication that light and electromagnetism are related. Magneto-optical effects occur when light interacts with a medium in the presence of a magnetic field. The rotation of the plane of polarization is proportional to the applied magnetic field in the direction of the beam of light.

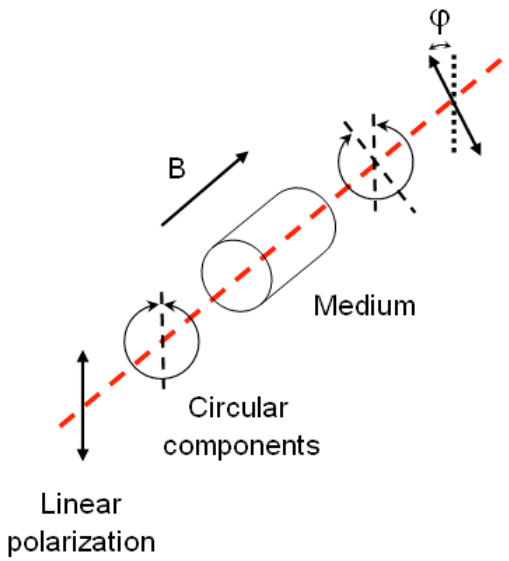

Figure 2.1 Faraday effect. When linear-polarized light interacts with a medium in the presence of a longitudinal magnetic field, *B*, its polarization is rotated by an angle φ.

The Faraday rotation occurs due to the difference in the indices of refraction for left- and right-circularly polarized light (σ^+ and σ^-, respectively) induced in the medium, which is cesium atomic vapor in our experiment, by the applied magnetic field (Figure 2.1). A light field propagating in the *z* direction can be explained as a superposition of optical eigenmodes (i.e., waves that traverse the medium without changing their state of polarization, experiencing only attenuation and phase shifts). The optical eigenmodes are determined by the symmetry properties of the medium.

The magnetic field is an axial vector, so its presence creates a preferred "handedness" in the system which manifests as a breaking of the symmetry between the two optical eigenmodes, left- and right-circularly polarized waves. This symmetry breaking allows different complex indices of refraction to arise for the circular components.

Linearly polarized light can be expressed as a coherent superposition of circular components, where the plane of light polarization is defined by the relative phase between the two circular components. For example,

$$\hat{\boldsymbol{\epsilon}}_x = \frac{1}{\sqrt{2}}(\hat{\boldsymbol{\epsilon}}_- - \hat{\boldsymbol{\epsilon}}_+) \qquad (2.1)$$

$$\hat{\boldsymbol{\epsilon}}_y = \frac{i}{\sqrt{2}}(\hat{\boldsymbol{\epsilon}}_+ + \hat{\boldsymbol{\epsilon}}_-) \qquad (2.2)$$

where $\hat{\boldsymbol{\epsilon}}_x$ and $\hat{\boldsymbol{\epsilon}}_y$ are unit vectors representing light linearly polarized along *x* and *y*, respectively, and $\hat{\boldsymbol{\epsilon}}_+$ and $\hat{\boldsymbol{\epsilon}}_-$ are unit vectors representing left- (σ^+) and right-circularly polarized (σ^-) light, respectively.

As the light propagates through the atomic vapor, the two circular components acquire a relative phase shift leading to rotation of the axis of light polarization by angle ϕ:

$$\phi = \frac{\omega \ell}{c} \cdot \mathrm{Re}\left(n^{+} - n^{-}\right) \qquad (2.3)$$

where ω is the frequency of the light field, l is the path length in the vapor, n^{+} *and* n^{-} are the complex indices of refraction for the circular components.

2.1.2 Macaluso-Corbino effect

About half a century after Faraday's discovery, Domenico Macaluso and Orso Corbino modified the Faraday's experimental setup and studied magneto-optical rotation in alkali vapors [47]. Their work was motivated by the recent discovery by Zeeman of the splitting of atomic spectral lines in magnetic fields. Macaluso and Corbino discovered that when the frequency of the incident light was tuned near an atomic resonance frequency, magneto-optical rotation was significantly enhanced and had a distinct resonant character. The Macaluso-Corbino effect can be illustrated as, for example, F=1 → F' = 0 atomic transition as shown in Figure 2.2.

Linearly polarized light incident on the sample can be decomposed into two counter-rotating circular components $\sigma^{\pm}$. In the absence of a magnetic field, the ground state M sublevels are degenerate and the optical resonance frequencies for σ^{+} and σ^{-} coincide. In the presence of a longitudinal magnetic field, the Zeeman sublevels of the ground state are shifted in energy by $g\mu BM$, where g is the Lande factor, μ is the Bohr magneton. This leads to a difference in resonance frequencies for

left- (σ^+) and right- (σ^-) circularly polarized light (circular birefringence). As a result, the plane of polarization rotates through an angle φ.

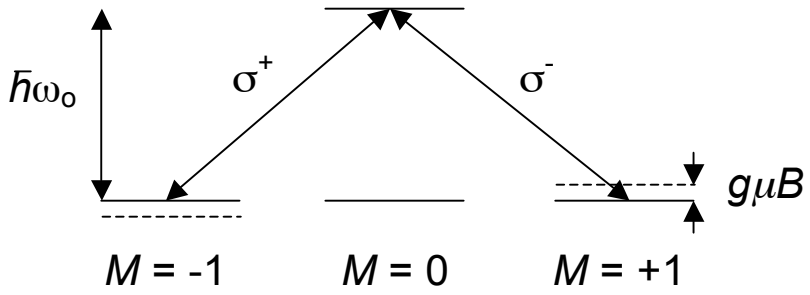

Figure 2.2 An F=1 → F' = 0 atomic transition. F, F' are the total angular momenta of the lower and upper states of the transition, respectively. In the presence of a longitudinal magnetic field, the different circular components of the linearly polarized light field couple to different ground state Zeeman sublevels. For this reason, the Zeeman effect creates a difference in the indices of refraction for the circular components, leading to a phase shift between the circular components of the light and consequently optical rotation of linearly polarized light.

The populations of the ground-state Zeeman sublevels that are split by a magnetic field are generally different according to the Boltzmann distribution. This leads to a difference in refractive indices for the corresponding light polarization components. This mechanism is termed the paramagnetic effect. For gaseous systems, this effect is relatively small compared to the other mechanisms. However, it can be dramatically enhanced by creating a nonequilibrium population distribution between Zeeman sublevels. This can be accomplished by optical pumping, a nonlinear effect that will be discussed in detail in the nonlinear magneto-optical rotation process in section 2.2.1.

2.2 Nonlinear magneto-optical effect

A nonlinear optical process is a process in which the optical properties of the medium depend on the light field itself. The light field can consist either of a single beam that both modifies the medium and probes its properties, or of multiple beams (e.g., a pump-probe arrangement). For nonlinear magneto-optical effect (NMOE), when an NMOE occurs, the properties of both the medium and the light are affected. The physical mechanisms that cause NMOE are the influence of light on the medium, detailing how the populations of and coherences between atomic states are changed (optical pumping), and the influence of the medium on the light, indicating how the light polarization is subsequently modified (optical probing). A single laser beam is used for both pumping and probing, these processes occur simultaneously and continuously.

2.2.1 Optical pumping

Optical pumping methods achieve highly non-Boltzmann population distributions by utilizing the quantum mechanical selection rules of angular momentum. It was first reported by Kastler [48] that circularly polarized light could be used to pump electronic spins of gaseous metal species into nonequilibrium population distributions. Later, a study in detail on optical pumping was given by Happer *et al*. [49] in 1972. Sensitive magnetometers require large atomic spin polarization to provide useful measurement signals. Optical pumping methods can be

used to obtain highly non-equilibrium spin polarizations, thereby increasing net magnetization by several orders of magnitude.

The thermal polarization of an ensemble of alkali atoms is given by

$$P = \tanh\left(\frac{g_s \mu_B B}{2kT}\right) \qquad (2.4)$$

where g_s~2 is the electron g-factor, μ_B is Bohr magneton, k is Boltzmann's constant. P obtained is too small ($P << 1$) to be measured by atomic magnetometer. Large nonthermal spin polarization, with P~1, can be obtained by optical pumping which transfer angular momentum from resonant light to the atoms.

In optical pumping process, the spins of unpaired electrons of alkali metal atoms are polarized with laser light (Figure 2.3). By applying circularly polarized light tuned to the D1 transition of the alkali metal, population can be selectively depleted from one of the m_J sublevels in the ground state (neglecting the hyperfine coupling with the nuclear spin of the metal), σ^+ light drives population from m_J = -½ in the ground state into m_J = ½ in the excited state. Collisions with other gas-phase species equalize the populations of the excited-state sublevels, equilibrating the relaxation rates to the ground m_J sublevels. The depletion of the ground m_J = - ½ sublevel (and subsequent accumulation of population in the ground m_J = ½ sublevel) rapidly reaches steady state, leaving the metal vapor electronically spin-polarized. Atoms in the ground m_J = ½ sublevel are forbidden from absorbing a photon because there is no level in the excited state with an additional +1 momentum. Hence, they remain in that level unless they experience some relaxation mechanism.

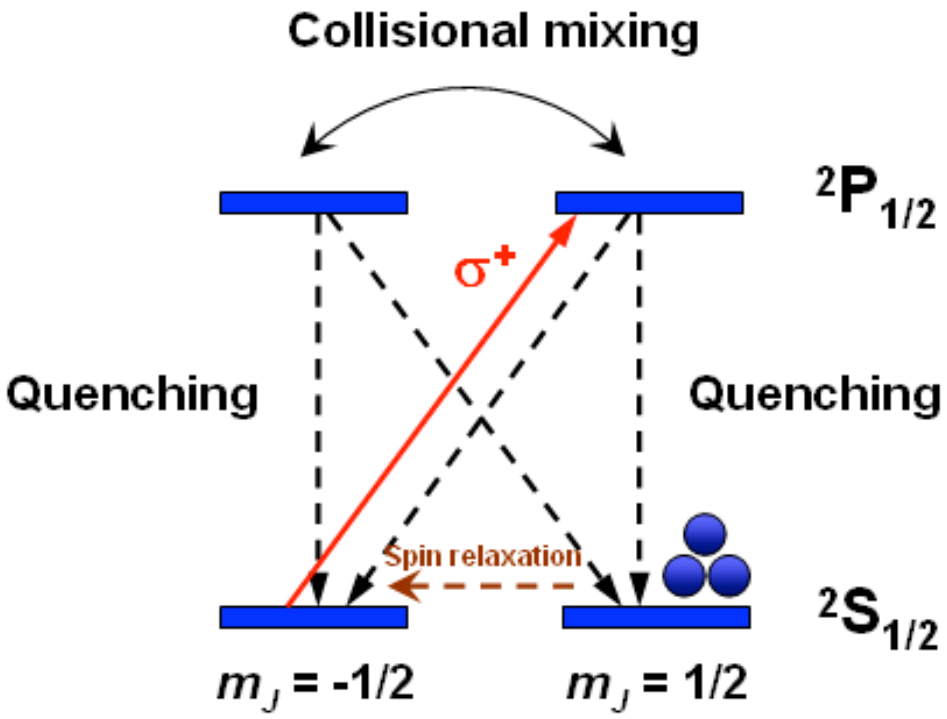

Figure 2.3 Optical pumping of the electronic spins of the alkali atoms (neglecting the hyperfine ($F = I + J$) couplings between the electronic and nuclear spins of the alkali metal atoms).

2.2.2 Radiation trapping and quenching

The presence of buffer gas, such as He or Ne, used to prevent wall collisions affects the efficiency of optical pumping. Collisions with buffer gas atoms depolarize the alkali atoms. Thus, there is very rapid collisional mixing between the Zeeman levels of the excited states that equalizes the populations of the levels.

Atoms that spontaneously decay back to the ground state emit a randomly polarized, resonance photon that can depolarize another atom if reabsorbed. In very dense alkali vapor, the probability of absorption is high. A phenomenon known as radiation trapping can occur in which reabsorption of spontaneously emitted photons limits the polarization of the alkali vapor. To prevent spontaneous decay a quenching gas, N_2, is added to the cell. During collisions between the excited alkali atoms and the quenching gas, atoms transfer their excess energy to the rotational and vibrational modes of the quenching gas molecules and decay back to the ground state without radiating a resonant photon.

2.2.3 Spin exchange relaxation

Another factor that limits the sensitivity of magnetometers is spin exchange relaxation, a mechanism which usually destroys the orientation of atomic spins. This can be avoided by using a high density of alkali atoms and a very low magnetic field. Under these conditions, decoherence due to spin-exchange collisions can be suppressed when the atoms exchange spin faster than their magnetic precession frequency. A spin-exchange relaxation-free (SERF) magnetometer reaches very high

magnetic field sensitivity by monitoring a high density vapor of alkali metal atoms precessing in a near-zero magnetic field [50]. SERF magnetometers are among the most sensitive magnetic field sensors and in some cases surpass the performance of SQUID detectors of equivalent size. A glass cell with a small volume of 1 cm^3 containing potassium vapor has been reported to show 1 $fT/(Hz)^{1/2}$ sensitivity and can theoretically become even more sensitive with larger volumes [26].

In atomic vapor cells with antirelaxation coating, two possible mechanisms may occur, transit and wall-induce Ramsey effects. In the transit effect, pumping and probing occur while atoms traverse along the single pass of beam. In the wall-induced Ramsey effect, atoms that are pumped leave the light beam for a certain amount of time undergoing many wall collisions around the cell before returning to the beam where the probe interaction occurs. Consequently, the time between pumping and probing is much longer in the wall-induced Ramsey effect compared to the transit effect, leading to the ultranarrow linewidths, which implies enhanced sensitivity.

The use of high buffer gas increases the travel time of the atoms to collide with the cell wall because the atoms experience diffusive motion. Thus, the atoms' mean free path λ in the buffer gas is comparable to or less than the dimensions of the cell.

2.3 Atomic magnetometers

Atomic magnetometers measure magnetic fields by using lasers to detect the interaction between alkali metal atoms in a vapor and the magnetic field. Most atomic magnetometers use a polarized alkali-metal vapor (K, Rb or Cs) as a sensor because

of the hydrogen-like electron configuration. In the presence of a magnetic field, which includes the magnetic field to be measured, the electronic states of the alkali undergo Zeeman splitting. A polarized laser beam, with near-resonance wavelength to one of the electronic transitions of the alkali, generates a coherent population in certain ground-state Zeeman sublevels.

In this study, a Cs atomic sensor was implemented. Cesium in its atomic state has just one valence electron and can be approximated by a one-electron-atom model. However, its nuclear properties are different from hydrogen and this leads to a different energy-level structure. There are 40 known isotopes of cesium in nature. The atomic masses of these isotopes range from 112 to 151. Cesium-133 is the only naturally occurring and only stable isotope of cesium. ^{133}Cs atomic vapor was used as an atomic sensor in this experiment. The two transitions, termed D1 and D2 lines, are shown in Figure 2.4. The optically pumped alkali atoms subsequently interact with a probe laser beam, which may be the same as the pump beam, and consequently modulate the polarization or amplitude of the beam. The modulation is a function of the magnetic field to be detected. The magnetic field produced by the sample is parallel to the propagation of the laser. Detection of the optical properties of the probe beam is therefore a measurement of the magnetic field.

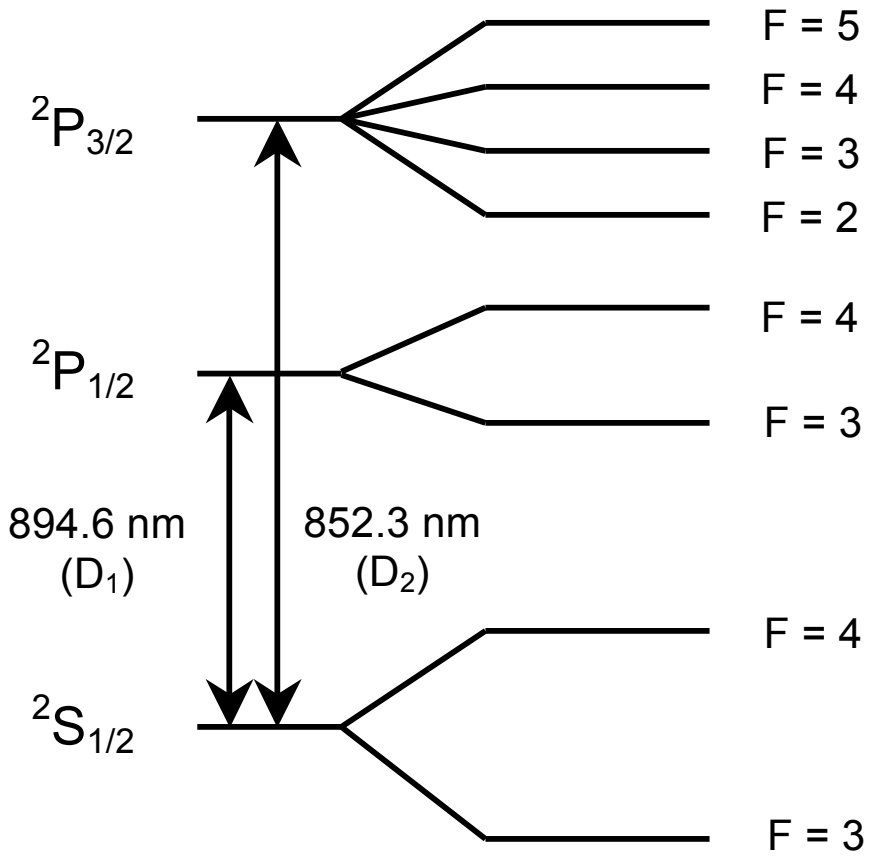

Figure 2.4 Electronic states of Cs atoms with hyperfine structure (not to scale). Shown above are the ground state $^2S_{1/2}$, and the two lowest excited states, $^2P_{1/2}$ and $^2P_{3/2}$. In the presence of a magnetic field, each hyperfine F level generates $2F+1$ sublevels (Zeeman splitting).

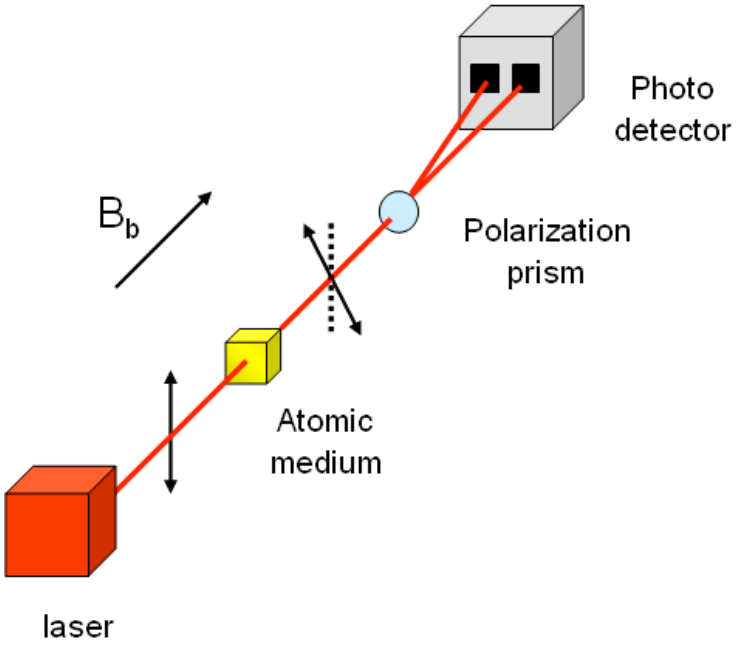

Figure 2.5 Schematic of a typical atomic magnetometer. Atomic magnetometers determine the intensity or polarization change of a laser (probe) beam after it interacts with spin-polarized alkali atoms in the presence of a magnetic field. The polarization of the laser is a function of its modulation frequency, which corresponds to the magnetic field to be measured.

The schematic of atomic magnetometry is shown in Figure 2.5. Atomic magnetometers are based on the magneto-optical effects that arise when a polarized laser beam passes through alkali atoms [45]. Bias field, B_b, is a small magnetic field used to define the detection axis of the atomic magnetometer. Consequently, the atomic magnetometer as shown is a vector magnetometer. B_s is the sample magnetic field to be measured, and $B_s << B_b$. For magnetometers operated in a near-zero magnetic field, no bias field is used. So, the detection axis is determined by the configuration of pump and probe lasers [26]. The polarization axis of the probe laser beam is rotated due to the linear dichroism of the polarized atoms [46]. The rotation angle is measured by the balanced polarimeter. That is, after the alkali cell, the beam is split by a polarizing beamsplitter set at 45^o to the initial polarization, resulting in two separate beams with the intensities as follow:

$$I_1 = I_o \sin^2 (\theta - \pi/4) \qquad (2.5)$$

$$I_2 = I_o \cos^2 (\theta - \pi/4) \qquad (2.6)$$

Such that $I_o = I_1 + I_2$, and the intensities are balanced when $\theta = 0$ and unbalanced otherwise. The optical rotation angle ϕ, $\phi << 1$, can be obtained from the following equation:

$$\phi = \frac{I_1 - I_2}{2(I_1 + I_2)} \qquad (2.7)$$

The resonance with atomic precession can be obtained by modulating the amplitude or frequency of the laser [51, 52]. When the resonance occurs, the sample magnetic field can be determined from the frequency according to the following equation:

$$\omega_L = \gamma(B_b+B_s) = \frac{g\mu_B}{\hbar(2I+1)}(B_b+B_s) \quad (2.8)$$

where ω_L is the Lamor frequency of the alkali atoms, γ is the atomic gyromagnetic ratio, g~2 is the electron g factor, μ_B is the Bohr magneton, I is the nuclear spin of the atom.

2.4 Sensitivity of atomic magnetometers

Atomic magnetometers contain alkali atoms within a glass cell, which is heated up to 200 ^oC, depending on the alkali species, to increase the saturated vapor density of the alkali atoms. Magnetometers are characterized by their sensitivity. To determine the precision of the device, the sensitivity of an atomic magnetometer, δB, is determined by

$$\delta B \approx \frac{1}{\gamma\sqrt{Nt\tau}} \quad (2.9)$$

where γ = gyromagnetic ratio of the alkali atom

N = total number of atoms in the gas phase

τ = coherence time of atomic polarization

t = measuring time

At a constant temperature, N is proportional to the cell volume. For a given volume of alkali atoms and fixed measuring time, the sensitivity of the magnetometer is proportional to the coherence of atomic polarization. Consequently, the construction of a sensitive magnetometer depends on achieving the maximum possible polarization lifetime.

Since alkali atoms lose their polarization immediately after colliding with the cell wall, these collisions need to be suppressed. One possible way is to use a chemical that prevents depolarization to coat the surface. Paraffin is the most efficient coating, making the atomic spin coherence longer up to 10,000 times collisions of atomic spins with the surface without depolarizing [53]. With the paraffin coating technique, coherence times as long as ~1 s have been observed. A sensitivity of ~0.3 $fT/(Hz)^{1/2}$ was achieved in a rubidium cell of volume 500 cm^3 [34]. However, paraffin has a limitation in high temperature applications because of its low melting point. A coating of octadecyltrichlorosilane (OTS) on surface of high temperature has been reported [54]. Balabas *et al*. represented a coating with alkene material, 1-nanodecene, exhibiting Zeeman relaxation times up to 77 s, which is 2 orders of magnitude improvement (longer relaxation time) over the best paraffin (alkane) coatings. This coating was conducted at room temperature, which makes the magnetometer more practical [55, 56]. The other method is to fill the cell with a high pressure of an inert buffer gas to inhibit diffusion. Helium is often used in spin-exchange relaxation-free (SERF) condition, which eliminates high density spin-exchange collisions between alkali atoms [57]. The SERF magnetometer currently demonstrated the most sensitive atomic optical magnetometer at the sensitivity of 0.54 $fT/(Hz)^{1/2}$ for low-frequency magnetic fields, with potassium sensors of several

centimeters at 190 ˚C [45]. Furthermore, in magnetometers, the reduced atomic cell size enhances the filling factor. It reduces the distance between the sensor and the sample of interest. With Rb sensor, sensitivity 0.3 $fT/(Hz)^{1/2}$, but still using large measurement volume (500-cm^3 cell) [46, 58]. For near-dc magnetic fields, a sensitivity of 150 $fT/(Hz)^{1/2}$ was demonstrated with a centimeter-scale cesium magnetometer at 37 ˚C [59, 60].

Chapter 3

Cs atomic magnetometer instrumentation

3.1 Cs atomic magnetometer instrumentation

In this chapter, the details and characterization of a compact and sensitive Cs-based atomic magnetometer are described. A schematic of the setup is shown in Figure 3.1. The main components for the atomic magnetometer are: Cs atomic vapor cell, a multilayer shield, a diode laser, piercing solenoid, internal coils, optics, electronics for signal amplification and data acquisition. New features added to the instrument which caused the improved sensitivity of the atomic magnetometer will be discussed.

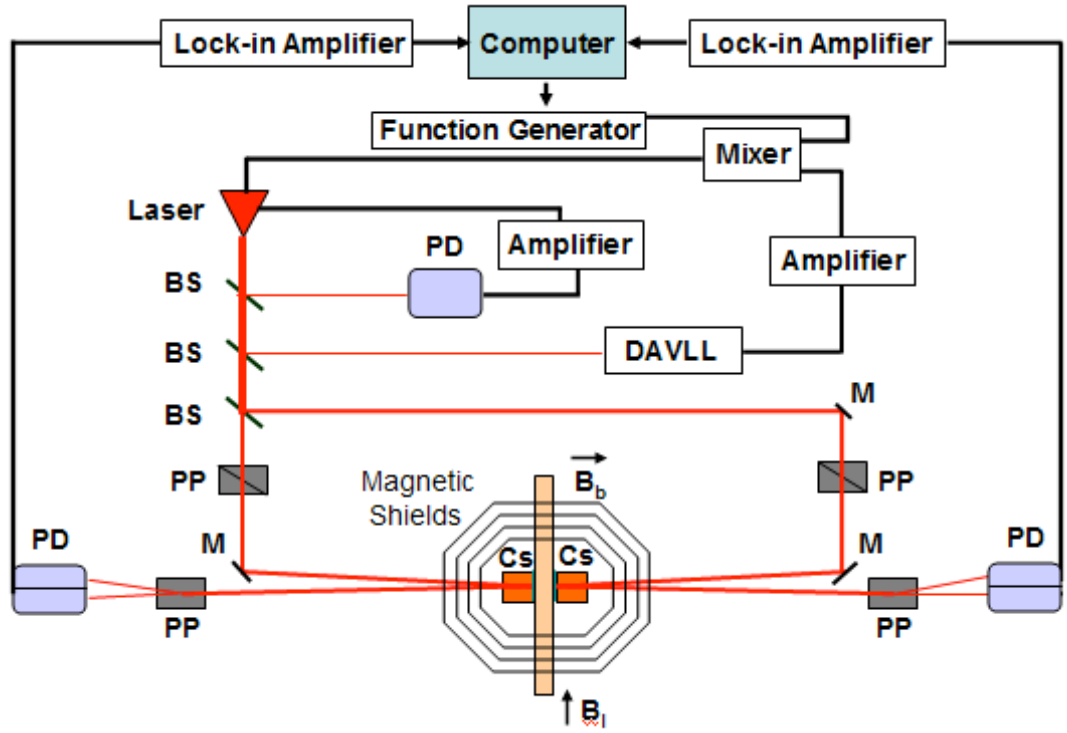

BS = Beam sampler
PP = Polarizing prism
PD = Photodiode
M = Mirror

Figure 3.1 Optical layout for Cs atomic magnetometer.

3.1.1 Paraffin-coated Cs vapor cells

One of the most critical elements of our experiment is the paraffin-coated Cs atomic vapor cells located at the center of the apparatus, Figure 3.2. The antirelaxation coating minimizes the coherence destructive collisions between the alkali atoms and the walls since atoms lose their polarization when they collide with the cell wall. The antirelaxation molecules enable atomic ground state polarization to survive many thousand wall collisions. The cell dimensions are 5 x 5 x 5 cm^3, mounted on a Delrin holder and housed in a magnetic shield to prevent environmental magnetic field noise. A gold mirror was glued on the back of the cell for beam reflection. A gold mirror was chosen because of its high reflectivity. The reduced cell size makes it possible for the sample of interest to be in closer proximity to the detector, thereby improving the filling factor.

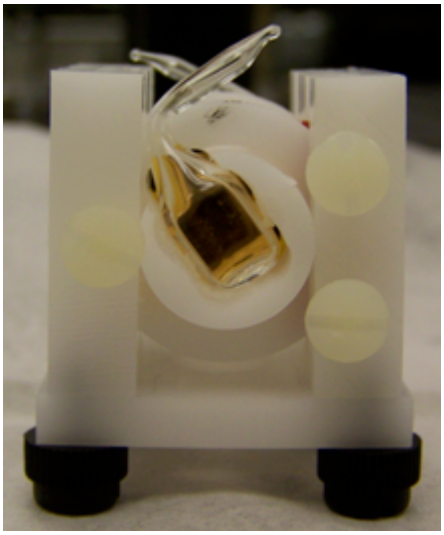

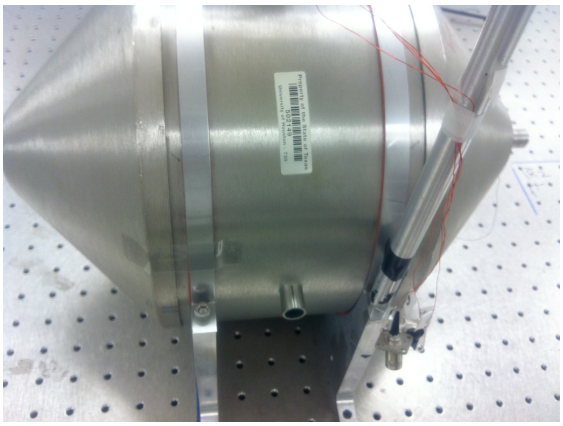

Figure 3.2 Cs cells and magnetic shield.

The appropriate temperature is needed to increase the number of cesium vapor atoms in the cell, at the same time, to maintain the alkali vapor density low enough to avoid the increased atomic collisions over the relaxation rate. The Cs magnetometer operated at body temperature, 37 ^{o}C, provides the maximum signal-to-noise ratio for this apparatus [59]. To avoid introducing extra noise from the heating source, stainless steel wires for heating were wrapped around outside of the innermost layer of the magnetic shield. This heating method was found to be efficient since noise was cancelled from the double winding configuration and shielded from the magnetic shield. A dc power supply was used as a heating source.

We use Cs cells over other alkali atoms in our magnetometers because the absorption bands of Cs are distinctly resolved, so the possibility of laser frequency cross-over is reduced. Also, Cs-based magnetometers seem to be the preferred type for common optical magnetometers due to their high accuracy and low heating demands.

3.1.2 Magnetic shields

To reduce magnetic field in the lab area, a multilayer magnetic shield is used. The shield has a cylinder center with caps on ends. The shield was made of mu-metal (0.15 cm thick and 22 cm outer diameter), manufactured according to the design by Xu *et al*. [61] by Amuneal Inc. The overall shape of each layer approximates a sphere to maximize the shielding factor. Between each layer, Styrofoam is used to hold the shield in place and also serves as a thermal insulation from the surroundings. There are four ports on the cylindrical parts and one each on the end caps for each layer.

These ports are used for optical access, sample inlet, piercing solenoid and electronic wire connections. The volume of our shield is compact, about 10% of the volume the shield used in [62] and is much smaller to that used by Ledbetter *et al*. [19].

3.1.3 Internal coils

The internal coils were wound around a Delrin tube inside the magnetic shield, including a Helmholtz coil, an excitation coil, and three gradient coils. These coils were used to cancel the residual magnetic field and gradients and to provide a bias field. The *z*-gradient coil is driven by an adjustable dc source (Krohn-Hite, Model 523). The bias field, which follows the Faraday optical rotation, is directed along the Cesium cell, defined as z-axis, and parallel to the laser beam. Since the sample magnetic field is much smaller than the bias field, the atomic magnetometer is only sensitive to the magnetic field change along the *z*-axis.

3.1.4 Diode laser and optical layout

A single diode laser, New Focus model 7018, tuned to the D1 transition of Cs (wavelength 894.95 nm), frequency modulated by driving a piezoelectric transducer in the laser cavity with a function generator, is used. The laser beam is first attenuated by a neutral-density filter. Two 5% beam samplers are used for controlling the laser. The first one feeds a photodiode for power monitoring. The voltage output photodiode is amplified and fed back to the laser for constant power operation. The second one is used for the Dichroic-Atomic-Vapor Laser Lock (DAVLL) system. Then, the rest of

the beam, which is the main laser beam, passes through a 50-50 beam splitter to supply beams for each magnetometer.

For each magnetometer, the incoming beam from the beam splitter passes through a Glan polarizer to set the initial polarization of the beam. Then, it hits the mirror to direct the beam into the Cs cell. The beam hits another mirror mounted close to the back of the Cs cell holder and is reflected back through the cell again and then through a Rochon polarizer located 45^{o} from the initial polarization prism. The refracted beams are detected by two photodiodes and amplified by a lock-in amplifier.

The double-pass arrangement was chosen for this setup (Figure 3.3). This is significant because of the small size of the cells used in this work, the double-pass arrangement increases the optical path length, i.e., the rotation is additive on the two passes, resulting in an increased the sensitivity of the instrument.

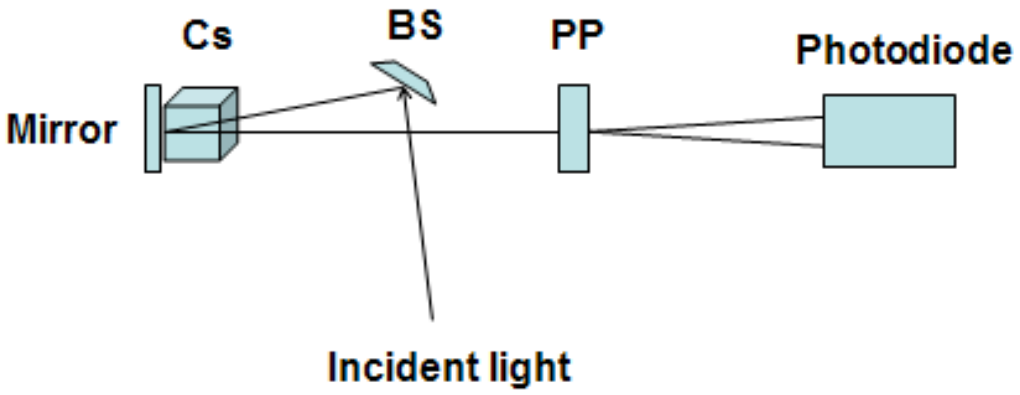

Figure 3.3 Double-pass arrangement.

3.1.5 Laser lock

Over time, the frequency of the laser will drift due to the instability factors, for example, temperature, current, mechanical fluctuations. These problems can be reduced by using a system called dichroic atomic vapor laser lock (DAVLL). It generates an electronic feedback signal to control the laser frequency and locks the laser for long term signal stability [63, 64]. A small portion of the laser is directed to DAVLL side to lock the laser at the frequency of resonance and to stabilize the frequency.

The DAVLL technique is used to extend the recovery range by using a magnetic field to split the Zeeman components of an atomic Doppler-broadened absorption signal and then generating an error signal that depends on the difference in absorption rates of the two components.

In the DAVLL setup, we measured the polarization rotation caused by the vapor cell by using a balance polarimeter consisting of the linear polarizer and polarization beam splitter (PBS) as an analyzer. The axis of the PBS is rotated by an angle $L = 45^{o}$ with respect to the axis of the polarizer. The normalized difference in the transmitted intensities of two PBS arms is the measure of the optical rotation. The spectral dependence of the magneto-optical rotation has a characteristic shape. The laser beam passes through a cell-magnet combination consisting of a glass cell filled with Cs vapor and a 200-G magnetic field. The magnet is made of rings of rubber-embedded permanently magnetic material, space appropriately and mounted together concentrically around the glass cell. The DAVLL signal is from subtracted photocurrents. The diode laser is then locked by feeding back a voltage to the

piezoelectric transducer (PZT) so that the DAVLL signal is maintained at the central zero crossing. The stability of the laser wavelength should be within the Doppler broadened atomic linewidth. Both the linewidth and power of the light were optimized because they are related to the noise in the polarization in the magnetometer. After a linearly polarized laser light passes Cs atomic vapor in the DAVLL box (Figure 3.4), it evolves to elliptical polarized light. Then, the beam passes through a quarter-wave plate and a polarization prism. Then, the final beams are fed into two photodiodes, which voltages are amplified by a lock-in amplifier (Stanford Research SR530).

The schematic of the DAVLL system and characteristics of the DAVLL signal are shown in Figure 3.5 and 3.6. The frequency lock point, which maintains at zero-crossing point, can be tuned by adjusting the angle of quarter wave plate. The differential signal from the two photodiodes is fed to the piezoelectric element of the laser, which maintains the frequency of the laser at the locking point.

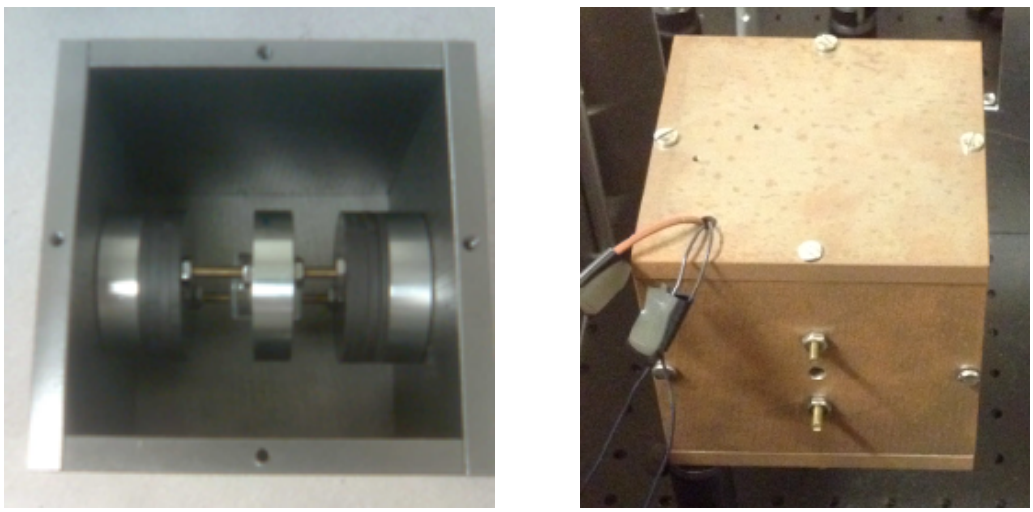

Figure 3.4 DAVLL box.

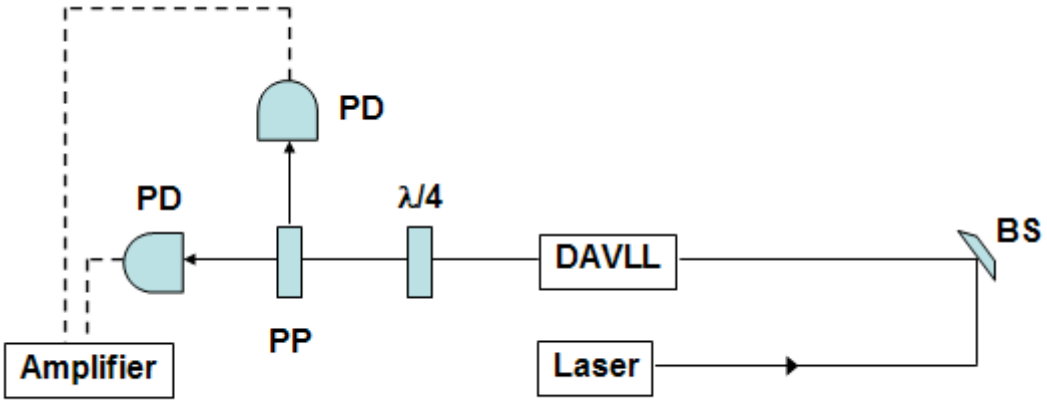

Figure 3.5 The schematic of a DAVLL system is illustrated. A small portion of the laser beam is directed to the locking apparatus where the Cs vapor cell is located inside. The light then passes through the quarter-wave plate followed by a polarizing prism which separates the right and left circular polarized beams. These are directed to the two photodetectors (PD) to analyze the intensity of the laser power of the polarized beams.

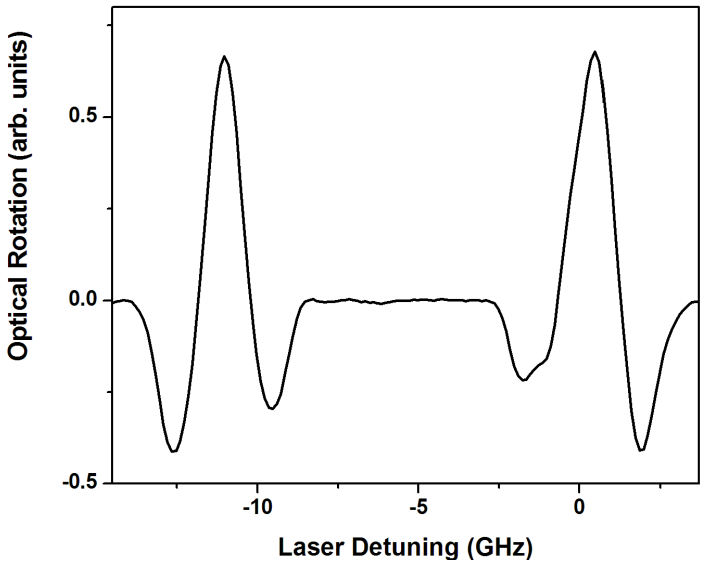

Figure 3.6 Magneto-optical rotation in DAVLL.

3.1.6 Signal detection, electronics and communications system

The photodiodes are connected in pairs without bias voltage so that the only the differential photocurrent is amplified, reducing the dark current. The differential photocurrent between the photodiode pair is detected by a lock-in amplifier.

Since fast modulation of light is necessary to overcome low-frequency noise. A lock-in amplifier (Stanford Research, SR830) is used. For NMOR, with frequency modulated light, detection of plane rotation must be synchronized. Therefore, a lock-in detector is an important element of the setup. In the experiment, the differential current signals were measured with a time constant of 30 ms.

The function generator provided the modulation frequency to the laser controller. Another model of lock-in amplifier used for the DAVLL system gave the dc signal to lock the laser at a specific wavelength. Using an ac-dc mixer, both information was fed into the laser controller. The function generator also communicated with both of the lock-in detectors to synchronize the detection of light.

A personal computer was used to display the in-phase and quadrature components of the NMOR signals as detected by the lock-in amplifiers, which were connected to the computer via a GPIB interface. Using a LABVIEW program (Figure 3.7), these signals could be visualized. The phases of both quadrature signals could be adjusted via the auto-phase button. The main goal was to set the phase of the in-phase signal to be less than 5^{o}, while the out-phase was less than 180^{o}. The oscillation amplitude of the modulation frequency and the modulation frequency can also be set via the LABVIEW program.

To lock the laser at the resonance frequency, the center frequency of the resonance signal was determined in the quadrature signal. This method was slow and required stabilization of the system each time the modulation frequency was changed. This can be overcome by a feedback algorithm that has proportional and integral parameters.

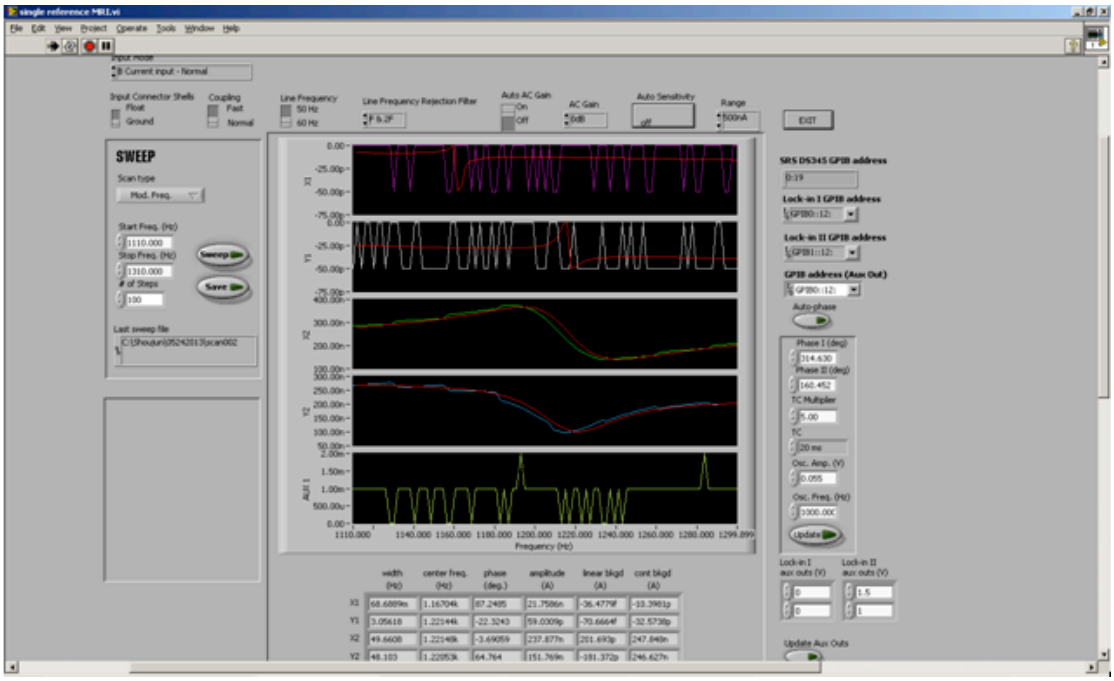

Figure 3.7 LABVIEW interface for GPIB communication and frequency modulation.

The deviations from resonance were proportional to the in-phase signal from one magnetometer. This signal was measured, inverted and fed back to the function generator and modifies the modulation frequency. The way the computer provided feedback is via an integral loop as given by the equation:

$$f = P(\varepsilon + I\int_{-t}^{0}\varepsilon dt') \qquad (3.1)$$

Where f is the feedback signal, ε is the error signal and P and I are the proportional and integral coefficient, respectively.

For calibration, we set P as 50% of the value of the oscillation threshold with a fixed integration range. The value of I was adjusted to optimize the respond of the instrument to discrepancies from the square waves.

The magnetometer designated as the primary channel was, therefore, always on resonance. On the other hand, the in-phase signal from the other magnetometer was free of common-mode noise. This algorithm is especially advantageous since it is not sensitive to noise and it enables the user to alter parameters of the integral function.

3.2 Characterization of the instrument

3.2.1 Absorption of Cs

The laser with the wavelength tuned to the D1 transition of the Cs atoms is used to optically pump the atoms in the cells. The experimentally obtained absorption profile of Cs atom from one of the sensors is shown in Figure 3.8. We chose the D1 line over D2 because the hyperfine transition strengths in D1 are much stronger compared to those in D2 [65]. From experiments, we observed that for a particular voltage range, the one that was tuned to the highest voltage gives the most sensitive and stable signal. This voltage corresponded to the highest wavelength, which corresponded to the lowest energy requirement of the hyperfine transition $F= 4 \rightarrow F' =3$.

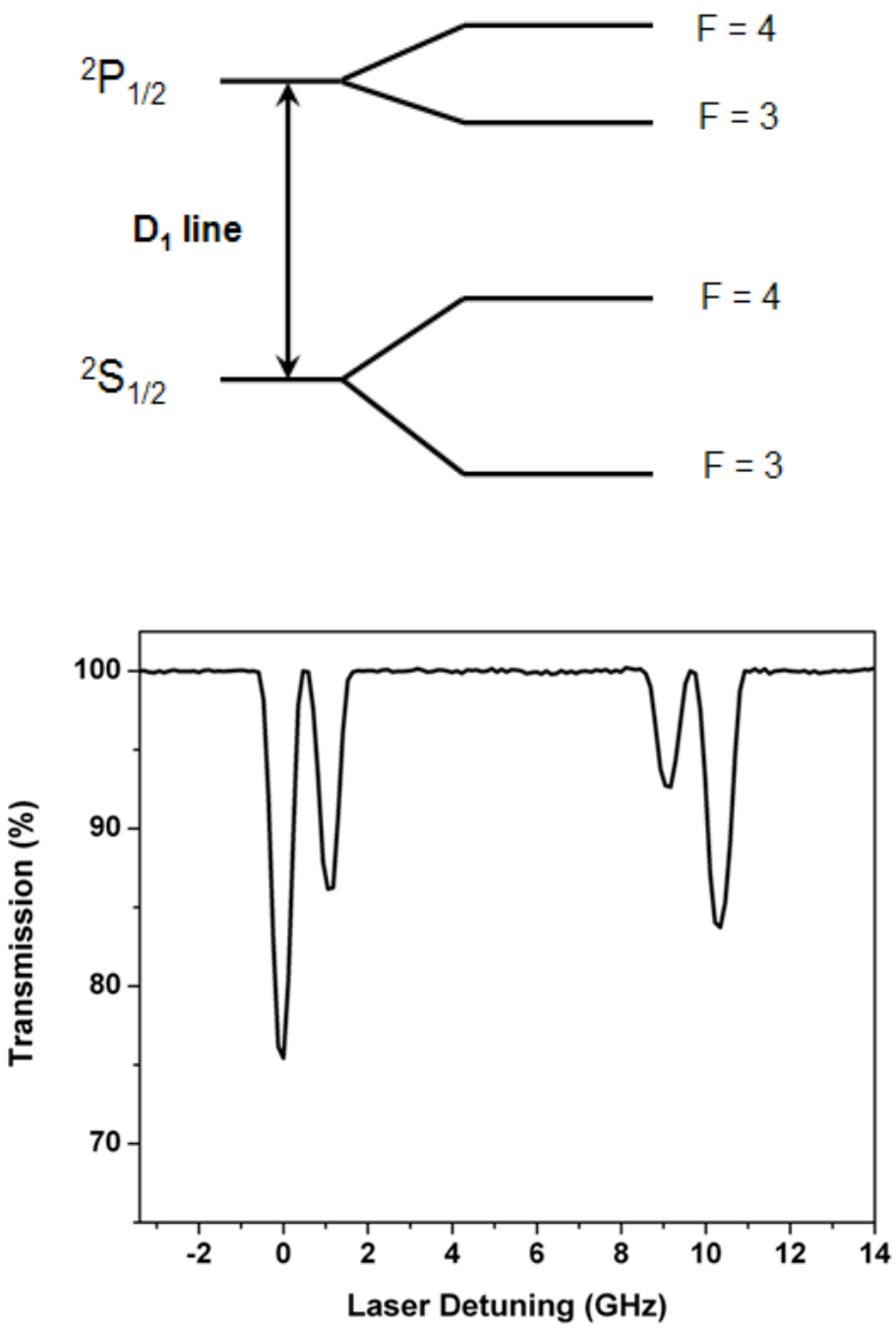

Figure 3.8 Absorption of Cs sensor of the D1 transition.

3.2.2 Nonlinear magneto optical resonance

With the laser detuning fixed at the optimal position, we sweep the modulation frequency of the laser to get the resonance due to the non-linear magneto optical resonance (NMOR). This occurs when the modulation frequency is twice of the Lamor precession frequency. A bias field was used to detect the resonances. The in-phase and out-phase quadrature signals are shown in Figure 3.9. The magneto-optical rotation is measured by a pair of photodiodes and amplified by a lock-in amplifier (SR 830).

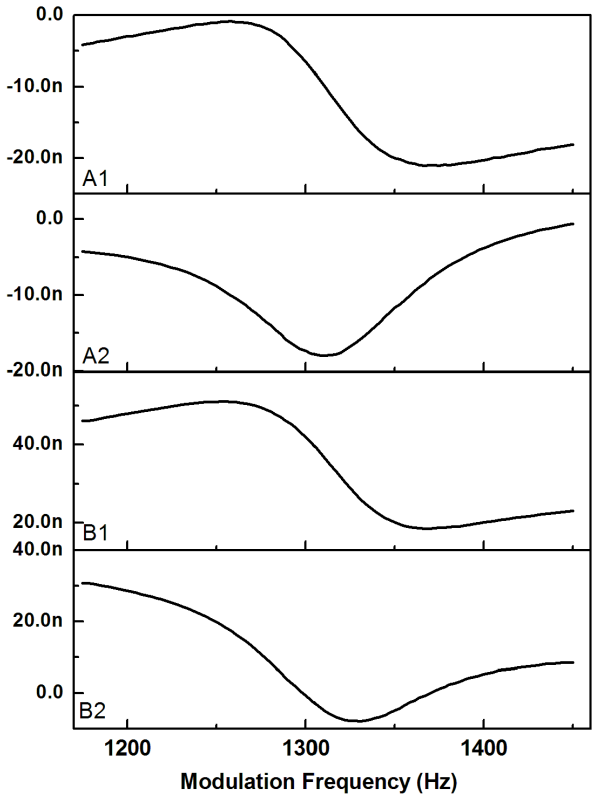

Figure 3.9 The resonance signals, in-phase and out-of-phase, of two Cs magnetometers.

3.2.3 Instrumental calibration

In order to determine the sensitivity of the instrument and to calibrate the optical output from the lock-in amplifier, an ac magnetic field, 0.1 Hz (~ 100 pT), generated by a function generator was used. The integration time is 30 ms per data point. The sensitivity of our magnetometer is 150 fT/(Hz)$^{1/2}$ with optimal operating temperature at 37 ^{o}C as described in [59].

The difference signal between the two sensors is plotted in Figure 3.10. Calibration was done by simply comparing the ratios between the magnetic field and amplitude of the test signal versus the magnetic field and amplitude of the sample being measured.

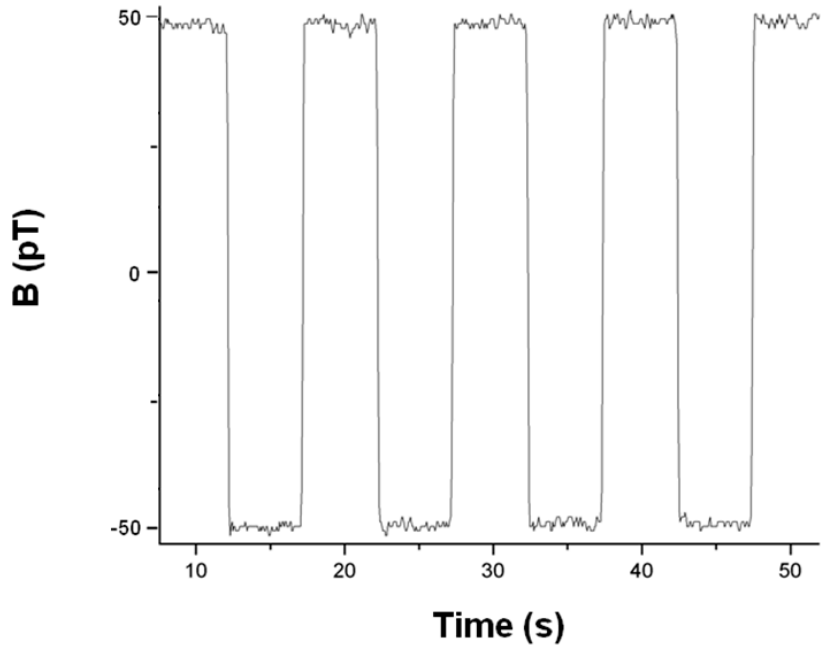

Figure 3.10 Square wave signals ranging from -0.1 V to 0.1 V for signal calibration.

3.3 A new design of atomic magnetometer

The Cs atomic magnetometer with new features was built in order to make our instrument more applicable to study systems of interest and to enhance the sensitivity of the instrument. New features included new sets of magnetic shields with different caps, a plastic disk that served as a divider and the gradient piercing solenoid.

3.3.1 Divider

A key feature in this design is a dividing piece that separates the piercing solenoid and the atomic sensor. The divider is made of a thin plastic and placed in the middle of the four-layer magnetic shield (Figure 3.11a). The divider prevents air circulation caused by the motion of the transducer and maintains the atomic sensors at a stable temperature. Therefore, it reduces the undesired optical rotation caused by air currents and avoids the atomic density fluctuation caused by the temperature instability that would occur otherwise.

3.3.2 Cs cell

The atomic sensor used in this study is shown in Figure 3.11b. It is essentially a cubic-shaped glass compartment with a long tail. The cubic portion is 5 mm long on each side and coated with paraffin to elongate the coherence time of the polarized cesium atoms. The tail contains a drop of cesium and is connected to the cubic cell by a narrow channel so that cesium atoms continuously refill the cubic compartment.

a) 

b) 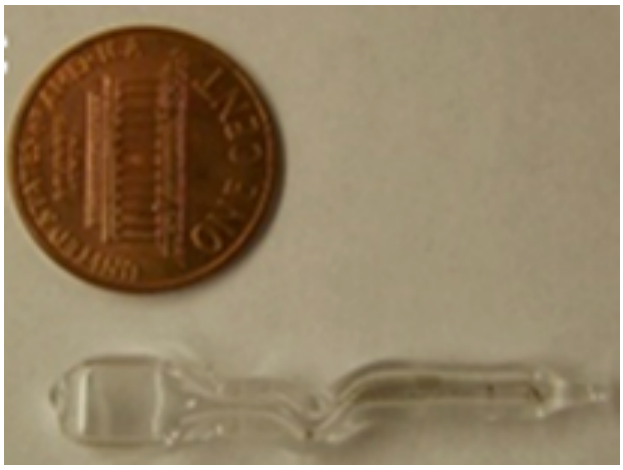

Figure 3.11 a) The photo of 4-layer magnetic shields. A plastic divider separates two regions of the shield. b) The Cs vapor cell is mounted on a platform located at the center of the magnetic shield.

a)

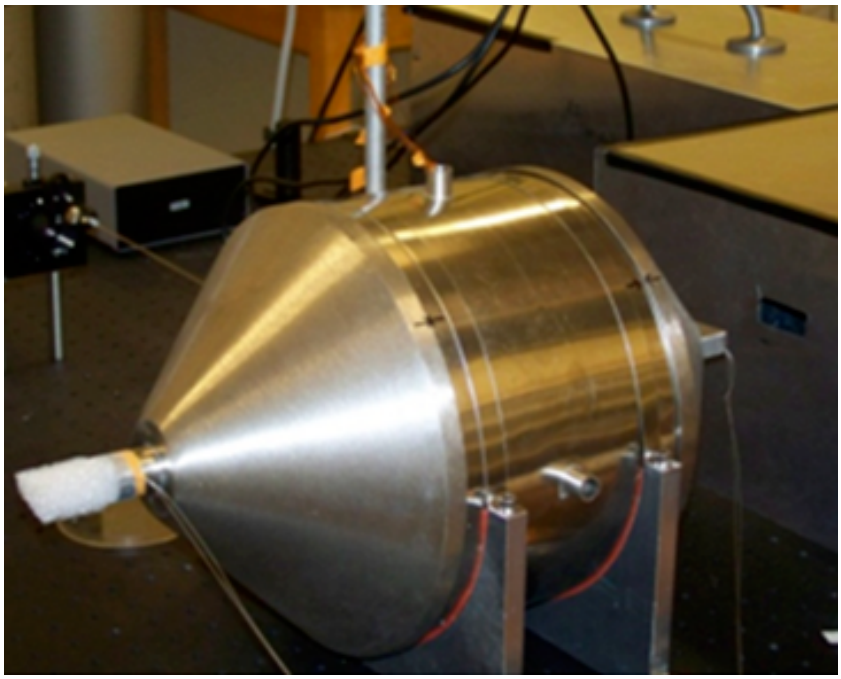

b)

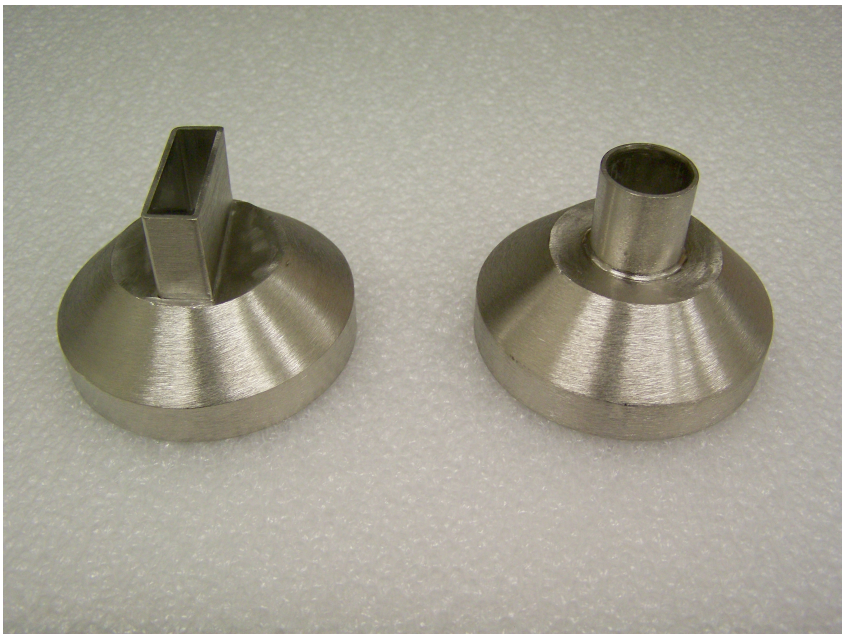

Figure 3.12 a) A new built atomic magnetometer with new features. b) Internal magnetic caps with different port shapes.

3.3.3 Magnetic shields and internal coils

The caps on one side of the new set of magnetic shield have rectangular ends. The innermost caps of the magnetic shield are shown in Figure 3.12. Unlike the previous built magnetometer, the sensor(s) can be arranged on one side, while the flowing of the sample can occur either through the central port of the magnetic shields, or the other side of the magnetic caps. This new configuration minimizes noise due to air turbulence and also improves instrument stability.

A set of coils is mounted on a hollow cylindrical Teflon holder inside the magnetic shield. Figure 3.13 shows the technical design for the coils. There are five different set of coils inside the shield: Helmholtz coil, Maxwell coil, Golay coil, and two saddle coils. Gradient field is provided via the Maxwell coil. The Golay coil was placed inside the magnetic shield for field calibration. The rest of the coils are for noise cancellation.

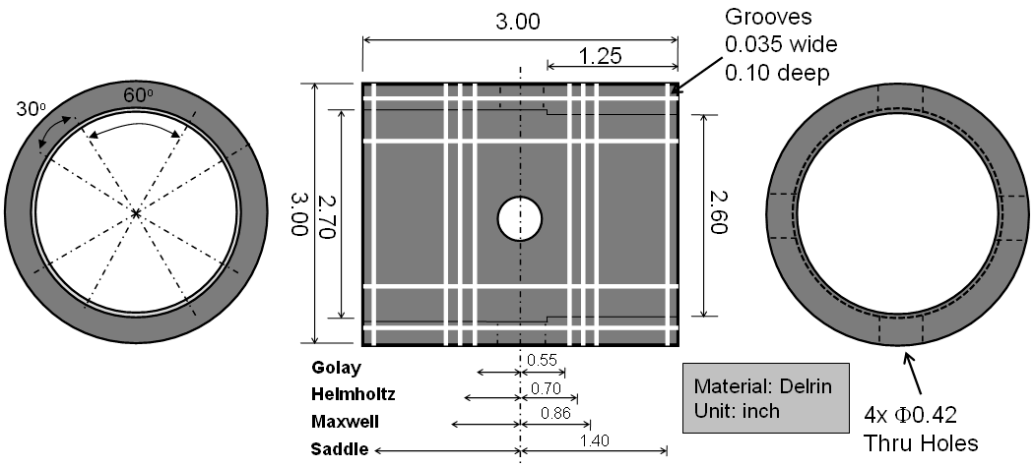

Figure 3.13 Schematic of the design for a coil holder located inside the magnetic shield.

A coil was placed inside the magnetic shield for field calibration (not shown). The sensitivity measurement was conducted in two steps. First, 0.5 and -0.5 V were applied to the coil to observe the difference in the resonance frequency ω_m. Second, at a constant ω_m, ±0.1 V was applied to the coil to obtain the signal-to-noise ratio and, subsequently, the sensitivity.

3.3.4 Characterization of the instrument

The magneto-optical profiles are shown in Figure 3.14 for 0.5 and -0.5 V, respectively. Fitting with dispersive Lorentz function gives resonance frequencies of 1,242.77 and 1,239.50 Hz. Therefore, 1 V corresponds to a magnetic field of 467 pT for the specific calibration coil used in this apparatus. Next, the magnetic fields produced by -0.1 and 0.1 V were measured (Figure. 3.15). The jump in the signal represented the change in voltage from -0.1 to 0.1 V, which was 94 pT based on the calibration in Figure 3.15 The detection bandwidth is 50 Hz. From the signal-to-noise ratio of ~170, we deduced the sensitivity to be ~80 fT/$(Hz)^{1/2}$. This is an improvement compared with the ~150 fT/$(Hz)^{1/2}$ sensitivity of a previous atomic magnetometer using the same atomic sensor [59].

The improvement in sensitivity is likely due to the implementation of the divider that increased thermal stability. Our previous study demonstrated that temperature played an important role in the sensitivity of atomic magnetometers [59]. Compared with the microfabricated atomic sensors that use rubidium atoms, our current apparatus has slightly worse sensitivity. For example, a recent report demonstrated a sensitivity of 50 fT/$(Hz)^{1/2}$ using a microfabricated Rb sensor [66],

which is better than that of our current apparatus. However, our apparatus uses Cs atoms in the sensor instead of Rb. One significant advantage is that the operating temperature is much lower, 35-37 ^{o}C as opposed to 180 ^{o}C, because cesium has the highest vapor pressure of all the alkali elements and our magnetometer is operated at low vapor pressure condition. The much lower operating temperature facilitates the applications of atomic magnetometers to avoid undesired heating of the samples.

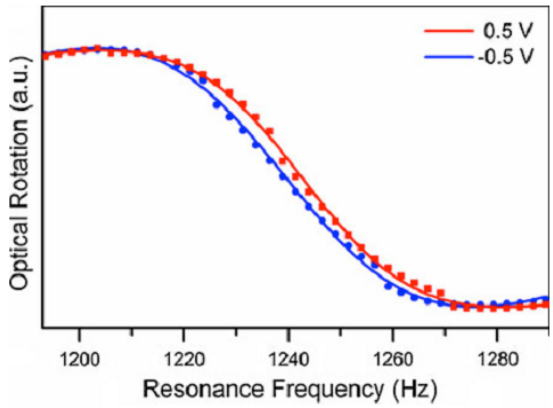

Figure 3.14 Magneto-optical resonance profiles for calibrating magnetic fields.

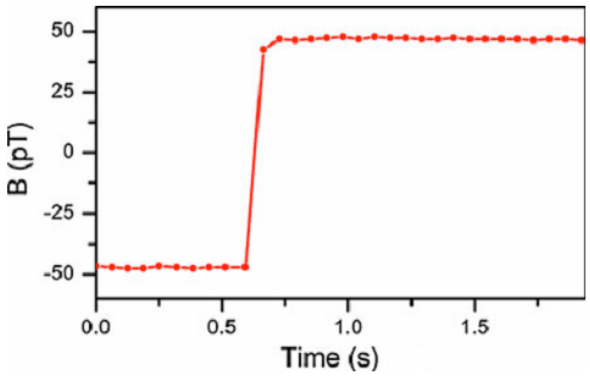

Figure 3.15 The sensitivity of the atomic magnetometer.

3.4 Detection schemes for NMR and MRI

Two primary schemes have been explored in detecting MR signal with an atomic magnetometer namely, the remote detection scheme and the radiofrequency detection scheme. Both schemes are applicable for low-field NMR and MRI. We have reported the applications of atomic magnetometer in NMR and MRI in chapter 1. Here, we use the remote detection of MRI, which is the technique that overcomes the problem of low sensitivity.

3.4.1 Remote detection

Remote detection is a special technique in which the signal detection location is spatially separated from the sample location where the spectroscopic (for NMR) or spatial (for MRI) information is encoded, so that the sample can attain both high encoding quality and high detection sensitivity. Remote detection of NMR and MRI was first developed by Pines and co-workers [67]. A schematic is shown in Figure 3.16. In this detection scheme, the information is stored as time-dependent total magnetization M_z of a mobile NMR-active sensor medium along the longitudinal axis, which can be transferred from the sample to the detector.

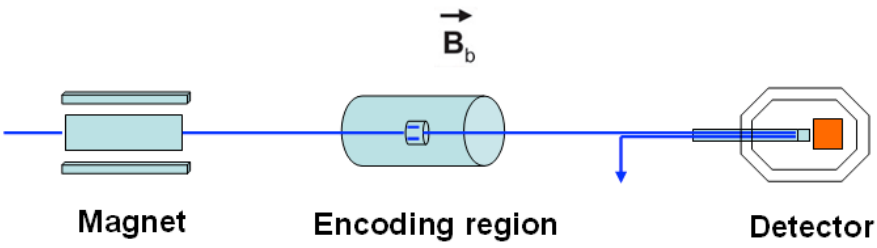

Figure 3.16 Remote detection of MRI with an atomic magnetometer.

The information can be transported by any fluid that has NMR active nuclei with a sufficiently long spin-lattice relaxation time, T_1, and then read out of the encoded information after the time of travel at the detector. Many nuclei are suitable for using as NMR signal carriers, for examples, ^{3}He, ^{129}Xe, ^{13}C or ^{1}H. The carrier can be in the gas or in the liquid phase. T_1 of the carriers are different from hours to a few seconds. The encoded information can be recovered by Fourier transformation of the sample magnetization. The "filling factor", the extent to which the sample couples to the detector, is used to indicate the detection efficiency. If the sample is spread out spatially, this precludes efficient NMR detection. Remote detection enhances the filling factor as the sample can be concentrated in the detection region and consequently the detection efficiency is improved [68-72].

In NMR experiments, conditions for optimized encoding are to use a good rf coil and magnetic field homogeneity. In contrast, improving signal detection includes using high magnetic fields and small rf coils. As remote detection technique spatially separates the detection from the encoding region, optimized detection can be achieved not only by rf coils of optimized size since the coil detection sensitivity is inversely proportional to the coil diameter. Alternative methods have been used, for instance, SQUIDs or atomic magnetometers.

3.4.2 Radio frequency (RF) detection scheme

RF detection scheme was demonstrated for detection of proton NMR signals with a radio-frequency atomic magnetometer, presented by Savukov *et al*. [73] as shown in Figure 3.17. In this scheme, the sample is static, similar to conventional

NMR. A pulsed magnetic field is used for prepolarization. (For fluidic samples, the sample may also be polarized by a permanent magnet outside the magnetometer and flow into the detection region.) The nuclei are located inside a closely wrapped long solenoid, so that this field is not experienced by the outside atomic magnetometer. By tuning the bias field B_b, the precession of the atoms matches the precession of the nuclei, allowing direct detection of the nuclear precession (free induction decay). An NMR spectrum has been exhibited with this technique.

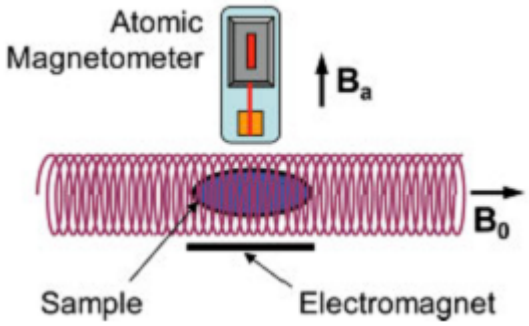

Figure 3.17 RF detection scheme with atomic magnetometer. A long solenoid provides a leading field B_0 for the sample nuclei, whereas the alkali atoms do not experience this field. A tunable ac field B_b is applied to the atomic magnetometer so that the atomic precession matched the nuclear precession in order to observe resonance.

3.5 Remote detection setup

The remote detection technique was used to detect the magnetization of our sample. In this detection scheme, the sample nuclear spins go through three separate

stages as follow: pre-polarization, encoding and detection. In the pre-polarization region, the molecules of sensor medium, in this case, water, are magnetized by flowing through a 2 T permanent magnet. A brass rod sample holder containing a 5 μm porous material is placed inside the bore of the magnet to keep the fluid inside the magnetizing region as long as possible while retaining the same flow rate, then flow through a tube to the encoding region, which provides low and homogeneous magnetic field, then to the detection region. A fast flow rate, 28 ml/min, is set to minimize the relaxation of the nuclear polarization during the travel from the pre-polarization region to the detection region.

3.5.1 Encoding region

In the encoding region, Tecmag LF1 Apollo (rf transmitter system) produces and sends the excitation signal (rf pulses) to the encoding coil to excite nuclear spins of the sample via a power gain device, HP 461A amplifier. The gradient pulses from Tecmag for conducting one- and two-dimensional image experiments were amplified by AE Techron LVC 623 amplifier and transmitted to the gradient coils wound on the encoding cylinder.

An excitation field is required for excitation of the transverse magnetization in the sample. In addition, highly linear magnetic field gradients, that can be turned on and off during a relatively short time (normally in the millisecond timescale), are essential for spatial localization in MR imaging. Because of different functions and required characteristics of the excitation field, and gradient field, they are produced by different devices known as excitation coils and gradient coils, respectively.

3.5.1.1 RF excitation coils

A saddle coil, or rf excitation coil, drives the rf signal. The saddle coil is compact and easily constructed and can generate a uniform magnetic field perpendicular to the axis of the cylinder. The coil must produce uniform field and can be obtained by configuring the dimensions of the coils. The amplitude and homogeneity are obtained by the configuration of the angle, the length and diameter. An rf coil uses a number of wires wound on a cylindrical surface. It consists of four 120^{o} circular arcs and four linear segments, at 60^{o} and 120^{o} carrying equal currents in one direction and two other segments at 240^{o} and 300^{o} carrying equal currents in the opposite direction as shown in Figure 3.18. The optimal homogeneous coil can be obtained when ratio of length between loops and diameter *(l*/*d*) is 1.41 [74]. For the saddle coil used in our experiment, the length and the diameter are 2.0 and 1.42 inches, respectively.

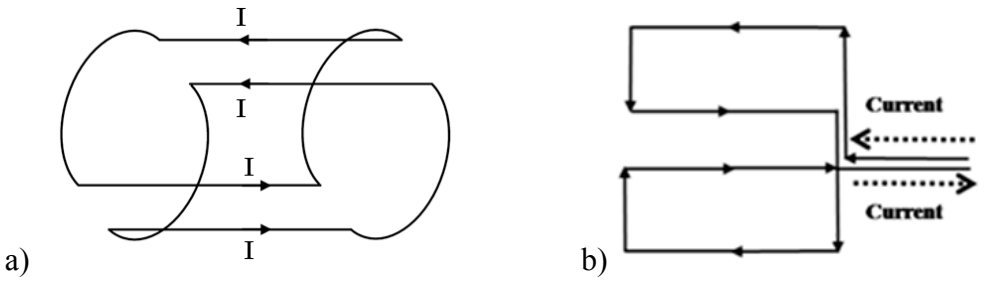

Figure 3.18 a) An excitation coil. b) Direction of current flow.

3.5.1.2 Gradient coils

Spatial localization in MRI is accomplished by using three orthogonal magnetic field gradients. A magnetic field gradient along *z*-axis (longitudinal gradient) is commonly generated by two identical coils carrying the same magnitude of currents, *I*, in opposite directions, known as a Maxwell pair (Figure 3.19). These coils are wound on the same coaxial cylinder used for the coils producing the excitation magnetic field. A commonly used coil configuration for *x*- and *y*-axes (transverse gradients) is Golay coils, which have double-saddle configuration of eight 120^{o} circular arcs (Figure 3.20). The arcs are connected by eight straight segments parallel to the *z*-axis. These *x*- and *y*- gradients are two identical coil arrangements that are rotated by 90 degrees around the *z*-axis relative to each other.

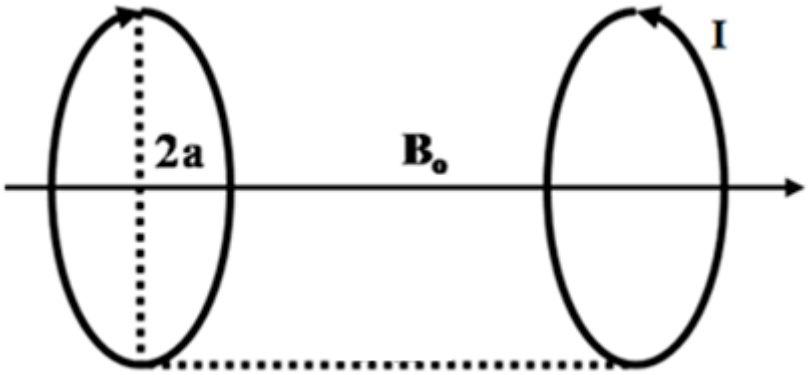

Figure 3.19 Maxwell coils to produce a linear field gradients in B_0 along the *z*-axis.

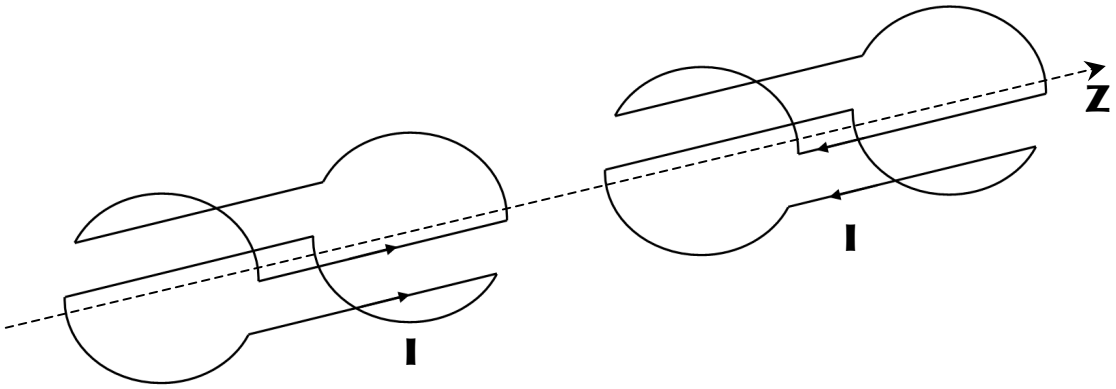

Figure 3.20 Golay coils to produce a linear gradient field in B_0 along the *x*- and *y*-axes.

For the Maxwell pair coil, *z* axis, distance between loops is chosen to be √(3/2), where *a* is radius of the coil loop. This gradient is uniform up to 5% within a sphere of radius 0.5*a* [75]. For Golay coils, *x* and *y* axes, these gradients are uniform up to 5% within a sphere of radius 0.6*a*. The picture of encoding cylinder is shown in Figure 3.21.

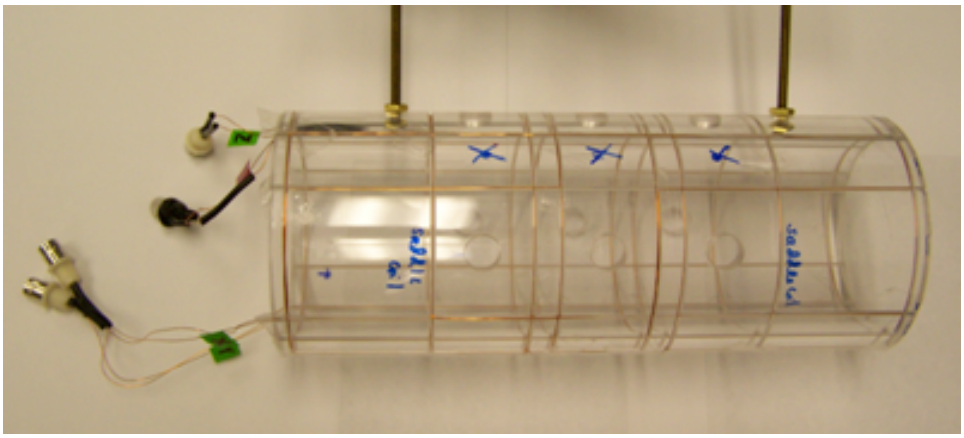

Figure 3.21 Gradient coils wound around an acrylic tube. Length and dimensions are measured based on the efficiency parameters.

The spatial encoding in MRI is achieved by using linear gradient magnetic fields. A new holder for gradient coils was made to increase gradient linearity over a large volume and also increase the coil efficiency (field gradient per unit volume). This coil provides a gradient uniform within a sphere of *a*/2, where *a* is the radius of the coil loop. Gradient uniformity quickly deteriorates beyond this region.

All three gradient coils are wound on a cylindrical coil holder, with a radius of 47 mm (Figure 3.21). The gradient efficiency (field gradient per unit current) for the Golay coils, for the *x*-and *y*-axes, is given in Equation (3.2). The gradient efficiency for the Maxwell coil for the *z*-axis is determined by Equation (3.3):

$$\eta = \frac{9.18 \times 10^{-7}}{a^2} \text{ T m}^{-1}A^{-1} \tag{3.2}$$

$$\eta = \frac{8.058 \times 10^{-7}}{a^2} \text{ T m}^{-1}A^{-1} \tag{3.3}$$

Using this set of gradient coils, the flow of water in a porous sample is imaged with Earth-field MRI. The porous metallic sample is of cylindrical shape, with 6.5 mm diameter and 10 mm length. The field-of-view is set as 22 mm along the *z*-axis and 12 mm along the *y*-axis. The gradient amplitudes can be calculated using the following equation:

$$FOV = \left(\frac{\gamma}{2\pi} G_{PE} \tau\right)^{-1} \tag{3.4}$$

Here γ is the proton gyromagnetic ratio, G_{PE} is gradient stepsize, and τ is the duration of the gradient field. τ is set as 5 ms for convenience in the current study. The gradients applied were 2.1 and 3.8 mG/mm, for the *z*- and *y*-axes, respectively. Based on the Equations (3.2) and (3.3), currents of 0.58 and 0.92 A were used for the *z*- and

y-axes, respectively. As the results, the power used for spatial encoding in low field MRI using atomic magnetometer is extremely small compared to conventional MRI.

3.5.1.3 Pulse sequences

The spectroscopic or spatial information can be encoded with the aid of appropriate pulse sequences (and weak gradients in the case of MRI). Information regarding the flow profile of sensor medium can be obtained by tracing the flow of the tagged spins from the encoding region to the detection region. The pulse is generated and amplified by Tecmag LF1 Apollo and RF amplifier, as shown in Figure 3.22. To obtain flow profile of the fluid, at the encoding region, a π pulse was used to invert the magnetization, as shown in Figure 3.23a. The magnitude of the magnetization is measured when it reaches the detection region.

a) 

b) 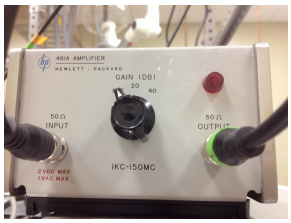

Figure 3.22 a) Tecmag LF1 Apollo unit for sending rf pulses and phase encoding. b) RF amplifier model HP 461A.

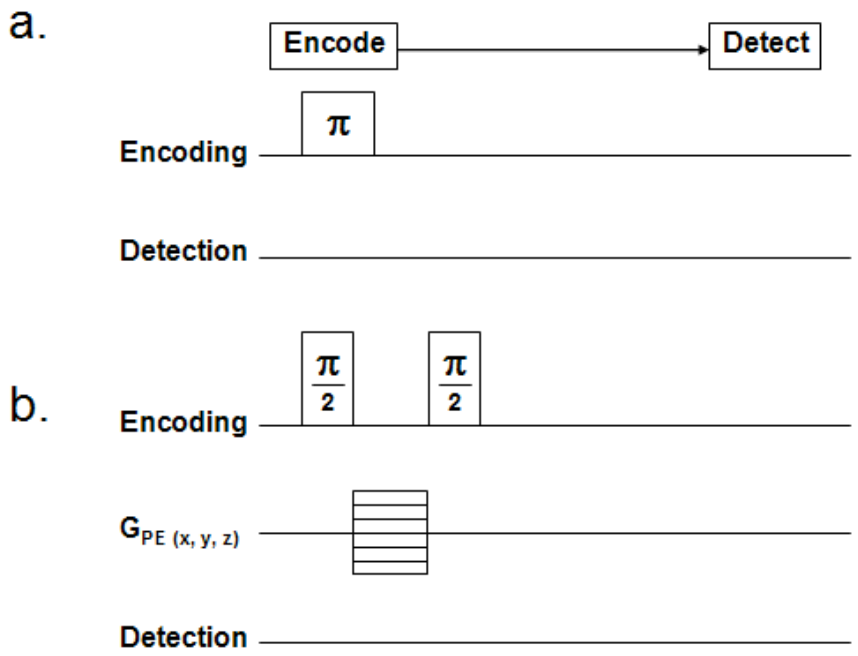

Figure 3.23 Pulse sequences. a) π pulse is used to invert the spins of the sensor medium to obtain the flow profile. b) Phase encoding pulse sequence for 1D and 2D imaging.

For remote detection of MRI, a pure phase encoding pulse sequences is most often used, as shown in Figure 3.23b. A π/2 pulse was applied, which tips the magnetization of the spins in the perpendicular plane. The spins precess in the presence of the gradient magnetic fields, which now contain spectral or spatial information. Then, a second π/2 pulse serves as the storage pulse. It stores the magnetization along the longitudinal axis, which is remotely detected by the magnetometer. The image is constructed by performing Fourier transform to take the data from the time domain, and then, relate it to the spatial domain. From using the phase-encoding pulse sequence, one-dimensional and two-dimensional images were obtained.

3.5.2. Detection region

3.5.2.1 Piercing solenoid, bias magnetic field and sample polarization

A long hollow solenoid, as shown in Figure 3.24, that pierces the magnetic shield provides a leading field (approximately at Earth's field, ~0.5 G) which is required for the nuclear spins in the sample. This leading field directed the spins in the sample after the encoding region to the sample holder in the detection region.

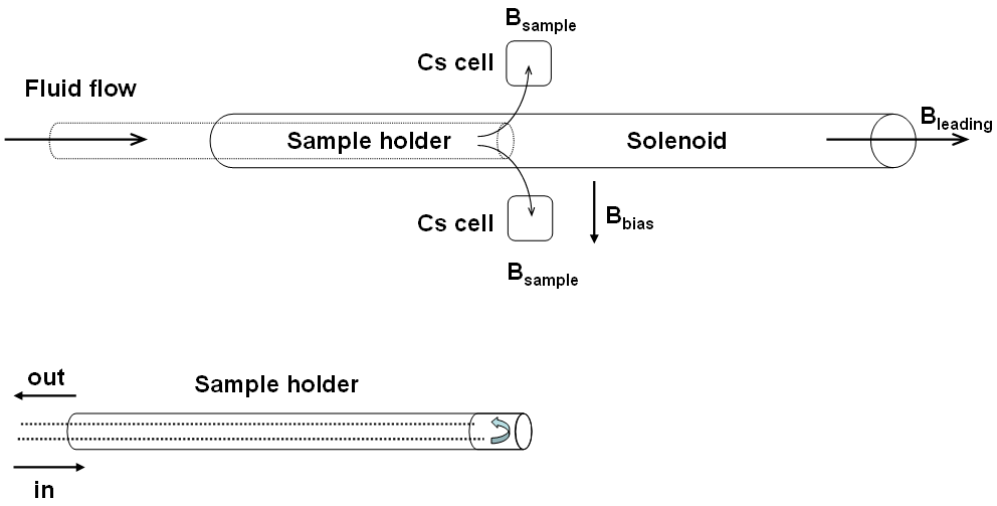

Figure 3.24 Detection region of the remote detection scheme. The piercing solenoid (top) generates the leading field ($B_{leading}$). Detection axis is defined by a bias field (B_{bias}). The two Cs cells experience the magnetic field introduced by the sample (B_{sample}). The copper sample holder (bottom) has two tubes inserted, for the detection of nuclear magnetization.

The fluid sample travels from the encoding region to the detection region via a copper tube with a cap that can hold 140 μL of sample. The magnetization of spin is directed into the region via a leading field of approximately at Earth's field, ~0.5 G, produced by the piercing solenoid. The direction of detection was set by applying a bias field (Figure 3.24). This enables both of the sensors to detect the magnetization of the flowing sample.

To achieve high resolution in MRI, the sample holder is placed in an optimal position to detect high magnetization signal regarding to the fact that the magnetic field strength exerted by the sample B_s on the detectors is inversely proportional to the distance r^3. With the orientation of the sensors, the magnetization signal from both sensors can be added and the common mode noise can be cancelled [49]. In other words, the sensors directly measure the magnetization of the sample.

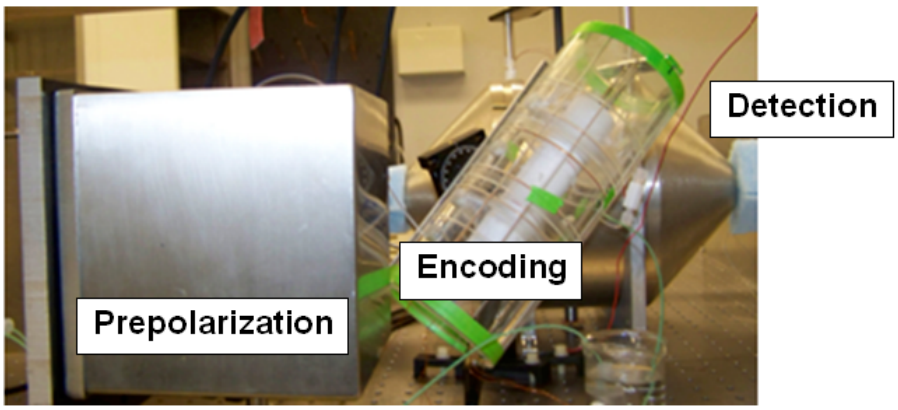

Figure 3.25 Remote detection setup. The fluid sample driven by a micropump (not shown) flows continuously through three consecutive regions: Prepolarization magnet, encoding region, and detection region. The sample is recycled to the reservoir.

A continuous stream of water driven by a microannular gear pump from a reservoir of the sample flows continuously through three consecutive regions: Prepolarization magnet, encoding region, and detection region. With this set-up, a minimum amount of sample can be used and recycled. Figure 3.25 shows the remote detection setup. TECMAG is used to give the pulse sequence in Figure 3.26. The resonance frequency is 2045 Hz. The duration for the π/2 pulses is 6 ms. The duration for the gradient is 10 ms. The average water signal, 1D- and 2D-images were obtained using MATLAB (see Appendices A1-A3 for MATLAB scripts).

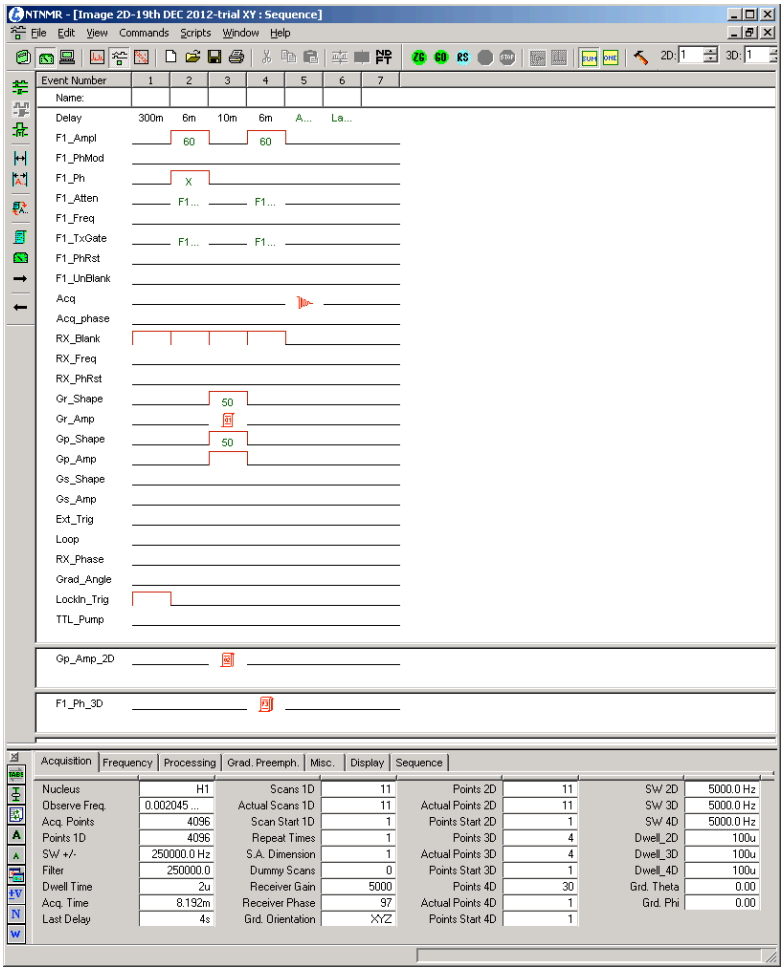

Figure 3.26 Pulse sequences for MR imaging of remote detection experiment.

Chapter 4

Applications of optically detected MRI for penetration in metal

4.1 Motivation of the study

Optically detected MRI uses sensitive atomic magnetometers to detect nuclear spin magnetization at a low magnetic field (typically less than ~1 mT). To fully benefit from the advantages of this technique, quantitative applications are needed, which are lacking at present. Specifically, low-field MRI has an advantage compared to high-field MRI: the capability of penetrating through metal [76]. Our goal is to quantitatively explore this aspect.

Porous materials with metallic character or impurities are implemented in a wide range of applications, including filtration, well logging, catalyzed reactions, and medical implants [77-81]. In these applications, the fluids inside the porous materials are often important, for example, oil flow in porous rocks and the products formed

inside catalyst pores. Therefore, visualization of the flow dynamics will allow a better understanding of the fundamental process inside the pores. Consequently, such results will aid in the analysis, evaluation and improvement of these materials for the related applications. Various techniques have been used to characterize these materials. Techniques such as X-ray tomography and digital image correlation have been used to characterize the structure and mechanical properties [82]. TEM can reveal pore shape, topology and mean size, but pore overlap can make interpretation difficult, and this method provides a detailed image at a limited region on the surface of the material. Optical techniques are not applicable because these materials are opaque.

NMR and MRI are valued tools that have been used to noninvasively observe processes in porous media and also suitable techniques to study opaque samples [83-85]. Many high-field MRI studies on porous materials have been reported [86-89]. But no high-field MRI studies have reported on porous metals because radiofrequency radiation has poor penetration depth in metal and the severe distortion of the magnetic field caused by the metal.

To circumvent the penetration problem, low-field MRI is capable of imaging fluids in porous metallic materials. In particular, the Earth's magnetic field (~50 μT) is appealing for low-field MRI because it is readily available and its homogeneity can be used for the study of large samples. Since the encoding is performed in a low magnetic field, the field distortion by the materials is not significant. The corresponding Larmor frequency of nuclear spins will be much lower, in the audio-frequency range, which has a much larger penetration depth in metallic materials. For instance, the skin depth of 2.1-kHz electromagnetic wave, which corresponds to the Larmor frequency of protons at 50 μT, is on the order of 1 cm in typical metals,

whereas the skin depth is only a few micrometers for 500-MHz radiation [90]. The nuclear spins buried deeper than the penetration depth will not be sufficiently excited and will not contribute to the MR images. In addition, magnetically heterogeneous samples can be studied in an ultralow magnetic field because the field distortion induced by the magnetic susceptibility of the sample is proportional to the magnetic field strength.

The consequence of using a low magnetic field for MRI is that a sensitive detection technique must be implemented. The conventional detection, which is based on Faraday induction, has a poor sensitivity in a low-field because the sensitivity is proportional to the magnetic field strength. Among low-field magnetic sensors, superconducting quantum interference devices (SQUIDs) and atomic magnetometers offer sensitivity on the order of femtotesla. SQUID-detected MRI shows promise in imaging samples in a metallic container and nearby metals [90]. However, SQUIDs require cryogenics to generate strong magnetic field, most often liquid helium, to maintain the superconductive state of the detector and also leads to high cost and limits the mobility of the instrument to remote areas. Conversely, optical detection with atomic magnetometers operates at near ambient temperatures and, unlike SQUIDs, does not require cryogenics. Optically detected MRI has produced MR images of fluids in a porous metal as a proof-of-principle experiment [76].

In this chapter, we report our study on quantitative measurements using optically detected MRI. We demonstrate that optically detected MRI is an effective technique for quantitative details of the flow inside a series of porous steels with different pore sizes. With the appropriate set-up, it will be shown that optically-

detected MRI, coupled with the remote detection scheme, is a tool that can be used to overcome limitations of high-field NMR/MRI applications.

4.1.1 Remote detection scheme

To study flow with MRI, the remote detection (as previously described in section 3.4.1) was again introduced by Seeley *et al*. [91] and further developed by Granwehr and coworkers [92]. A generalized schematic is shown in Figure 4.1. The detection is performed downstream of the flow with a sensitive device. The device can be either, as shown, a SQUID, an atomic magnetometer, or an inductive coil.

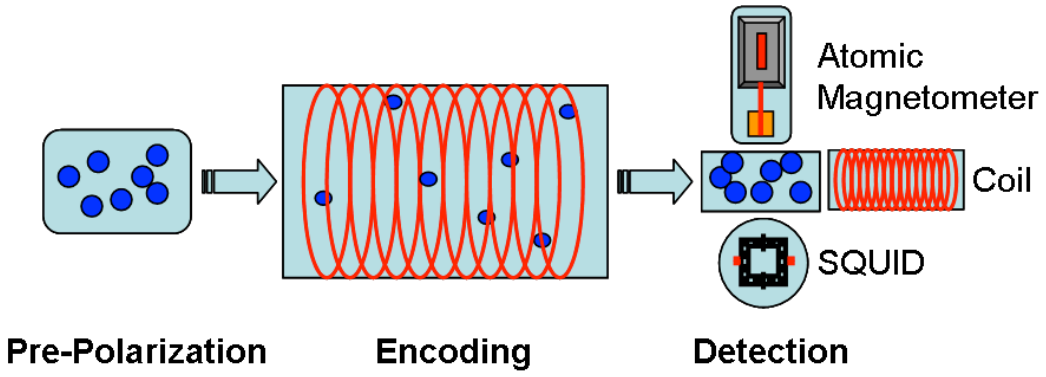

Figure 4.1 Remote detection of MRI.

Optically detected MRI, which refers to MRI using laser-based atomic magnetometers, was first demonstrated by Xu *et al*. using a remote detection scheme [64]. In a later publication, the authors showed that a sub-millimeter spatial resolution

can be achieved in the Earth's magnetic field [93]. Another publication revealed a comparative study on a porous steel stud using both laser-detected MRI and conventional MRI [76]. In his study, laser-detected MRI gave flow images. In contrast, conventional MRI gave no signal due to the penetration problem and field distortion. This result demonstrated the feasibility of using optically-detected MRI to study porous metallic materials. However, no quantitative analysis has been shown. In other words, the property of the host material, such as pore size, connectivity, and other properties of the materials, has not been studied as a function of MRI signal. To extract quantitative information that can be used as guidelines for practical purposes, the sensitivity of optically-detected MRI needs to be improved and new imaging schemes need to be developed.

Before discussing the studies of MRI applications, the basic principles of NMR and MRI are presented.

4.2 Basic concepts of MRI

Magnetic resonance imaging (MRI) is based on the fundamentals of nuclear magnetic resonance (NMR). The first accurate measurement of a nuclear magnetic moment was demonstrated in 1938 by Rabi and coworkers [94, 95]. The existence of such a magnetic moment and the phenomenon of resonance is at the basis of all NMR and MRI theory and experiments.

4.2.1 Nuclear magnetic resonance

NMR is a phenomenon arising in magnetic systems where the nucleus of an atom possesses a magnetic moment due to its angular momentum. When placed in a magnetic field, a nucleus with a magnetic moment can be oriented parallel or anti-parallel to the direction of the field, B_0. There are two possible values for the energy states which correspond to two different orientations:

$$E = \pm\gamma\left(\frac{1}{2}\right)\hbar B_0 \tag{4.1}$$

The difference in the energy in the two states is therefore:

$$\triangle E = \gamma\hbar B_0 \tag{4.2}$$

where $\hbar = h/2\pi$ and h is Planck's constant.

It can be shown that the energy of spins aligned with the field is lower than the energy of the spins anti-parallel to the field (see Figure 4.2). The ratio of the number

of protons populating the two energy levels in the equilibrium state is governed by the Boltzmann distribution:

$$\frac{N_{\uparrow}}{N_{\downarrow}} = e^{-(\gamma \cdot \hbar B_0 / kT)} \tag{4.3}$$

where $N\uparrow$ and $N\downarrow$ are the numbers of protons parallel and anti-parallel to the direction of the B_0 magnetic field, k is Boltzmann constant, and T is the absolute temperature in Kelvin. NMR or MRI experiments measure the total sum of protons' magnetic moments in the sample. This sum is called the macroscopic magnetization, and in the equilibrium state its value is

$$M_0 = \left(\frac{\rho_0 \gamma^2 \hbar^2}{4kT} \right) B_0 \tag{4.4}$$

where ρ_0 is the number of protons per unit volume, or proton density.

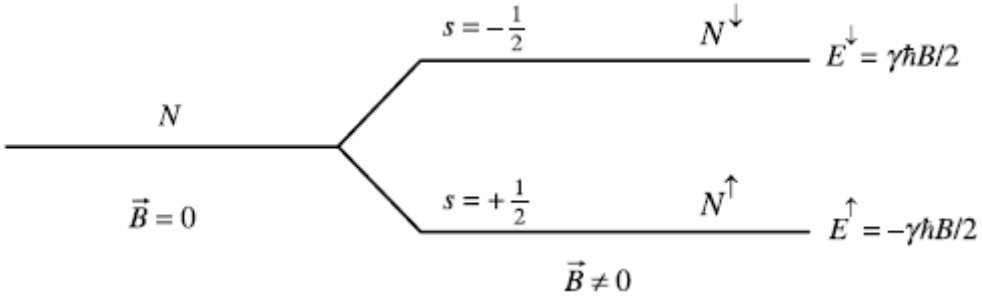

Figure 4.2 Zeeman Energy Splitting. Interaction between protons and the external magnetic field B results in splitting the energy levels. For a large number N of protons, $N\uparrow$ will have s = -½, and $N\downarrow$ will have s = ½, leading to corresponding energies $E\uparrow$ and $E\downarrow$. In the equilibrium state, the ratio of the number of protons populating the two energy levels $N\uparrow/N\downarrow$ is governed by the Boltzmann distribution.

The population difference between parallel and anti-parallel protons, which determines the macroscopic magnetization, is very small. This small population difference, resulting in exceedingly small equilibrium nuclear spin polarization, is largely responsible for the low sensitivity of the NMR, as compared to the other spectroscopic techniques. Increasing the strength of the B_0 field is one way to increase the sensitivity of both NMR and MRI techniques. Another approach to improving sensitivity is to increase the spin population difference by optical pumping as discussed in section 2.2.1. This technique has been used in MRI of the hyperpolarized gases [96, 97]. In addition to these two methods for enhancing the spin polarization, techniques including parahydrogen [98] and dynamic nuclear polarization [99] can be adopted.

4.2.2. Relaxation time constants: T_1 and T_2

To explain how spatial information is encoded in MRI, the topic of relaxation should be mentioned. There are two important types of relaxation time constants that describe the motion of spins exposed to magnetic fields. These time constants are characteristics of the spins being imaged and reveal their molecular environment.

When enough time and an energy-absorbing medium are given, a sample containing a large number of spins exposed to a static magnetic field, B, would become polarized, with a net magnetization, M, along the direction of B. The time-scale of this process is characterized by the relaxation time, T_1. This time determines the rate at which M, initially aligned with B along z-axis, will decay back to the original position if tipped away from it. This process is driven by thermal equilibrium

because M aligned with B corresponds to the lowest possible energy state. Therefore, energy is needed to tip M away from the z-axis and any process that causes T_1 relaxation must take this energy away from the system. The energy can be considered to be removed from the spins and put into the lattice (surrounding). Thus, this T_1 relaxation is defined as the spin-lattice relaxation or longitudinal relaxation, since the effect of this relaxation process is to realignment M back to the z-direction (longitudinal direction).

Besides the process of T_1 relaxation, M will process about B if it is tipped away from it at the rate of precession given by Lamor frequency, ω_0.

$$\omega_0 = \gamma B \tag{4.5}$$

where γ is the gyromagnetic ratio of the nucleus. For hydrogen, $\gamma/2\pi = 42.6$ MHz/T.

Once M is tipped away from the z-axis, it will have x- and y- components referred to as a transverse component: $M_T = (M_x, M_y)$. While T_1 signifies the rate at which M reorients itself back to the z-axis, T_2 indicates the rate at which M_T shrinks or loses magnitude. Therefore, another term for T_2 is the transverse relaxation time. Since M is made up of a sum of spins, interactions with other spins result in an effect on the phase relationship between the spins. Any dephasing of these spins will result in a decrease in the amplitude of M_T. Hence, T_2 is the measure of the rate at which spins are dephased through spin-spin interactions, and referred to as the spin-spin relaxation and it is usually shorter than T_1.

The equation of motion describing the precession of M in a static field B_0 and subject to the relaxation time constants, T_1 and T_2, is called the Bloch equation. It can be written in terms of the three spatial components of M along each axis as:

$$\frac{dM_x}{dt} = \gamma M_y B_0 - \frac{M_x}{T_2} \tag{4.6}$$

$$\frac{dM_y}{dt} = -\gamma M_x B_0 - \frac{M_y}{T_2} \tag{4.7}$$

$$\frac{dM_z}{dt} = -\frac{M_z - M_0}{T_1} \tag{4.8}$$

where M_x, M_y and M_z are the components of M along the x, y and z axes, respectively and M_0 is the magnitude of its longitudinal component at thermal equilibrium. The solution to these equations can be written as:

$$M_L(t) = M_0 + (M_L^0 - M_0)e^{-t/T_1} \tag{4.9}$$

$$M_T(t) = M_T^0 e^{-t/T_2} e^{i\omega_0 t} \tag{4.10}$$

where M_L and M_T indicate the longitudinal and transverse components of M, respectively, with their values at time $t = 0$ given by M_L^0 and M_T^0 and where ω_0 is the Lamor frequency. A diagram of three-dimensional motion of the magnetization vectors and relevant time dependents plots are depicted in Figure 4.3.

4.2.3 Detection of an NMR signal

In MRI, the signal is generated by applying a short-lasting magnetic field perpendicular to B_0, in the xy plane, causing a precession of M about its axis. The magnetic pulse oscillates at the Lamor frequency, which is the precession frequency of the magnetization vector. For conventional MRI, the Lamor frequency is in the

radio frequency (RF) range, so the pulse is often referred to as the RF pulse. Since this signal decays due to loss of M_T caused by T_2 relaxation process, it is commonly referred to as the free-induction decay signal (FID). The MRI signal can be expressed in terms of a complex number with its magnitude and phase.

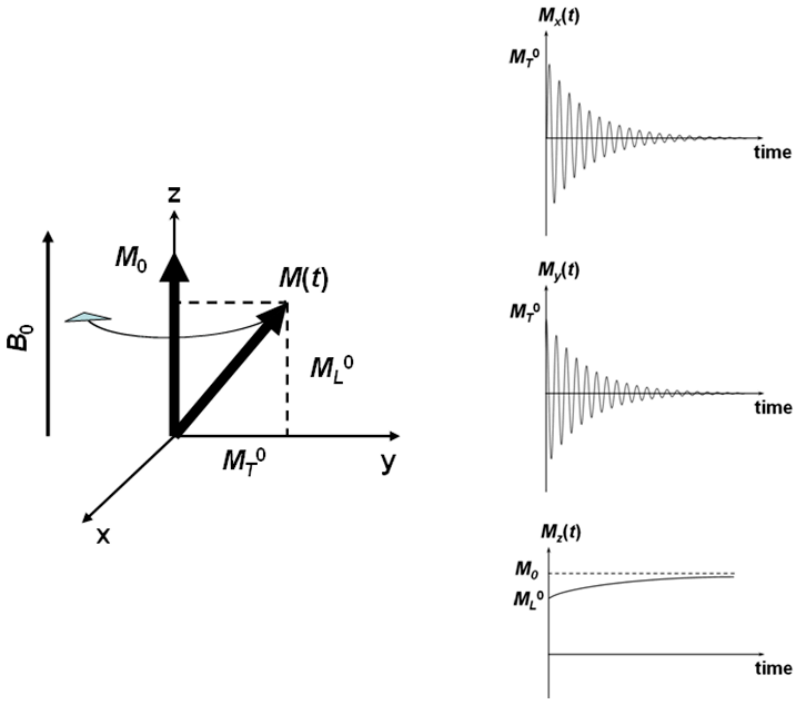

(a) (b)

Figure 4.3 (a) The three-dimensional motion of the magnetization vector. B_0 is the static magnetic field along the z direction, M_0 is the thermal equilibrium state of M and M_L^0 and M_T^0 represent longitudinal and transverse components of M at time $t = 0$, respectively. (b) The components of the magnetization vector as functions of time.

4.2.4 Encoding spatial information in MRI

In order to obtain an NMR signal, the sample or object being imaged must first be polarized. This is accomplished by a main magnet producing a strong, static

magnetic field along the z direction of magnetic B_0. This main field should be homogeneous within the imaging region so that an entire object, placed in this region, experiences the same main magnetic field strength.

The way that spatial encoding is introduced to the sample being imaged, is through the use of field gradients. These are magnetic fields which linearly change in strength along a particular direction. This causes a predictable, spatial variation in the field experienced by the object being imaged.

If a field gradient is turned on for a short amount of time, this will result in a spread of the Lamor frequencies of the spins for the short period. The end result will be that the spins will have accumulated an amount of phase rotation dependent on their position. By repeating this procedure several times with varying G strengths, a collection of phase encoded projections can be obtained. A two-dimensional Fourier transform (2D-FT) of this two-dimensional collection of signals will result in x and y localization, producing a 2D MR image. MR images are digital images, with the localization of the MR signals represented in a grid of small volume elements, called voxels for three-dimensional images, and pixels for two-dimensional images.

Each of the data acquisitions consists of a specific phase encoding signal. To complete a full two-dimensional data acquisition, several phase encoded signals along each dimension are required. This data information is stored in a matrix, called “k-space”. Fourier transformation of this data matrix gives the two-dimensional MR image, as shown in Figure 4.4. Each data in the k-space is a complex number, with real and imaginary components.

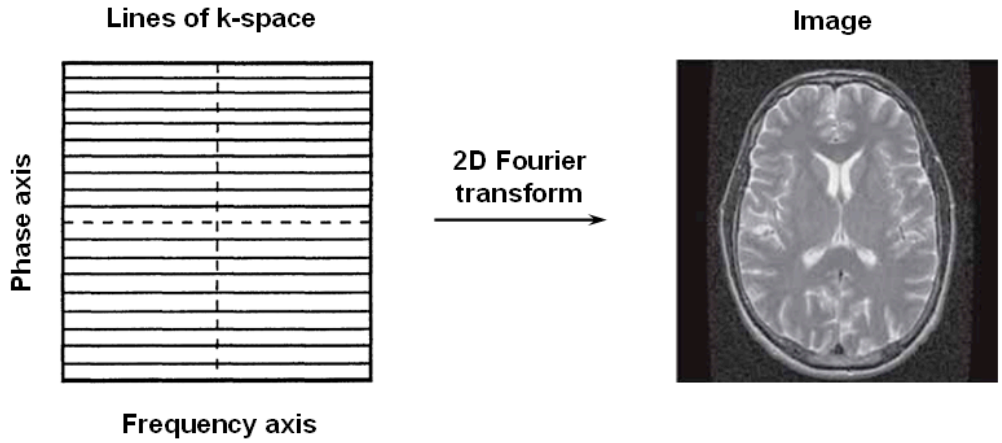

Figure 4.4 After each excitation, the magnetic resonance signal is acquired as a function of time and recorded as a row of numbers in a data array known as k-space. The process is repeated with phase-encoding gradients of incrementally different amplitudes, and each time the signal is recorded as an adjacent line in k-space. After all of the k-space data have been collected, the image is extracted by means of a 2D Fourier transform.

The dimension of the matrices depend on the number of the phase encode steps along each direction. The spatial resolution of an MR image is determined by the field-of-view (FOV)

$$\mathrm{FOV} = \frac{1}{\frac{\gamma}{2\pi} \cdot G \cdot t} \tag{4.11}$$

where G is gradient step size, t is duration of the gradient field.

The spatial resolution is given by

$$\mathrm{Resolution} = \frac{\mathrm{FOV}}{N} \tag{4.12}$$

where N is the acquisition matrix size in a particular direction.

4.3 Experimental methods

Four porous metallic samples (Applied Porous Technologies) that were 6.3 mm in diameter and 10.0 mm long were studied. These samples are referred to as the 0.5-, 10-, 40-, and 100-μm samples by the manufacturer based on the estimated pore sizes. The remote detection scheme was employed for this study, and has been discussed in detail in the previous chapter. Briefly, the fluid flow is driven and recycled by a Micropump with a flow speed of 28 mL/minute. The nuclear spins of water first undergo prepolarization by a 2-T permanent magnet. Flow profiles were obtained by using a single π pulse. Time-resolved flow images, both two-dimensional and one-dimensional, were obtained using a phase-encoding pulse sequence.

Different techniques were also employed to provide more information on the porous steels. Scanning electron microscopy (SEM) and optical microscopy were attempted to characterize the appearance and pore size of the samples. Liquid extrusion porosimetry (Porous Materials, Inc, Ithaca, NY) was used to measure the total pore volume and the porosity. A capillary flow porometer (Porous Materials, Inc, Ithaca, NY) was used to measure the distribution and mean value of the pore diameter in each steel sample.

4.4 Results and discussion

We studied four porous steel samples with different pore sizes. The optical images and SEM images for the samples are shown in Figure 4.5. The optical images show that the roughness differs at the surfaces of the materials. No information on

pore size or bulk property is available. SEM has sufficient resolution to show the pores at the surface, but it cannot provide flow information, which is essential for applications using these materials.

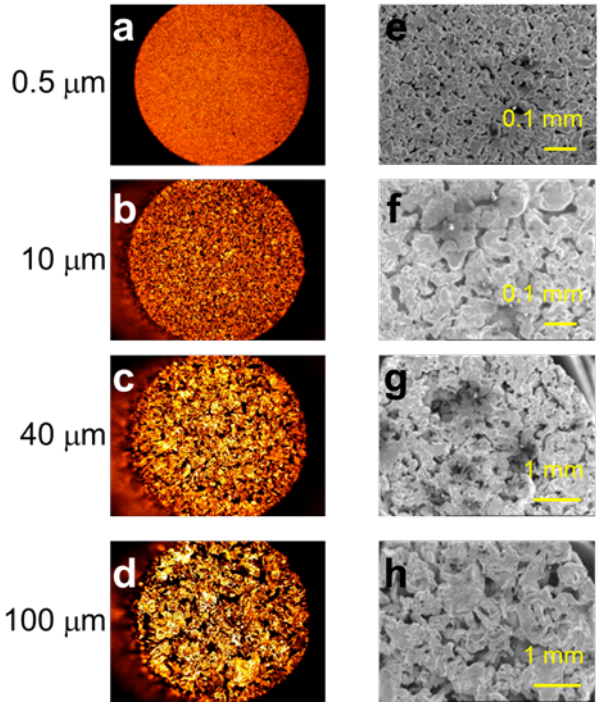

Figure 4.5 Optical images (a-d) and SEM images (e-h) of the four porous metals.

The void volume and average pore size of the samples were measured by liquid extrusion and capillary flow porometry. The results are listed in Table 4.1. The total volume of the samples that were 6.3 mm in diameter and 10.0 mm long was calculated as 0.317 ml. Porosity was calculated by dividing the void volume by the total volume of the samples. The results show that the average pore size increases with the 0.5-, 10-, 40-, and 100-μm samples. In addition, the 0.5-μm sample has a much lower porosity than the other three samples. Its void volume is only

approximately 68% of the other three samples. It is unclear why the 0.5-μm sample has an apparent lower porosity using these techniques. No information on the flow dynamics is available from these measurements.

Table 4.1 Void volume, porosity, and average pore size of the porous metals.

Sample Name	Void Volume (ml)	Porosity (%)	Average Pore (μm)
0.5	0.099	31	2±1
10	0.145	46	10±8
40	0.160	50	20±20
100	0.147	46	50±50

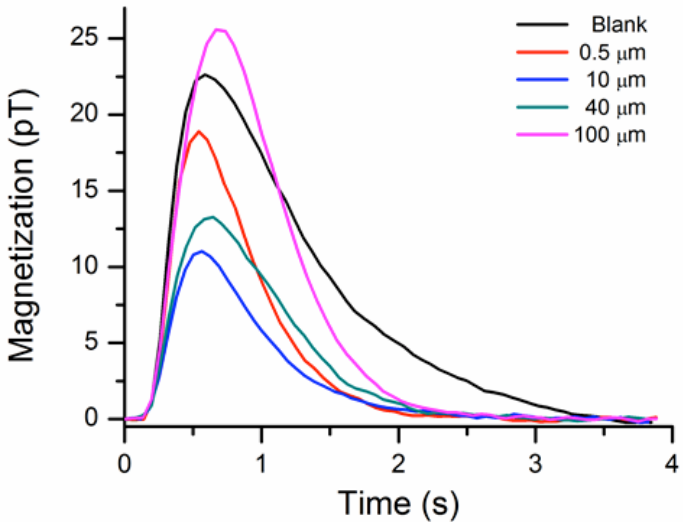

Figure 4.6 Flow profiles for the porous steel samples and the blank sample.

To obtain the flow information for the porous steels, we first measured the flow profiles for water through the samples. The results are shown in Figure 4.6. The flow time is defined as the duration between the start of phase encoding and when the encoded water reaches the detection region. There are three important observations

from these flow profiles. First, the flow profiles are all narrower for the porous steels than for the blank sample, which did not contain a steel sample but contained empty volume. Second, the magnitude is higher for the 100-μm sample than for the blank sample, while the other three samples have lower amplitudes compared with the blank sample. Third, the flow profile in the 0.5-μm sample has higher amplitude compared with the 10-μm and 40-μm samples. This result seemingly contradicts the general trend that nuclear spin polarization decreases with a decrease in pore size because the spins relax faster inside the smaller pores [100].

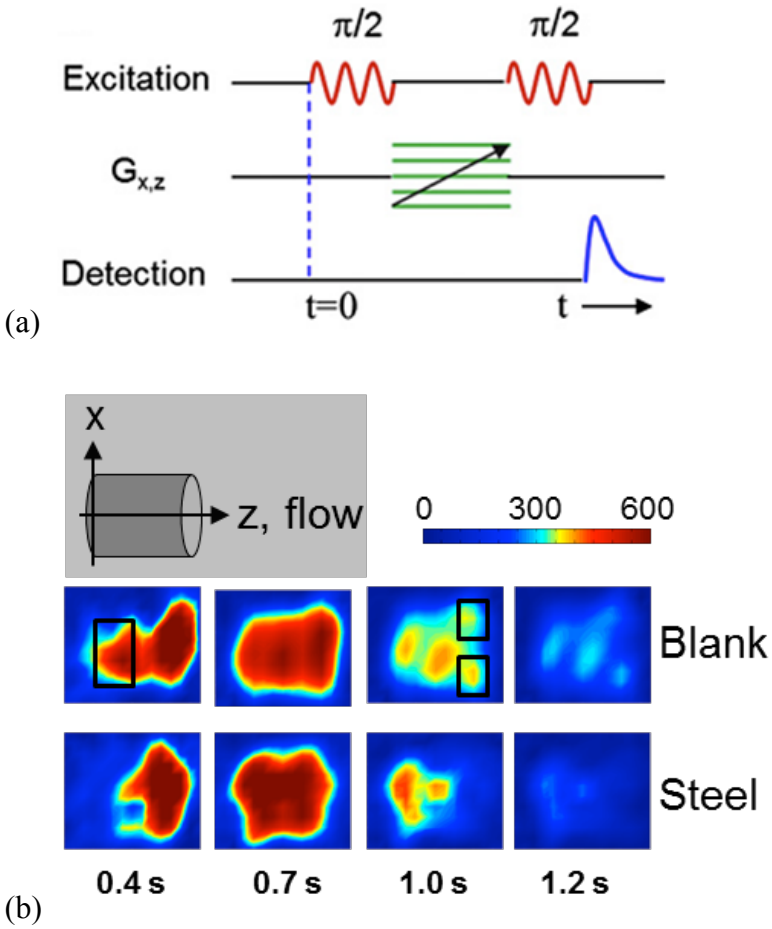

Figure 4.7 MR images of the flow inside the blank and 100-μm steel samples. (a) The pulse sequence (b) 2D Images. The inset in grey depicts the axes and flow direction.

To better understand these observations, we then conducted two-dimensional imaging for the 100-μm sample and the blank sample to compare the spatially and temporally resolved flow behaviors. The MR images are shown in Figure 4.7b. The flow direction is along the z-axis, which is the center of the cylindrical samples; the x-axis is perpendicular to the z-axis (inset in Figure 4.7b). The pulse sequence is shown in Figure 4.7a. The gradient steps are 4 mG/mm for the z-axis and 6 mG/mm for the x-axis. The duration of the gradients is 5 ms. The flow time here is the duration between the first $\pi/2$ pulse and when the encoded water reaches the detection region. Comparing the images at 0.4 s, a region with a small z (the far end to the detection region) appears in the image for the blank sample but not the porous steel sample. This region appeared because the flow in the blank sample is approximately laminar flow; therefore, a portion distal to the downstream detector but proximal to the center axis (the region highlighted with a black box) reaches the detector early. When a porous material is present, the laminar flow profile is altered to more resemble block flow. Then, at a later time (1.0 s), the region most proximal to the detection region but not on the center axis remained in the blank sample, which is indicated with two black boxes. This region has a slower velocity in accord with laminar flow characteristics. In contrast, the image at 1.0 s in the porous steel does not depict such regions. Therefore, the 2D images explain how the flow profiles for the steel samples are narrower compared with the blank sample. The flow behavior observed in this work is similar to the results of a high-field MRI study on porous organic polymers [101].

More quantitative details can be observed using one-dimensional (1D) imaging along the x-axis (Figure 4.8). The 1D profile for the steel sample is broader at 0.7 s but narrower at 1.2 s compared with the blank profile. This result is consistent with

observations from the two-dimensional images. In addition, the signal amplitude for the steel sample is higher at 0.7 s but lower at 1.2 s compared with the blank sample, which is consistent with the flow profiles in Figure 4.6. Furthermore, the 1D profiles for the steel sample are less symmetric at the z-axis (x = 0) compared with the blank sample likely because the pore distribution is not homogeneous.

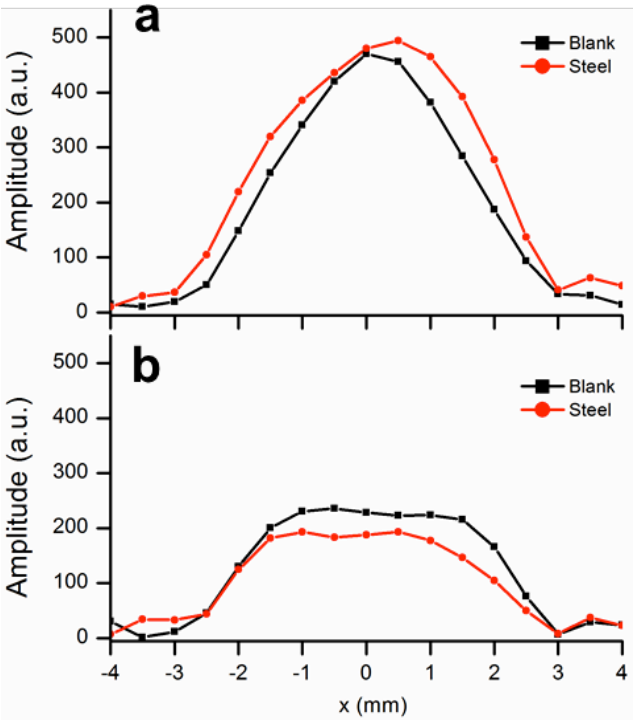

Figure 4.8 One-dimensional images for the blank and 100-μm steel samples at 0.7 s (a) and 1.2 s (b).

The higher signal that was observed for the 100-μm steel compared with the blank sample is likely due to the volume difference between these samples. The void volume is 0.146 ml for the steel sample and 0.317 ml for the blank sample.

Consequently, the water protons relax for a longer time after polarization in the blank sample. Therefore, the overall signal is apparently weaker. The signals in the 40-μm and 10-μm samples are lower compared with the blank sample because the enhanced relaxation by the steel samples with smaller pore sizes outweighs the initial relaxation effect.

The signal for the 0.5-μm steel sample is higher compared with the signals for the 40-μm and 10-μm samples. This result can be explained using similar logic: the volume in the 0.5-μm sample is lower than the volume in the other two steel samples; therefore, the sample yields a less relaxation time under the same flow rate. However, the volume decrease cannot be discerned from the flow profile alone.

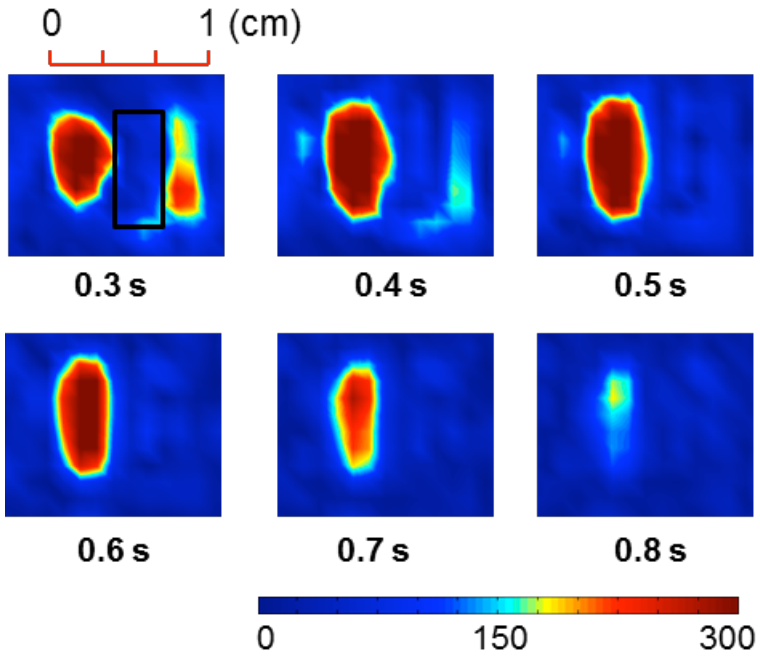

Figure 4.9 Optically detected MRI depicts a clogged region in the 0.5-μm steel sample.

We performed two-dimensional imaging for the 0.5-μm sample (Figure 4.9). The images depict a clogged region, which is located at the middle one-third of the sample and is most clear in the image at 0.3 s. The size is consistent with volume loss compared with the other porous samples, because the percentage volume loss is approximately (0.145 – 0.099)/0.145 = 32%, which is consistent with the size of the clogged region. This clogged region was not detected by either optical microscopy, SEM techniques (Figure 4.5) or conventional techniques for characterizing porous materials.

Chapter 5

High–resolution optically detected MRI in an ambient magnetic field

5.1 Motivation of the study

Magnetic resonance imaging (MRI) in an ultralow magnetic field usually has poor spatial resolution compared to its high-field counterpart regardless of which detection technique is used. In addition to the low nuclear magnetization in an ultralow field even via pre-polarization compared to that in a high magnetic field (>1 T), one main reason for the poor spatial resolution is the concomitant field effect, which imposes an upper limit on the gradient field [102, 103]. For instance, for a 10 × 10 imaging of a 1 cm × 1 cm area, the maximum gradient field is approximately 5 μT/cm to avoid substantial image distortion. The situation is particularly severe under ambient conditions because the significant heterogeneity of the magnetic field imposes a lower limit on the gradient field. For example, the homogeneity of the

ambient magnetic field in a laboratory environment is approximately 0.1–0.2 μT/cm. This value sets a lower limit of approximately 1 μT/cm for the gradient field. Therefore, the appropriate range for the amplitude of the gradient field is small. Consequently, the spatial resolution is constrained. Several methods for image correction have been proposed and have been experimentally implemented [104–106]. However, the spatial resolution for ultralow-field MRI has not reached sub-millimeter resolution for both of the in-plane axes.

An additional issue that limits the spatial resolution of ultralow- field MRI is the low detection efficiency of the alternative techniques. For optical detection with atomic magnetometers, the atomic sensor is usually placed in the vicinity of the nuclear spins. The filling factor is not as optimal as that of an inductive coil, which usually encloses the entire sample. Although the innovative idea of using a flux transformer has been successfully demonstrated, this method only has good sensitivity at approximately 100 kHz because it is based on Faraday induction [30,107]. Thus, this method is not suitable for investigating metallic materials. New configurations are needed to improve the filling factor in ultralow magnetic fields, and this improvement will eventually also improve the spatial resolution.

5.2 An Image artifact in very low field MRI: Concomitant effect

While MRI at very low magnetic fields has certain potential advantages, it may also face problems that are not typical for MRI at conventional and high field

(0.1–10 T). Major differences arise due to the presence of the undesirable artifact effects of concomitant components of inhomogeneous magnetic field (gradients) that are transverse to the major B_z field, B_o. These concomitant transverse field components are unavoidably created by the same gradient coils used to encode spatial information in MRI. The concomitant gradients artifacts occur when the product of the magnetic field gradient and the dimension of the sample become comparable to the static magnetic field. The parameter that measures the concomitant field effect is given by

$$\varepsilon = GL/B_0, \qquad (5.1)$$

where G is the gradient magnetic field, L is the dimension of the FOV, and B_0 is the leading magnetic field [106, 108, 109].

For most MRI techniques at conventional magnetic fields, the concomitant fields do not impose significant problems as the effective magnetic field defining the Larmor frequency differs only slightly from B_z. However, in a very low field scanner (several mT or even μT), the transverse concomitant magnetic field created by the gradients may be on the order of or even larger than B_0. This will create substantial artifacts in the imaging experiment. A similar problem will exist for imaging in the Earth's magnetic field [110]. Such artifacts will be most pronounced in MRI at micro-Tesla fields [111, 112].

Here, we present a zoom-in imaging method that overcomes the concomitant field effect in an ambient magnetic field. Sub-millimeter resolution has been obtained through the clear revelation of a 0.6 mm gap between two flow channels. Through the implementation of a gradient solenoid, the filling factor, and hence, the detection

efficiency, is significantly improved. The resultant higher signal level enhanced the spatial resolution.

5.3 Experimental methods

Figure 5.1a shows the concept of the zoom-in method. Assuming a field of view (FOV) of 10 cm × 10 cm, a 100 × 100 grid is needed to achieve spatial resolution of 1 mm × 1mm (Figure 1a, left). Such a large number of encoding steps will most likely make the maximum gradient field comparable to or larger than the ambient field, giving that the gradient field has a lower limit determined by the field inhomogeneity. Therefore, the concomitant field effect will be severe. In other words, it is difficult to obtain 1 mm × 1 mm resolution. However, we can instead focus on one (or a few) region(s) of interest by initially imaging a 10 × 10 grid. The significantly reduced number of steps will not cause the concomitant field effect. Then, the center of the gradient stack is moved to the region of interest. A second 10 × 10 image on the reduced field of view is performed (Figure 1a, right). The net result is that for the region of interest, a high resolution of 1 mm × 1 mm is obtained and the concomitant field effect is avoided because of the reduced field of view.

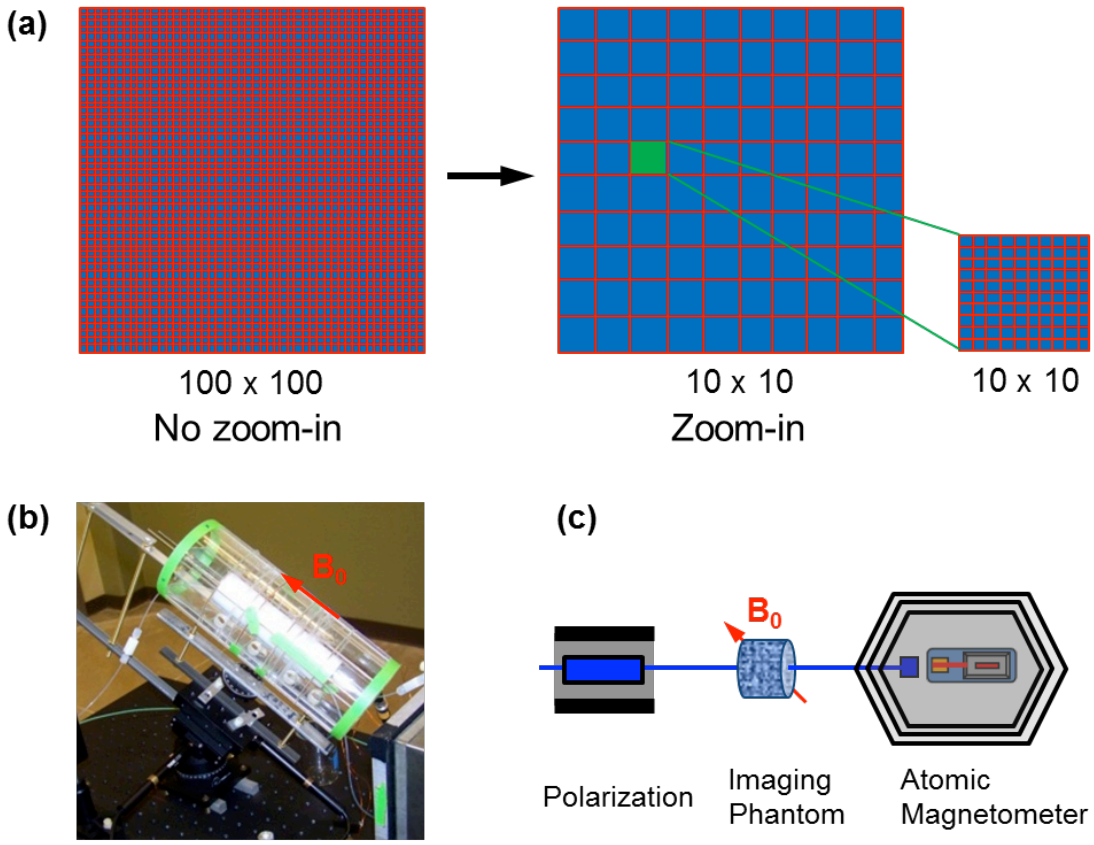

Figure 5.1 Experimental details: (a) Schematic of the zoom-in method. The left panel shows the ordinary imaging method with no zoom-in. The right panel shows the zoom-in method, which consists of two 10 × 10 grids that achieve the same spatial resolution as the ordinary 100 × 100 grid, but only for a region of interest (in green). (b) The coil stack is mounted on a two-dimensional translation stage; the orientation of the coil stack is aligned with the ambient magnetic field B_0. (c) Scheme showing the optically-detected ultralow-field MRI of the flow.

The zoom-in method requires two conditions. One condition is that the gradient stack be mobile. This condition is easily satisfied for ultralow-field MRI because the gradient coils are open, lightweight, and use very low current; thus, the

coils have high mobility. Figure 5.1b shows the gradient stack mounted on a two-dimensional translation stage. The other requirement is that the magnetic field B_0 be large in size, so that there is room to move the gradient coils to obtain different FOVs and so that the movement is not physically restricted by the magnet. This requirement is easily met by the ambient magnetic field produced by the Earth.

An optical atomic magnetometer is used to detect nuclear magnetization with a remote detection scheme (Figure 5.1c). Here, prepolarization is achieved with a 2-T permanent magnet. Spatial encoding is performed in the ambient magnetic field. The encoded nuclear spins in water flow inside the detection region, which is inside a multilayer magnetic shield where an atomic sensor resides. The sensitivity of the atomic magnetometer is approximately 80 fT/(Hz)$^{1/2}$ for near-dc magnetic signals.

The imaging phantom is shown in Figure 5.2a. The phantom consists of two channels, both 4.0 mm in height but with different widths; one channel is 1.9 mm wide, and the other is 1.6 mm. The gap between the channels is 0.6 mm. The overall length of the phantom is 10 mm. The translation stages, one for the x-axis and one for the z-axis, have a movement range of 25 mm.

The pulse sequence is similar to the phase encoding sequence used previously (Figure 5.2b) [29, 113]. The excitation frequency is 2.045 kHz, which corresponds to a magnetic field strength of 48 μT. The duration of the 90^o pulse is 6 ms, and the gradient field duration is 5 ms. Phase cycling is used for the second 90^o pulse. The field inhomogeneity is measured to be 0.1 μT/cm perpendicular to B_0 (x- and y-axes) and 0.2 μT/cm along B_0 (z-axis). The gradient strength $\Delta G_{x,y}$ was 3.5 μT/cm for the first step of the zoom-in process. For the second encoding step, after moving the gradient stack, ΔG_x was 7.0 μT/cm. ΔG_y was 3.5 μT/cm.

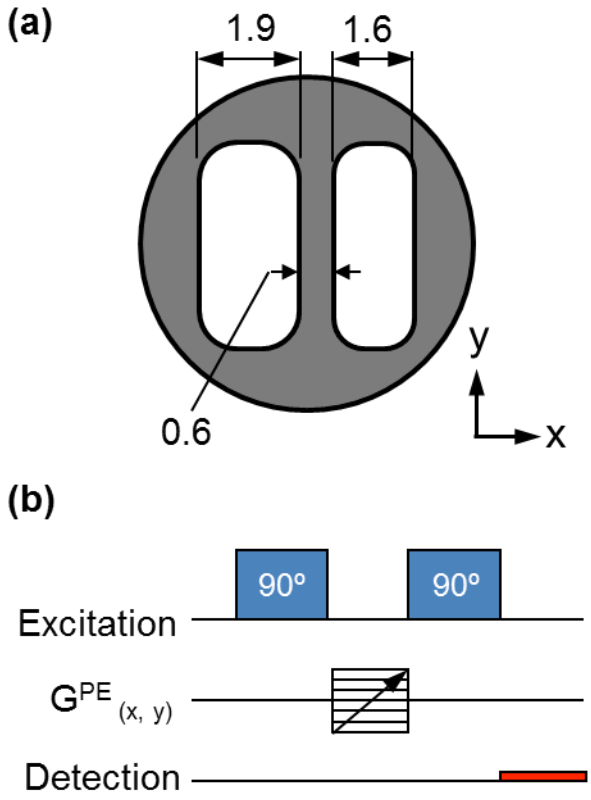

Figure 5.2 Imaging phantom and pulse sequence: (a) Drawing of the phantom with two flow channels with 0.6 mm edge-to-edge spacing. Unit: mm. (b) Pulse sequence. $G^{PE}(x, y)$: Phase encoding gradient field along x- and y- axes. The atomic magnetometer measures the magnetization downstream, as indicated by the red line.

A gradient solenoid was used to guide the nuclear spins while the spins flowed into the detection region inside the magnetic shield (Figure 5.3). The winding was tight at the left side, which was placed in the ambient magnetic field, and gradually widened toward the right end, which was placed inside the magnetic shield. A DC power supply was used to deliver a constant current to the solenoid. The current was adjusted to maximize the signal. The diameter of the solenoid was 6.5 mm, and the

length was 14 cm. The solenoid was hollow so water could flow from the encoding region to the vicinity of the atomic sensor for measurement.

Figure 5.3 The gradient solenoid used to improve the detection efficiency.

5.4 Results and discussion

Figure 5.4 shows the MR images of water flowing through the phantom at the time of the maximum signal. In Figure 5.4a, an 11 × 11 grid was used and the FOV was 13 mm × 13 mm. Therefore, the spatial resolution was 1.2 mm × 1.2 mm. Clearly, this resolution was unable to reveal the gap between the two channels. The image in Figure 5.4a showed that the region of interest is approximately 2 mm (indicated by d on the image) from the center of the FOV. Thus, we then moved the gradient stack to the left by 2 mm to magnify the region of interest. The gradient field ΔG_x was doubled to 7.0 μT/cm while ΔG_y remained 3.5 μT/cm. Therefore, the spatial resolution along the *x*-axis was doubled to 0.6 mm. The resulting image is shown in Figure 5.4b. The finer spatial resolution was able to resolve two channels; this resolution was lacking in the previous image.

The concomitant field effect was avoided through the simultaneous increase in the gradient strength and reduction in the FOV. Based on this concomitant field effect

equation 5.1, the zoom-in method keeps ε constant through a simultaneous increase in the gradient and a decrease in the size of the FOV. However, the spatial resolution is improved. In addition, the new FOV is adjusted to the region of interest. This adjustment is important because without the spatial mobility, the region of interest, indicated by a green box in Figure 5.4a, would be partially outside of the reduced FOV.

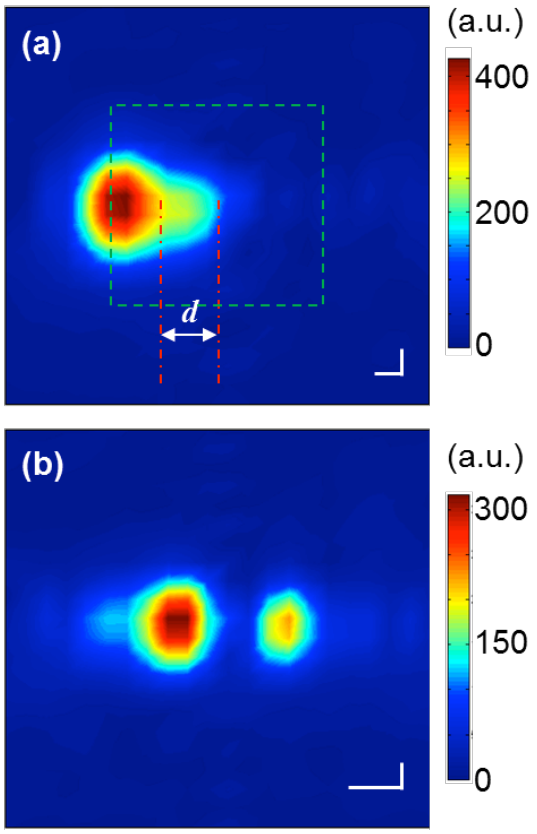

Figure 5.4 Results of using the zoom-in method for ultralow-field MRI in an ambient magnetic field: (a) MR image before zoom-in, in which the green box indicates half of the FOV. (b) Zoom-in MR image after the coil stack was moved to the left by 2 mm and the gradient field on the horizontal axis was doubled. The scale bars indicate 1 mm.

Figure 5.5 shows the image with a reduced FOV along both the *x*- and *y*-axis by a factor of 2, via increasing the gradient duration to 10 ms. Therefore, the spatial resolution was 0.6 mm × 0.6 mm, which is the highest resolution for ultralow-field MRI under similar conditions. The black traces on the image show the actual sizes of the flow channels; these sizes match the MR image well. The connection between the two channels possibly arises from the reduced signal-to-noise ratio of the image or from the area at the ends of the two channels where the channels connect. Note that the amplitude of the signal is substantially lower than that of the images in Figure 5.4 because of the reduced pixel size.

To demonstrate the concomitant field effect for comparison, we performed MR imaging with the same FOV as Figure 5.5, but twice gradient *G*. Therefore, ε became 0.5, a two-fold increase from the value for the image in Figure 5.5. The image is shown in Figure 5.6. Severe distortion was observed in the image. It did not show the appropriate dimensions of the phantom, in contrast to the image in Figure 5.5.

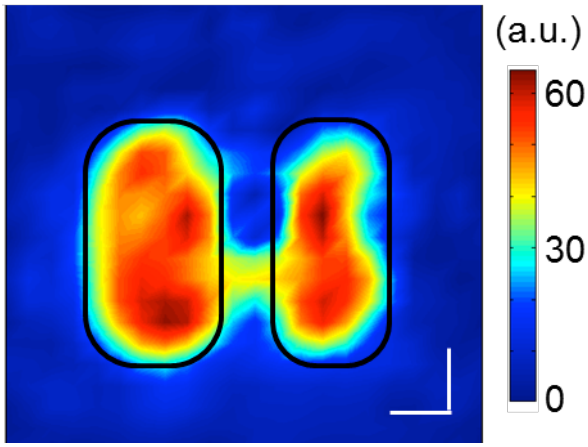

Figure 5.5 Zoom-in MR image acquired by doubling the gradient field along both axes, with scale bars indicating 1 mm.

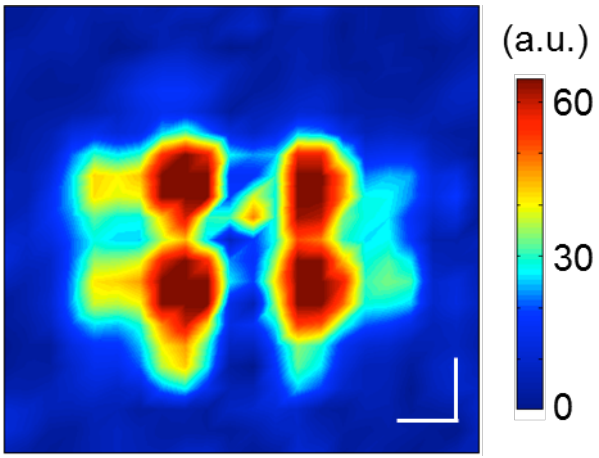

Figure 5.6 MR image to show the concomitant field effect, with gradients 7 μT/cm for both axes, with scale bars indicating 1 mm.

The zoom-in method not only improves the spatial resolution and overcomes the concomitant field effect for ultralow-field MRI, it also significantly reduces the experimental time required to image continuous flow. This reduction is because the total number of encoding steps is substantially lower with the zoom-in method. For example, a 100 × 100 grid requires 10^4 encoding steps with pure phase encoding whereas two 10 × 10 grids only require 200 encoding steps. Even if there are five regions of interest, the total imaging time is still reduced 10-fold. The reduction in the number of steps is significant in ultralow-field MRI because prepolarization, which usually takes a few seconds for each step, is the speed-limiting process.

A clear disadvantage of the zoom-in method is that it does not provide a high-resolution image of the entire FOV. However, this entire high-resolution image may not be necessary for many applications, where localized images will suffice instead. For example, the identification of clogged regions in a metallic substrate does not require high resolution over the entire FOV [113]. Additionally, medical imaging for

diseases often focuses on localized regions with abnormalities. In these cases, our zoom-in method provides a practical approach to high-resolution ultralow-field MRI.

In addition to the concomitant field effect, another parameter that relates to spatial resolution of ultralow-field MRI is the signal amplitude. This is because the voxel size will become smaller at higher resolution; in order to obtain images with the same signal- to-noise ratio within the same data acquisition time, signal amplitude needs to be improved. If the sensitivity of the detector is fixed, the filling factor of the detector needs to be improved to increase the signal amplitude. This coupling problem is particularly significant for ultralow-field MRI because its signal-to-noise ratio is usually poor compared to high-field MRI.

We attempted to improve the spatial resolution by increasing the signal amplitude. In optical detection, a guiding magnetic field is essential to allow the nuclear spins to pass through the multilayer magnetic shield [29, 114]. The guiding field cannot interfere with the near-zero magnetic field needed for the atomic magnetometer in our detection scheme. Previously, a long piercing solenoid was used for the nuclear spins and the atomic magnetometer was placed outside of the middle of the solenoid. This configuration ensures that the atomic sensor does not experience the magnetic field produced by the solenoid. However, this geometry increases the distance between the sample and the atomic sensor. An alternative approach used a pulsed magnetic field to transport the nuclear spins, and this pulsed field was turned off during the measurement [31]. This approach is not suitable for the imaging of a continuous flow.

The gradient solenoid shown in Figure 5.3 provided a magnetic field that gradually decreased from the outside of the magnetic shield to the atomic sensor

inside the magnetic shield. The magnetic field of the gradient solenoid bridged the ambient magnetic field outside of the magnetic shield (48 μT) and the near-zero magnetic field where the atomic sensor resided (~0.2 μT). In practice, a current of 0.1 A was used for the solenoid. The magnetic field generated by the last two loops on the solenoid at the atomic sensor position was estimated to be approximately 3 nT. Such a small field would not affect the sensitivity of the magnetometer. Figure 5.7a shows the two magneto-optical resonance profiles with and without current in the solenoid. It can be observed that the resonance feature was not broadened after current was supplied to the solenoid. The 7 Hz frequency shift in Figure 5.7a indicates that a magnetic field of 1 nT was produced by the solenoid; this value is consistent with the estimate of 3 nT as shown in the magnetic field mapping in Figure 5.8 and Figure 5.9 The estimations were done by using MATLAB. The MATLAB scripts are shown in Appendices A4 and A5, following the equations in Appendix B. The lower value is most likely because of the shielding of the innermost layer of the magnetic shield.

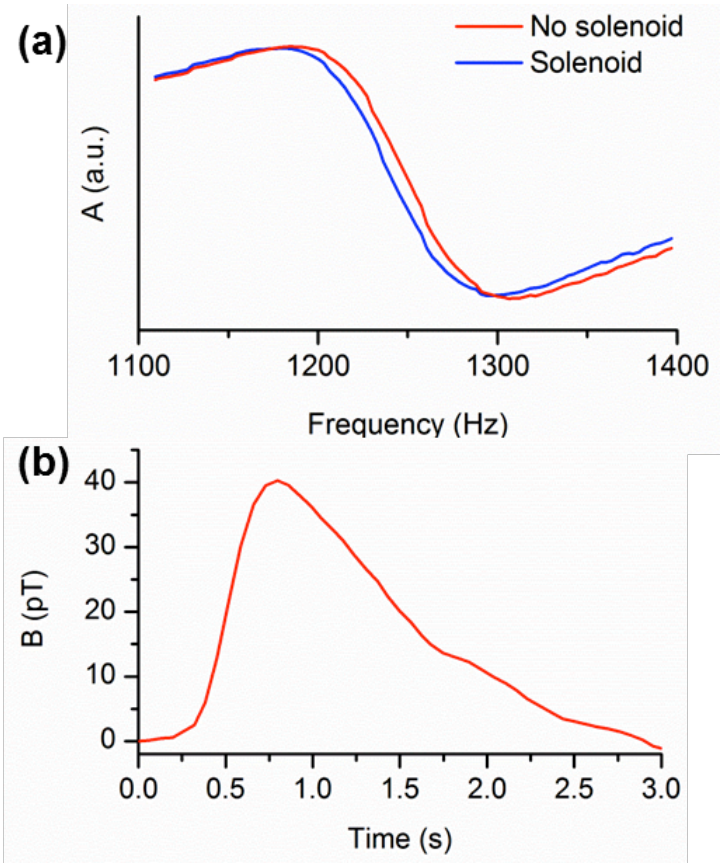

Figure 5.7 Improvement of the detection efficiency with a gradient solenoid: (a) magneto-optical resonance profiles with and without the gradient solenoid; (b) water flow profile measured by the atomic magnetometer with a gradient solenoid.

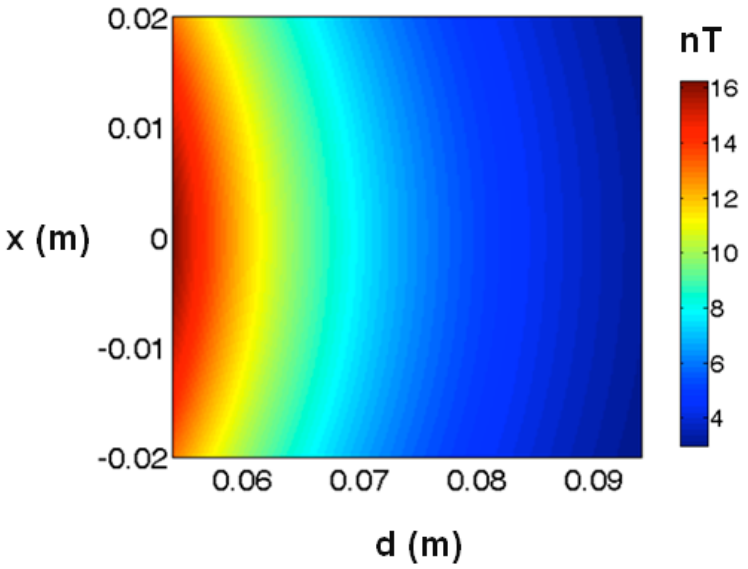

Figure 5.8 Magnetic field mapping of a plane parallel to the gradient solenoid. The estimate amplitude at the atomic sensor, on the center right edge, is 3 nT.

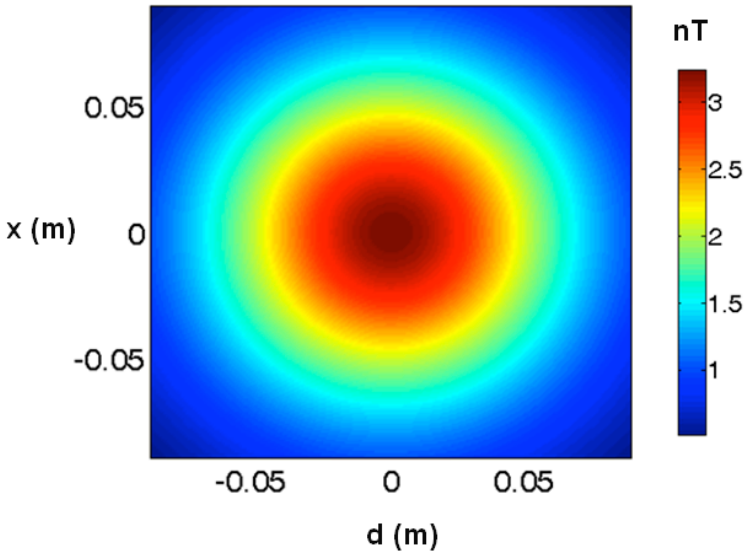

Figure 5.9 Magnetic field mapping of a plane perpendicular to the gradient solenoid. This map exhibits consistent estimate amplitude at the atomic sensor (at the center).

Figure 5.7b shows the nuclear magnetization measurement for flowing water. A single 180^{o} pulse was applied to invert the spins in the ambient magnetic field. Time zero was set to be the beginning of the pulse. The high amplitude shows that the gradient solenoid effectively guides the nuclear spins that are transported from the ambient magnetic field to the near-zero field. Compared to previous results with a piercing solenoid [113], the signal was nearly twice as high. Such an increase is substantial given the usually low signal for ultralow-field MRI.

The increase in the signal amplitude can be explained by the improvement in the filling factor. Figure 5.10 shows the schematics of the two different configurations. Based on the geometry, the distance between the sample and the atomic sensor was significantly shorter when the gradient solenoid was used. The reduction factor was about 1.25, from 10 mm to 8 mm approximately. Because of the r^{-3} dependence of magnetic field, where r is the distance between the sample and the sensor, the signal should increase by nearly a factor of 2. This prediction is consistent with the experimentally measured signal improvement. The increase in the signal facilitates the improvement in spatial resolution through the zoom-in scheme. This facilitation occurs because when the spatial resolution increases, the smaller voxel size contains fewer nuclear spins. The higher detection efficiency helps improve the quality of the images.

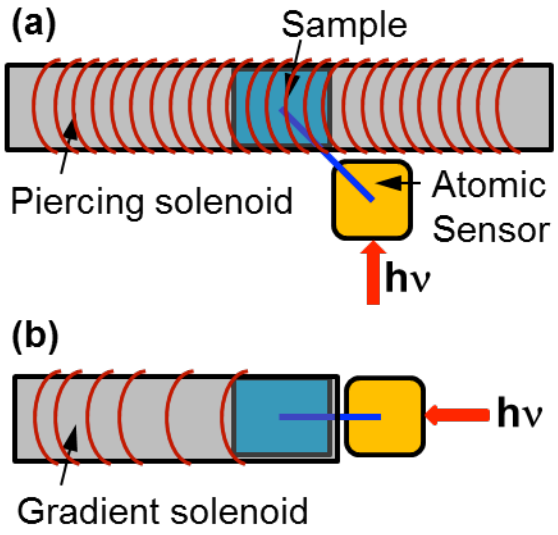

Figure 5.10 Comparison of the filling factors for (a) a piercing solenoid and (b) a gradient solenoid. The blue bars indicate the average distances between the sample and the atomic sensor. The detection axis is determined by the indicated propagation direction of the laser.

Although the idea of a gradient solenoid is specifically useful for the imaging sequence shown here, the zoom-in method is generally applicable for ultralow-field MRI, whether optical detection is used or not. The method avoids the concomitant field effect, and sub-millimeter resolution can be achieved in the ambient magnetic field. However, the resolution is ultimately limited by the sensitivity of the detection technique and the filling factor. These limits require further development of the detection techniques.

It remains difficult for ultralow-field MRI to compete with high-field MRI under situations where both are applicable. Nevertheless, ultralow-field MRI has not nearly reached its limit. For example, recent work by Romalis and coworkers has

demonstrated a sensitivity of 0.16 $fT/(Hz)^{1/2}$ [28]. Kitching and colleagues significantly improved the sensitivity of miniaturized atomic sensors [27]. Such high sensitivities have not been used for MRI. Through the coupling of sensitivity improvements and the new methods developed here, optically-detected ultralow-field MRI can find a wide range of applications. The technique will be particularly valuable in situations where high-field MRI is not applicable, including samples with high magnetic heterogeneity, systems involving metallic materials, and scenarios that require portability.

Chapter 6

Selective polarization and nuclear spin relaxation for different fluids

6.1 Selective polarization

6.1.1 Motivation of the study

Selective polarization of a sample in a specific channel provides significant values for studying flow and mixing in chemical reactions, petrochemical industries or chemical and biological applications in microchips. Controlling flow of chemical processes requires detailed information, for example, analyte distribution in multiple channels, flow dynamics and mixing behavior [115-118]. Fluorescent detection provides highly sensitive means of sensitive fluid tracking techniques used to monitor the flow phenomena [119-122]. However, they are not applicable in many applications.

Selective polarization is a noninvasive labeling method involving only nuclear spins. The flow dynamics and distribution of the reactants in the labeled channel can

be attained before, at some point in, and after it undergoes chemical reactions [78]. Unlike other chemical labeling techniques, e.g., fluorescent and magnetic labeling, the nuclear-spin labeling technique does not disturb the ongoing reactions or biological processes. This technique also overcomes selective pulses limitation encountered in high-field MRI, for example, high-field MRI is limited only to one slice or one voxel in the encoding volume whereas it is applicable to a channel with arbitrary shape and multiple channels in low-field MRI.

6.1.2 Experiment

The flow behavior of fluids can be revealed by using selective pre-polarization, a unique advantage for low-field MRI. A schematic of selective pre-polarization is shown in Figure 6.1. The fluid of interest indicated as Fluid 1, goes through the pre-polarization magnetic field, B_{pre}, to build up the initial polarization. The other component, denoted as Fluid 2, is not allowed to pass the magnetic field. Therefore, Fluid 2 gives no detectable magnetic resonance signal. To study distribution of nuclear spins of fluids, water was used in this experiment and flow through porous steel samples. From this setup configuration, the essential information about the effect of one fluid on the other in a particular material was obtained.

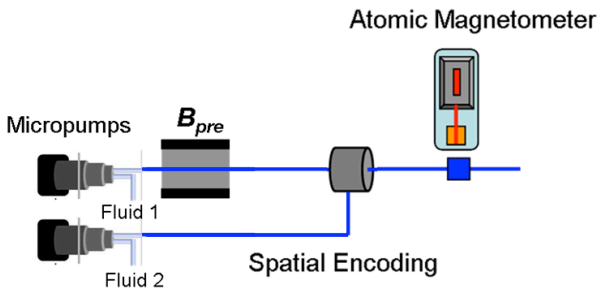

Figure 6.1 Selective polarization.

The sample holder is composed of two channels on the input side, and one channel on the output side with the same diameter as in Figure 6.2. Polarized water flows through channel 1, whereas nonpolarized water passes through the side channel.

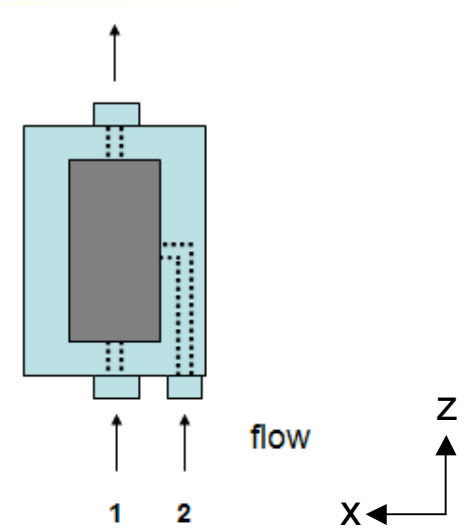

Figure 6.2 The sample holder consists of two input channels and one output channel. Polarized water flows through channel 1, whereas nonpolarized water passes through the side way, channel 2. The flow direction is along *z*-axis.

To obtain flow information of the porous steels for selective polarization, flow profiles of water, again, through the samples were studied. The results are shown in Table 6.1. For spatial encoding, a two-dimensional phase encoding pulse sequence was used: the duration of the excitation pulse was 6 ms; the step sizes of the gradient fields were 2.6 and 3.3 mG/mm for the *z* and *y* axes, respectively. The duration for the gradient-field pulses was 5 ms.

Table 6.1 Comparison of signal amplitudes of the sample holder, the sample holder with bypass channel and with 100 μm porous steel sample inserted.

Samples	Signal (pT)
Blank	**42**
Bypass	**25**
Bypass + metal	**21**

The signal amplitude of the sample holder with bypass channel, termed as bypass sample holder, decreases to almost half of that of the original blank sample holder, 42 pT as indicated in section 5.4. This is consistent with the fact that fluid from one channel is not prepolarized. In addition, the speed of the polarized water in channel 1 was set a little higher, by using a smaller diameter tube, ∅ 0.02 mm, to dominate the effect of the prepolarized water over the other channel, ∅ 0.03 mm. Interestingly, the signal amplitude of the bypass holder is more than a half of the amplitude of the blank sample holder. These are consistent with the higher speed of the prepolarized water in the main channel over the bypass channel. Furthermore, the signal amplitude of the bypass sample holder with 100-μm metal inserted is lower than that of the bypass sample holder, which is opposite to the normal flow experiment in chapter 4. Non-polarized water from the side channel deteriorates signal drastically. This is probably because of less void volume of 100-μm sample compared to the blank bypass sample holder. Therefore, enhanced relaxation of 100-μm sample significantly dominates the initial relaxation effect of the blank bypass sample holder.

To further explain these observations, we conducted more studies on two-dimensional (2D) imaging for the bypass sample holder with and without the 100-μm sample in order to compare flow behaviors.

The images in Figure 6.3 show no observable signal from the unpolarized water from the side input channel. Only polarized water in the 2-T field at the center can be seen in MR images. The resolution is 2.0 mm for the *z* axis and 1.3 mm for the *y* axis. The total signal amplitude is approximately a half of that observed when both channels are filled with polarized water.

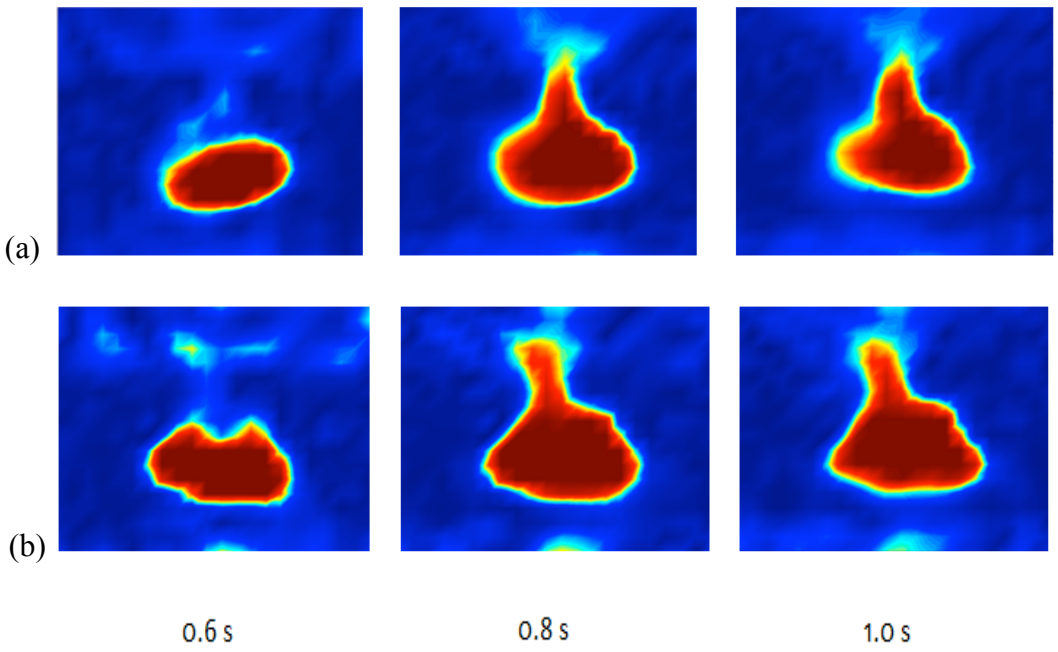

Figure 6.3 MR images along (a) *yz*- and (b) *xz*-planes of selectively polarized water in the sample holder with bypass channel.

The images of selectively polarized water in the sample holder with bypass channel with 100-μm porous steel sample are shown in Figure 6.4. The area of the non-polarized water can be seen from the low intensity (blue) region in the middle of images of the sample holder.

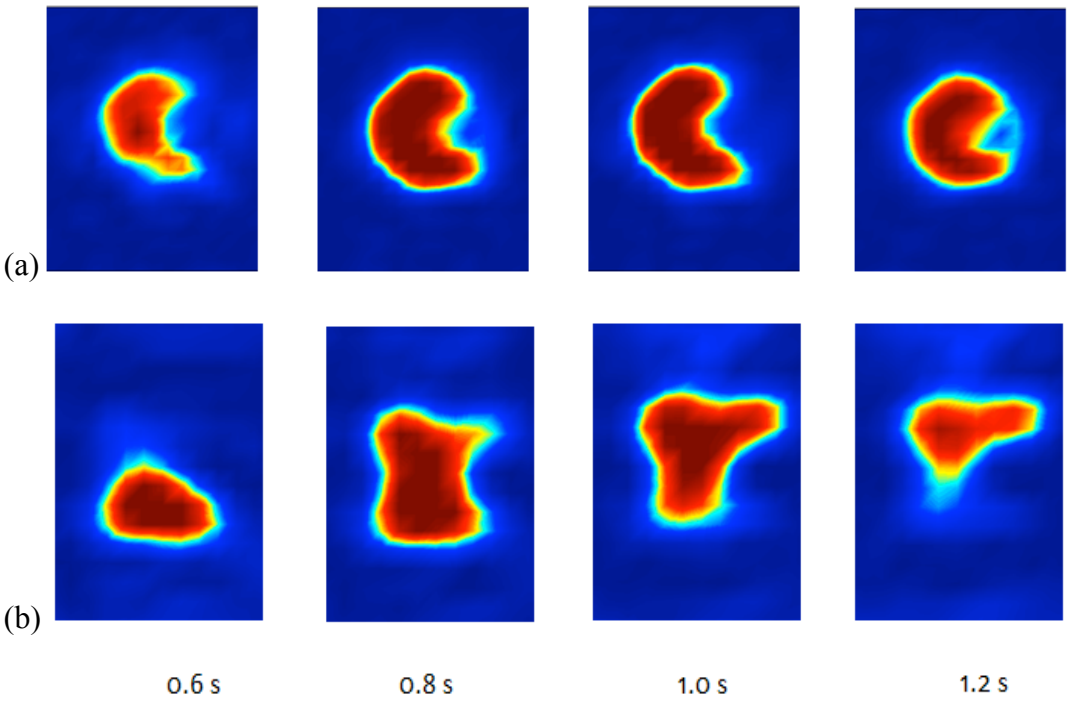

Figure 6.4 MR images along (a) *xy*- and (b) *xz*-planes of selectively polarized water in the sample holder with bypass channel with 100-μm porous steel sample.

The images along *xy*-plane in (a) original sample holder, (b) bypass holder and (c) bypass holder with 100-μm porous steel sample are shown in Figure 6.5. The disturbance regarding to the non-polarized water from the side is clearly seen in porous sample.

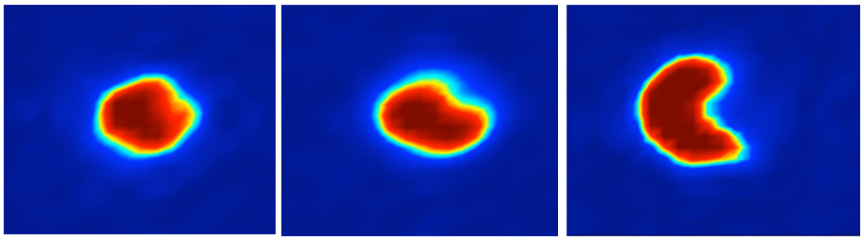

(a) **(b)** **(c)**

Figure 6.5 MR images of selectively polarized water along *xy*- plane in (a) original sample holder (b) bypass holder and (c) bypass holder with 100-μm porous steel sample.

6.1.3 Discussion

The images shown in Figure 6.3 and 6.4 reveal interesting flow behavior. The behaviors of flow mixing are different between with and without porous sample; selective mixing from one direction is achievable in a porous sample, for example, controlling the flow from the side channel in a desired position. However, orientation and position of mixing in blank holder is likely more spread out. If a chemical reaction is designed to occur in the porous sample under these experimental conditions, it will take place after 0.8 s and two flows come into contact, as clearly seen in Figure 6.4. In order to gain reasonable yield from mixing of some chemical or biological reactions with the current sample holder, the same flow conditions as in this experiment are required. Such information is essential to the design of microchannels, mixing and diffusing transport system or filtration membrane in which chemical reactions and biological processes occur.

6.2 Nuclear spin relaxation for different fluids in porous materials

To simulate the flow of mixtures in practical applications and to reveal the characteristics of the porous materials, different fluids were studied. Water and hexane have been selected, one is hydrophilic and the other hydrophobic. A series of porous steel samples are studied, with pore sizes of 0.2, 0.5, 1, 2, and 5 microns, respectively. At a continuous flow rate of 28 ml/min, the fluids were first polarized by

a 2-T permanent magnet, and then flew through the porous samples. A π pulse, with duration of 5 ms, is used to invert the spins in the sample region. The spin-tagged fluid then reached the atomic magnetometer for detection. The detection volume is 150 μl.

The flow profiles of water and hexane in a 0.5-micron porous steel sample are shown in Figure 6.6. The signal from hexane is lower than that of water despite the similar proton densities in the two compounds. No other significant differences in flow profiles were observed. Then in Table 6.2, the signal maxima of water and hexane are listed as a function of average pore size of the materials. It is interesting to note that the water magnetization varies significantly with the pore size, while the signal of hexanes varies little. This is most likely due to the fast proton exchange in water, which makes water protons sensitive to the environment. Conversely in hexane, proton exchange does not occur. Therefore, the nuclear relaxation is not affected much by the pore size of the material.

Table 6.2 Water and hexane signals vs. pore size.

Size (μm)	**Water M (pT)**	**Hexane M (pT)**
0	22.6	7.8
0.2	17.7	7.7
0.5	19.0	8.4
1	14.2	7.6
2	15.9	7.5
5	16.2	7.3

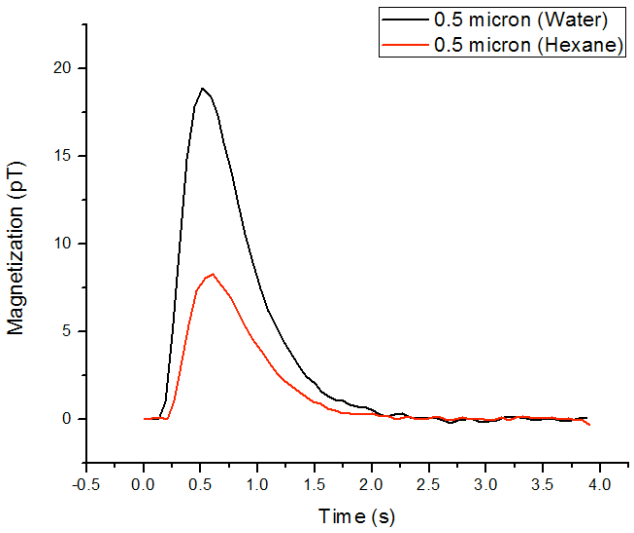

Figure 6.6 Flow profiles of water and hexane in a porous steel sample.

This result may lead to using hexane to explore the overall pore volume of porous materials due to the slight changes in nuclear relaxation. On the other hand, water can be used to probe the pore size and distribution, since the nuclear magnetization of water is sensitive to local environment.

Chapter 7

Conclusion

In this work, a compact and sensitive atomic magnetometer with sensitivity 150 fT/(Hz)$^{1/2}$ was used to study the magnetic resonance imaging (MRI) application by coupling with remote detection technique. This optically detected MRI is a useful tool for materials characterization. It is uniquely suitable for imaging through metals, a feature that optical and electronic microscopic techniques as well as conventional MRI cannot accomplish. Optically detected MRI compliments conventional techniques for analyzing porous materials, such as capillary flow porometry and liquid extrusion porosimetry. The spatially and temporally resolved flow information is essential for many applications of porous metals.

For enhanced sensitivity, a different configuration of magnetometer was designed and built. A divider was used to separate the sample region from the detection region. This arrangement increased the sensitivity by a factor of two, 80 fT/(Hz)$^{1/2}$, which was attributed to a decrease in noise caused by air flow. A zoom-in method was implemented to obtain high-resolution images for ultralow-field MRI.

The method overcomes the limitation on the gradient field imposed by the concomitant field effect and overcomes the heterogeneity of the ambient magnetic field. A sub-millimeter resolution of 0.6 mm × 0.6 mm has been achieved, demonstrated by the excellent resolution of two channels separated by a 0.6-mm gap. The spatial resolution is also facilitated with a gradient solenoid. The new geometry improved the filling factor for optical detection compared to a previous configuration. These results may pave the way for a wide range of applications for ultralow-field MRI.

The current instrument still has a large room for improvement. For example, the atomic sensors are made by glass blowing. A drawback of manufacturing cells in this fashion is probable imperfection of the glass surface, resulting in poor optical quality of the cells which distorts and scatters the laser beam. The sensitivity still needs to be improved. One way to improve is by setting up the multiple pass arrangement of beam. This will allow the beam to interact with Cs atoms longer therefore result in a higher optical rotation. Another development would be to minimize or eliminate the magnetic shield for more portable and accessible.

Appendix A

MATLAB codes

A1. Flow profiles

The average water signal was obtained using the following MATLAB script.

```
clear all
lock=importdata('pathfile');
M(:,1)=lock(:,1);   % Import Time, Diff Signal and Trigger.
M(:,2)=lock(:,4);
M(:,3)=lock(:,5);
prompt = {'Enter peak difference:'};
dlg_title = 'Input';
num_lines = 1;
def = {'6.30e-03'};   % Input peak difference of square waves.
answer2 = inputdlg(prompt,dlg_title,num_lines,def);
diff = str2num(answer2{1});
```

```
index = 0;   % Number of Triggers. (The first data point after the trigger)
index3 = 0;   % Number of Triggers - 1. (The last data point before the trigger)
size = 50;   % Number of points per flow profile.
X = zeros(5,1);  % For calculating standard deviation.
hu = [];
fu = [];
for n = 2:length(M)
   if (M(n,3)<3) && (M(n-1,3)>3)  % Find the first point of a given trigger.
      index = index+1;
      hu(1,index) = n;
   end
   if  n<length(M) && index>=1
      if (M(n,3)<3) && (M(n+1,3)>3)  % Find the last point of a given trigger.
         index3 = index3+1;
         fu(1,index3) = n;
      end
   end
   if index>0
      if  n>4
         for m = 1:5
            X(m) = M(n+m-5,2);
         end
      if  M(n,2)>mean(X)+3*std(X)
         M(n,2) = mean(X);
```

```
        else if M(n,2)<mean(X)-3*std(X)
            M(n,2) = mean(X);
            else M(n,2) = M(n,2);
            end
        end
        end
    end
end
for z = 1:index
    if  z<index
        rawdata1 = (M(hu(z):fu(z),1)-M(hu(z),1))';
        rawdata2 = ((M(hu(z):fu(z),2)-M(hu(z),2))*100/diff)';
    end
    if  z==index
        rawdata1 = (M(hu(z):(hu(z)+size),1)-M(hu(z),1))';
        rawdata2 = ((M(hu(z):(hu(z)+size),2)-M(hu(z),2))*100/diff)';
    end
    p = polyfit(rawdata1,rawdata2,16);
    xx = min(rawdata1):0.1:max(rawdata1);
    fit_x = xx(1:30);
    if z==1
        ha = zeros(index,length(fit_x));
    end
    fit_y = zeros(1,length(fit_x));
```

```
    for ii = 1:length(fit_x)
        fitting = [];
        for kk = 1:length(p)
            a = p(kk)*fit_x(ii).^( length(p)-kk);
            fitting = [fitting a];
        end
        fit_y(ii) = sum(fitting);
    end
    ha(z,:) = fit_y;
end
Z = mean(ha);
for m2 = 1:5
    Y(m2) = Z(length(fit_x)+m2-5);
end
for m = 1:length(Z);
    Z(m) = Z(m)-mean(Y)/fit_x(length(fit_x))*fit_x(m);
end
figure;
plot(fit_x,Z)
```

A2. 1D- and 2D-Imaging

Using the MATLAB script below, one-dimensional and two-dimensional images were obtained.

```
clear all
rawdata = importdata('pathfile');
M(:,1) = rawdata(:,1);
M(:,2) = rawdata(:,4);
M(:,3) = rawdata(:,5);
step_1D = 11; % 2D steps from pulse program.
step_2D = 11; % 3D steps from pulse program.
t_travel = 0.9; % Travel time.
size = 30; % Number of points per flow profile.
index = 0; % The first data point after the trigger.
step = step_1D*step_2D; % Number of steps for a single scan.
% Plot the 1D from 2D image
row = 13;
column = 11;
hu = [];
for n = 2:length(M)
   if (M(n,3)<3) && (M(n-1,3)>3)  % Find the first point of a given trigger.
      index = index+1;
      hu(1,index) = n;
   end
```

```
end
% Check for the missing data.
error = find(diff(hu)>79)+1;  % 79 is a threshold. It can be modified.
err2 = find(diff(hu)>79);
if isempty(error)==0
   time = M(:,1)';
   haha = (time(hu(error))+time(hu(err2)))/2;
   disp('Some data are missing. The positions are at')
   num2str(haha-0.1)
   break
end
data1 = [];
data2 = data1;
data3 = data1;
data4 = data1;
number = index;
dat1=[];
dat2=dat1;
dat3=dat1;
dat4=dat1;
tri_back=6;
for i = 1:1:index/step/4
    data1 = M(hu(1+(i-1)*4*step)-tri_back+1:hu(1+(i-1)*4*step+step)-tri_back,:);
    dat1 = [dat1; data1];
```

```
    data2 = M(hu(1+(i-1)*4*step+step)-tri_back+1:hu(1+(i-1)*4*step+2*step)-
tri_back,:);
    dat2 = [dat2; data2];
    data3 = M(hu(1+(i-1)*4*step+2*step)-tri_back+1:hu(1+(i-1)*4*step+3*step)-
tri_back,:);
    dat3 = [dat3; data3];
    if i == index/step/4
       data4 = M(hu(1+(i-1)*4*step+3*step)-tri_back+1:end,:);
       dat4 = [dat4; data4];
    else
       data4 = M(hu(1+(i-1)*4*step+3*step)-tri_back+1:hu(1+(i-1)*4*step+4*step)-
tri_back,:);
       dat4 = [dat4; data4];
    end
end
peakadd = zeros(step,4);
for r = 1:4;
    if r == 1
        lock = dat1;
    else if r == 2
            lock = dat2;
        else if r == 3
                lock = dat3;
            else
```

```
            lock = dat4;
        end
    end
end
N = [];
index = 0;
index2 = 0;
index3 = 0;
gu = [];
fu = [];
d = 0;
X = zeros(5,1);
peak = zeros(step,2); % Find the peak at the travel time and save for each step.
N(:,1) = lock(:,1);
N(:,2) = lock(:,2);
N(:,3) = lock(:,3);
for u = 2:length(N);
    if (N(u,3)<3)&&(N(u-1,3)>3)
        index = index+1;
        gu(1,index) = u;
    end
    if  u<length(N) && index>=1
        if (N(u,3)<3) && (N(u+1,3)>3)
            index3 = index3+1;
```

```
            fu(1,index3) = u;
        end
    end
    if index>0
      if u>4
        for m = 1:5
            X(m) = N(u+m-5,2);
        end
        if N(u,2)>mean(X)+3*std(X)
          N(u,2) = mean(X);
        else if N(u,2)<mean(X)-3*std(X)
              N(u,2) = mean(X);
            else
              N(u,2) = N(u,2);
            end
        end
      end
    end
end
for z = 1:index
    if  mod(z-1,step) == 0
        index2 = index2+1;
    end
    d = mod(z-1,step)+1;
```

```
if  z<index
   rawdata1 = (N(gu(z):fu(z),1)-N(gu(z),1))';
   rawdata2 = ((N(gu(z):fu(z),2)-N(gu(z),2))*2e4)';
end
if  z==index
   rawdata1 = (N(gu(z):(gu(z)+size),1)-N(gu(z),1))';
   rawdata2 = ((N(gu(z):(gu(z)+size),2)-N(gu(z),2))*2e4)';
end
p = polyfit(rawdata1,rawdata2,16);
xx = min(rawdata1):0.1:max(rawdata1);
fit_x = xx(1:30);
if z==1
   G = zeros(length(fit_x),2,step);
end
fit_y = zeros(length(fit_x),1);
for ii = 1:length(fit_x)
   fitting = [];
   for kk = 1:length(p)
      a = p(kk)*fit_x(ii).^( length(p)-kk);
      fitting = [fitting a];
   end
   fit_y(ii) = sum(fitting);
   if index2 == 1
      G(ii,1,d) = fit_x(ii);
```

```
            end
            G(ii,2,d) = G(ii,2,d) + fit_y(ii);
        end
    end
    if index2>0
        for d = 1:step
            peak(d,1) = d;
            % Baseline editing.
            b02 = (G(length(fit_x)-1,2,d)+G(length(fit_x)-2,2,d)+G(length(fit_x)-
3,2,d)+G(length(fit_x)-4,2,d)+G(length(fit_x),2,d))/5;
            for ii = 1:length(fit_x)
                G(ii,2,d)    =    (G(ii,2,d)-G(ii,1,d)*(b02)/G(length(fit_x),1,d))/index2;    %
Calibration and linear correction.
                if (ii>5)&&(G(ii,1,d)>=t_travel)&&(G(ii-1,1,d)<t_travel) % To avoid the
first point.
                    peak(d,2) = G(ii,2,d)+(G(ii,2,d)-G(ii-1,2,d))*(t_travel-
G(ii,1,d))/(G(ii,1,d)-G(ii-1,1,d));
                    peak_position = ii;
                end
            end
        end
    end
    peakadd(:,r) = peak(:,2);
end
```

```
a1 = peakadd(:,1); a2 = peakadd(:,2); a3 = peakadd(:,3); a4 = peakadd(:,4);
real = (a1-a2)/2; imag = (a3-a4)/2;
total = real+sqrt(-1)*imag;
total = reshape(total,step_1D,step_2D);
b = fftshift(fftshift(fft(fft(total,2*step_1D,1),2*step_2D,2),1),2);
figure; pcolor(abs(b));
shading interp;
set(gcf,'Renderer','painters');
% Plot figure
figure(1);
set(gca,'fontsize',24)
pcolor(abs(b));
xlabel('Pixel')
ylabel('Pixel')
shading interp;
set(gcf,'Renderer','painters');
figure(2);
hold on
set(gca,'fontsize',24)
plot(aaa(row,:),'b','linewidth',3);
xlabel('Pixel (y-axis)')
ylabel('Intensity')
figure(3);
hold on
```

```
set(gca,'fontsize',24)
plot(aaa(:,column),'b','linewidth',3);
xlabel('Pixel (x-axis)')
ylabel('Intensity')
```

A3. 2D-Movies

Using the MATLAB script below, two-dimensional movies were obtained.

```
clear all;
tic
period = 0.01;
time_ini = 0;
time_final = 3;
t_travel = time_ini:period:time_final;
step_1D = 9;
step_2D = 11;
step = step_1D*step_2D;
size_temp = 30;  % Number of points per flow profile.
% Loop of data
filename = 'lock001';
workpath = 'data';
setenv('DYLD_LIBRARY_PATH', '/usr/local/bin/');
output_folder = ['./',workpath]; % All the data files generated will be stored in this folder.
path_data = strcat(output_folder,['/',filename]);
```

```
% Output pathnames
path_output = strcat(output_folder);
% Save result
out_filename = 'data_2D.mat';
out_path_data = strcat(output_folder,['/',out_filename]);
% Load data
rawdata = importdata(path_data);
M(:,1) = rawdata(:,1);
M(:,2) = rawdata(:,4);
M(:,3) = rawdata(:,5);
clear rawdata
trigger_threshold = 3;
hu = [];
for n = 2:length(M);
    if (M(n,3)<trigger_threshold)&&(M(n-1,3)>trigger_threshold)
        hu = [hu n];
    end
end
% Check the missing data
error = find(diff(hu)>79)+1;  % 79 is a threshold. It can be modified.
error2 = find(diff(hu)>79)+1;
if isempty(error)==0
   time = M(:,1)';
   haha = (time(hu(error))+time(hu(error2)))/2;
```

```
   disp('Some data are missing. The positions are at')
   num2str(haha-0.1)
   break
end
% Data analysis
tri_back = 6;
aaa_time = [];
peakadd = MRI_analyze(hu,M,step,size_temp,t_travel,tri_back);
a1 = peakadd(:,1);
a2 = peakadd(:,2);
a3 = peakadd(:,3);
a4 = peakadd(:,4);
real_temp = (a1-a2)/2;
imag_temp = (a3-a4)/2;
total = real_temp + 1i*imag_temp;
for mm = 1:length(t_travel)
    total_temp = total((mm-1)*step+1:mm*step);
    total_temp = reshape(total_temp,step_1D,step_2D);
    b = fftshift(fftshift(fft(fft(total_temp,2*step_1D,1),2*step_2D,2),1),2);
    aaa_time(:,:,mm) = abs(b);
    save(out_path_data,'aaa_time')
end
toc
% Plot figure (time flow)
```

```
figure(1);
set(gca,'fontsize',24)
xlabel('Pixel')
ylabel('Pixel')
for kk = 1:length(t_travel)
  pcolor(aaa_time(:,:,kk));
  caxis([min(min(min(aaa_time))) max(max(max(aaa_time)))])
  shading interp;
  set(gcf,'Renderer','painters');
  pause(0.1)
end

function peakadd = MRI_analyze(hu,M,step,size_temp,t_travel,tri_back)
index = length(hu); % This is the amounts of trigger.
dat1 = []; % phase x
dat2 = []; % phase -x
dat3 = []; % phase y
dat4 = []; % phase -y
for ii = 1:index/step/4   % The "4" means four phases.
   % Phase x
   data1 = M(hu(1+(ii-1)*4*step)-tri_back+1:hu(1+(ii-1)*4*step+step)-tri_back,:);
   dat1 = [dat1; data1];
   % Phase -x
```

```
    data2 = M(hu(1+(ii-1)*4*step+step)-tri_back+1:hu(1+(ii-1)*4*step+2*step)-
tri_back,:);
    dat2 = [dat2; data2];
    % Phase y
    data3 = M(hu(1+(ii-1)*4*step+2*step)-tri_back+1:hu(1+(ii-1)*4*step+3*step)-
tri_back,:);
    dat3 = [dat3; data3];
    % Phase -y
    if ii == index/step/4
      data4 = M(hu(1+(ii-1)*4*step+3*step)-tri_back+1:end,:);
      dat4 = [dat4; data4];
    else
      data4 = M(hu(1+(ii-1)*4*step+3*step)-tri_back+1:hu(1+(ii-1)*4*step+4*step)-
tri_back,:);
      dat4 = [dat4; data4];
    end
end
peakadd = zeros(step,4);
for r = 1:4;
    if r == 1
       lock = dat1;
    else if r == 2
          lock = dat2;
        else if r == 3
```

```
            lock = dat3;
        else
            lock = dat4;
        end
    end
end
N = [];
index = 0;
index2 = 0;
index3 = 0;
gu = [];
fu = [];
d = 0;
X = zeros(5,1);
peak = zeros(step,2);
N(:,1) = lock(:,1);
N(:,2) = lock(:,2);
N(:,3) = lock(:,3);
for u = 2:length(N);
    if (N(u,3)<3)&&(N(u-1,3)>3)
        index = index+1;
        gu(1,index) = u;
    end
    if  u<length(N) && index>=1
```

```
        if (N(u,3)<3) && (N(u+1,3)>3)
            index3 = index3+1;
            fu(1,index3) = u;
        end
    end
    if index>0
      if u>4
        for m = 1:5
            X(m) = N(u+m-5,2);
        end
        temp_3_std = 3*std(X);
        mean_X = mean(X);
        if N(u,2)>mean_X + temp_3_std
          N(u,2) = mean_X;
        else if N(u,2)<mean_X - temp_3_std
              N(u,2) = mean_X;
            else
              N(u,2) = N(u,2);
            end
        end
      end
    end
end
for z = 1:index
```

```
if  mod(z-1,step) == 0
   index2 = index2+1;
end
d = mod(z-1,step)+1;
if  z<index
   rawdata1 = (N(gu(z):fu(z),1)-N(gu(z),1))';
   rawdata2 = ((N(gu(z):fu(z),2)-N(gu(z),2))*2e4)';
end
if  z==index
   rawdata1 = (N(gu(z):(gu(z)+size_temp),1)-N(gu(z),1))';
   rawdata2 = ((N(gu(z):(gu(z)+size_temp),2)-N(gu(z),2))*2e4)';
end
p = polyfit(rawdata1,rawdata2,16);
fit_x = min(rawdata1):0.1:min(rawdata1)+2.9;
if z==1
   G = zeros(length(fit_x),2,step);
end
fit_y = zeros(length(fit_x),1);
for ii = 1:length(fit_x)
   fit_y(ii) = polyvalm(p,fit_x(ii));
   if index2 == 1
      G(ii,1,d) = fit_x(ii);
   end
   G(ii,2,d) = G(ii,2,d) + fit_y(ii);
```

```
    end
  end
  % Correction of baseline
  if index2>0
    for d = 1:step
      peak(d,1) = d;
      % Baseline editing.
      b02 = (G(length(fit_x)-1,2,d) + G(length(fit_x)-2,2,d) +...   % Smoothing (moving average)
          G(length(fit_x)-3,2,d) + G(length(fit_x)-4,2,d) +...
          G(length(fit_x),2,d))/5;
      for ii = 1:length(fit_x)
        G(ii,2,d) = (G(ii,2,d)-G(ii,1,d)*(b02)/G(length(fit_x),1,d))/index2;   % Calibration and linear correction.
          if (ii>5)&&(G(ii,1,d)>=t_travel)&&(G(ii-1,1,d)<t_travel) % To avoid the first point.
            peak(d,2) = G(ii,2,d)+(G(ii,2,d)-G(ii-1,2,d))*(t_travel-G(ii,1,d))/(G(ii,1,d)-G(ii-1,1,d));
          end
      end
    end
  end
  peakadd(:,r) = peak(:,2);
end
```

A4. Off-axis magnetic field (parallel)

An off-axis magnetic field mapping (a parallel plane) of a current loop was obtained using the following MATLAB script.

```
clear all
% For a parallel plane
xx = linspace(0.054,0.094,200);
yy = linspace(-0.02,0.02,200);
distance_ring = [0.005 0.008 0.012 0.015 0.0175 0.02 0.022 0.024 0.0265 0.0285 0.031 0.034 0.038 0.04 0.042 0.045 0.047 0.05 0.053]; % The distances from the Cs atomic vapor cell to each turn of copper wire wound around the gradient solenoid.
distance_x = [0 distance_ring];
current_I = 0.144; % amperes
temp_x = zeros(length(yy),length(xx));
temp_y = zeros(length(yy),length(xx));
for ii = 1:length(distance_x)
   [temp_Bx temp_By] = fun_SR_1(xx+distance_x(ii),current_I,abs(yy)');
   temp_Bx(isnan(temp_Bx)) = 0;
   temp_Bx(isinf(temp_Bx)) = 0;
   temp_By(isnan(temp_By)) = 0;
   temp_By(isinf(temp_By)) = 0;
   temp_x = temp_x + temp_Bx;
   temp_y = temp_y + temp_By;
end
```

```
C = sqrt(temp_x.^2+temp_y.^2);
B = C/1e-9;
% Plot figure
figure;
set(gca,'fontsize',18)
pcolor(xx,yy,B);
shading interp;


function [Bx Br] = fun_SR_1(x,I0,r)
a = 0.004; % Unit is in meter.
uo = 1.26e-6;   %uo = permeability constant
B0 = I0*uo/(2*a);  %Bo = magnetic field at the center of the coil
L = r/a;
B = x/a;
G = repmat(x,length(r),1)./repmat(r,1,length(x));
Q = bsxfun(@plus,(1+L).^2,B.^2);
k = (4*repmat(L,1,length(x))./Q).^0.5;
m = k.^2;
 [K E] = ellipke(m); %returns the complete elliptic integral of the first and second
kinds.
Bx = B0*1./(pi*Q.^0.5).*(E.*(bsxfun(@minus,1-L.^2,B.^2))./(Q-
4*repmat(L,1,length(x)))+K);
Br = B0.*G./(pi*Q.^0.5).*(E.*(bsxfun(@plus,1+L.^2,B.^2))./(Q-
4*repmat(L,1,length(x)))-K);
```

A5. Off-axis magnetic field (perpendicular)

An off-axis magnetic field mapping (a perpendicular plane) of a current loop was obtained using the following MATLAB script.

```
clear all
% For a perpendicular plane
xx = linspace(-0.09,0.09,200);
yy = linspace(-0.09,0.09,200);
r = sqrt(bsxfun(@plus,xx'.^2,yy.^2));
x = 0.094;
distance_ring = [0.005 0.008 0.012 0.015 0.0175 0.02 0.022 0.024 0.0265 0.0285 0.031 0.034 0.038 0.04 0.042 0.045 0.047 0.05 0.053]; % The distances from the Cs atomic vapor cell to each turn of copper wire wound around the gradient solenoid.
distance_x = x + [0 distance_ring];
current_I = 0.144; % amperes
temp_x = zeros(size(r));
temp_y = zeros(size(r));
for ii = 1:length(distance_x)
   [temp_Bx temp_By] = fun_SR(distance_x(ii),current_I,r);
   temp_Bx(isnan(temp_Bx)) = 0;
   temp_By(isnan(temp_By)) = 0;
   temp_x = temp_x + temp_Bx;
   temp_y = temp_y + temp_By;
end
```

```
C = sqrt(temp_x.^2+temp_y.^2);

B = C/1e-9;

% Plot figure

figure;

set(gca,'fontsize',18)

pcolor(xx,yy,B);

shading interp;


function [Bx Br] = fun_SR(x,I0,r)

a = 0.004; % Unit is in meter.

uo = 1.26e-6;   %uo = permeability constant

B0 = I0*uo/(2*a);  %Bo = magnetic field at the center of the coil

L = r/a;

B = x/a;

G = x./r;

Q = (1+L).^2 + B.^2;

k = (4*L./Q).^0.5;

m = k.^2;

 [K E] = ellipke(m); %returns the complete elliptic integral of the first and second kinds.

Bx = B0*1./(pi*Q.^0.5).*(E.*(1-L.^2-B.^2)./(Q-4*L)+K);

Br = B0.*G./(pi*Q.^0.5).*(E.*(1+L.^2+B.^2)./(Q-4*L)-K);
```

Appendix B

Off-axis field of a current loop

A magnetic field at any point in space can be estimated by using the simple formula obtaining from the law of Biot Savart, integrated over a circular current loop.

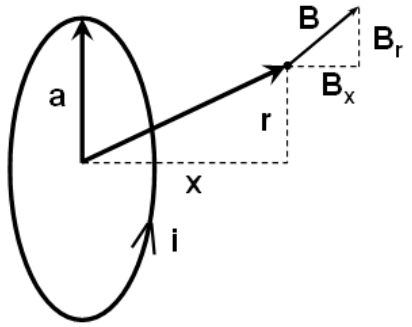

B is the magnetic field, in teslas, at any point in space that is not on the current loop. It is equal to the sum of two field components: $\mathbf{B_x}$ and $\mathbf{B_r}$.

$$B_x = B_0 \frac{1}{\pi\sqrt{Q}} \left[E(k) \frac{1-\alpha^2-\beta^2}{Q-4\alpha} + K(k) \right]$$

$$B_r = B_0 \frac{\gamma}{\pi\sqrt{Q}} \left[E(k) \frac{1+\alpha^2+\beta^2}{Q-4\alpha} - K(k) \right]$$

B_x is the magnetic field component that is aligned with the coil axis and

B_r is the magnetic field component that is in a radial direction.

i is the current in the wire, in amperes.

a is the radius of the current loop.

x is the distance, on axis, from the center of the current loop to the field measurement point.

r is the radial distance from the axis of the current loop to the field measurement point.

$$\alpha = \frac{r}{a} \quad , \quad \beta = \frac{x}{a} \quad , \quad \gamma = \frac{x}{r}$$

$$Q = \left[(1+\alpha)^2 + \beta^2\right]$$

$$k = \sqrt{\frac{4\alpha}{Q}}$$

K(k) is the complete elliptic integral function of the first kind.

E(k) is the complete elliptic integral function of the second kind.

Note that the argument to K and E is shown here as the modulus "k". Other valid argument is the parameter "m" (where $m = k^2$).

B_o is the magnetic field at the center of the coil ($i\mu_o/2a$)

μ_o is the permeability constant (1.26×10^{-6} H/m or $4\pi \times 10^{-7}$).

Bibliography

[1] G.J. Bene, Nuclear magnetism of liquid system in the Earth field range, Phys. Rep. 58 (1980) 213–267.

[2] J. Stepisnik, M. Kos, G. Planinsic, V. Erzen, Strong non-uniform magnetic field for self-diffusion measurement by NMR in the earth's magnetic field, J. Magn. Reson. A 107 (1994) 167–172.

[3] S. Appelt, F.W. Hasing, H. Kuhn, J. Perlo, B. Blumich, Mobile high resolution xenon nuclear magnetic resonance spectroscopy in the earth's magnetic field, Phys. Rev. Lett. 94 (2005) 197602.

[4] M. Packard, R. Varian, Free nuclear induction in the Earth's magnetic field, Phys. Rev. 93 (1954) 941.

[5] A.G. Goloshevsky, J.H. Walton, M.V. Shutov, J.S. de Ropp, S.D. Collins, M. J. McCarthy, Development of low field nuclear magnetic resonance microcoils, Rev. Sci. Instrum. 76 (2005) 024101.

[6] S. Appelt, H. Kuhn, F.W. Hasing, B. Blumich, Chemical analysis by ultrahigh-resolution nuclear magnetic resonance in the Earth's magnetic field Nat. Phys. 2 (2006) 105-109.

[7] J.N. Robinson, A. Coy, R. Dykstra, C.D. Eccles, M.W. Hunter, P.T. Callaghan, Two-dimensional NMR spectroscopy in Earth's magnetic field, J. Magn. Reson. 182 (2006) 343–347.

[8] A. Mohoric, G. Planinsic, M. Kos, A. Duh, J. Stepisnik, Magnetic resonance imaging system based on Earth's magnetic field, Instrum. Sci. Technol. 32 (2004) 655–667.

[9] M.E. Halse, A. Coy, R. Dykstra, C. Eccles, M. Hunter, R. Ward, P.T. Callaghan, A practical and flexible implementation of 3D MRI in the Earth's magnetic field, J. Magn. Reson. 182 (2006) 75–83.

[10] S.K. Lee, M. Möble, W.R. Myers, N. Kelso, A.H. Trabesinger, A. Pines, J. Clarke, SQUID-detected MRI at 132 μT with T_1-weighed contrast established at 10 μT- 300 mT, Magn. Reson. Med. 53 (2005) 9–14.

[11] V.S. Zotev, T. Owens, A.N. Matlashov, I.M. Savukov, J.J. Gomez, M.A. Espy, Microtesla MRI with dynamic nuclear polarization, J. Magn. Reson. 207 (2010) 78–88.

[12] J. Dabek, P.T. Vesanen, K.C.J. Zevenhoven, J.O. Nieminen, R. Sepponen, R.J. Ilmoniemi, SQUID-sensor-based ultra-low-field MRI calibration with phantom images: towards quantitative imaging, J. Magn. Reson. 224 (2012) 22–31.

[13] J. Hatta, M. Miyamoto, Y. Adachi, J. Kawai, G. Uehara, SQUID-based low field MRI system for small animals, IEEE Trans. Appl. Supercond. 21 (2011) 526–529.

[14] H.-H. Chen, H.-C. Yang, H.-E. Horng, S.H. Liao, S.-Y. Yang, K.L. Chen, L.W. Wang, M.J. Chen, Magnetic resonance imaging of hyperpolarized ^{3}He

detected with a high-Tc SQUID in microtesla magnetic field at laboratory environment fields, IEEE Trans. Appl. Supercond. 21 (2011) 505–508.

[15] R. McDermott, A.H. Trabesinger, M. Muck, E.L. Hahn, A. Pines, J. Clarke, Liquid-state NMR and scalar couplings in microtesla magnetic fields, Science 295 (2002) 2247-2249.

[16] R. McDermott, S-K. Lee, B. Haken, A.H. Trabesinger, A. Pines, J. Clarke, Microtesla MRI with a superconducting quantum interference device, Proc. Natl. Acad. Sci. USA. 101 (2004) 7857-7861.

[17] V.S. Zotev, A.N. Matlashov, P.L. Volegov, I.M. Savukov, M.A. Espy, J.C. Mosher, J.J. Gomez, R.H. Kraus Jr, Microtesla MRI of the human brain combined with MEG, J. Mag. Resn. 194 (2008) 115-120.

[18] F. Verpillat, M.P. Ledbetter, S. Xu, D.J. Michalak, C. Hilty, L.S. Bouchard, S. Antonijevic, D. Budker, A. Pines, Remote detection of nuclear magnetic resonance with an anisotropic magnetoresistive sensor, Proc. Natl. Acad. Sci. USA 105 (2008) 2271-2273.

[19] M. Pannetier, C. Fermon, G. Le Goff, J. Simola, E. Kerr, Femtotesla magnetic field measurement with magnetoresistive sensors, Science 304 (2004) 1648-1650.

[20] J.R. Maze, P.L. Stanwix, J.S. Hodges, S. Hong, J.M. Taylor, P. Cappellaro, L. Jiang, M.V. Gurudev Dutt, E. Togan, A.S. Zibrov, A. Yacoby, R.L. Walsworth, M.D. Lukin, Nanoscale magnetic sensing with an individual electronic spin in diamond, Nature 455 (2008) 644-647.

[21] G. Balasubramanian, I. Y. Chan, R. Kolesov, M. Al-Hmoud, J. Tisler, C. Shin, C. Kim, A. Wojcik, P.R. Hemmer, A. Krueger, T. Hanke, A. Leitenstorfer, R.

Bratschitsch, F. Jelezko1, J. Wrachtrup, Nanoscale imaging magnetometry with diamond spins under ambient conditions, Nature 455 (2008) 648-651.

[22] H.J. Mamin, M. Kim, M.H. Sherwood, C.T. Rettner, K. Ohno, D.D. Awschalom, D. Rugar, Nanoscale Nuclear Magnetic Resonance with a Nitrogen-Vacancy Spin Sensor, 339 (2013) 557-560.

[23] H.G. Dehmelt, Modulation of a light beam by precessing absorbing atoms, Phys. Rev. 105 (1957) 1924–1925.

[24] J. Dupont-Roc, S. Haroche, C. Cohen-Tannoudji, Detection of very weak magnetic fields (10^{-9} gauss) by ^{87}Rb zero-field level crossing resonances, Phys. Lett. A 28 (1969) 638–639.

[25] D. Budker, D.F. Kimball, S.M. Rochester, V.V. Yashchuk, M. Zolotorev, Sensitive magnetometry based on nonlinear magneto-optical rotation, Phys. Rev. A 62 (2000) 043403.

[26] I.K. Kominis, T.W. Kornack, J.C. Allred, M.V. Romalis, A subfemtotesla multichannel atomic magnetometer, Nature 422 (2003) 596–599.

[27] V. Shah, S. Knappe, P.D.D. Schwindt, J. Kitching, Subpicotesla atomic magnetometer with a microfabricated vapour cell, Nat. Photon. 1 (2007) 649–652.

[28] H.B. Dang, A.C. Maloof, M.V. Romalis, Ultrahigh sensitivity magnetic field and magnetization measurements with an atomic magnetometer, Appl. Phys. Lett. 97 (2010) 151110.

[29] S.-J. Xu, V.V. Yashchuk, M.H. Donaldson, S.M. Rochester, D. Budker, A. Pines, Magnetic resonance imaging with an optical atomic magnetometer, Proc. Natl. Acad. Sci. USA. 103 (2006) 12668–12671.

[30] I.M. Savukov, V.S. Zotev, P.L. Volegov, M.A. Espy, J.J. Gomez, R.H. Kraus, MRI with an atomic magnetometer suitable for practical imaging applications, J. Magn. Reson. 199 (2009) 188–191.

[31] M.P. Ledbetter, C.W. Crawford, A. Pines, D.E. Wemmer, S. Knappe, J. Kitching, D. Budker, Optical detection of NMR J-spectra at zero magnetic field, J. Magn. Reson. 199 (2009) 25–29.

[32] M.P. Ledbetter, T. Theis, J.W. Blanchard, H. Ring, P. Ganssle, S. Appelt, B. Blumich, A. Pines, D. Budker, Near-zero-field nuclear magnetic resonance, Phys. Rev. Lett. 107 (2011) 107601.

[33] V.V. Yashchuk, J. Granwehr, D.F. Kimball, S.M. Rochester, A.H. Trabesinger, J.T. Urban, D. Budker, and A. Pines, Hyperpolarized Xenon Nuclear Spins Detected by Optical Atomic Magnetometry, Phys. Rev. Lett. 93 (2004) 160801.

[34] I.M. Savukov and M.V. Romalis, NMR Detection with an Atomic Magnetometer, Phys. Rev. Lett. 94 (2005) 123001.

[35] S.-K. Lee, K.L. Sauer, S.J. Seltzer, O. Alem, M.V. Romalis, Subfemtotesla radiofrequency atomic magnetometer for detection of nuclear quadrupole resonance, Appl. Phys. Lett. 89 (2006) 214106.

[36] H. Xia, A.B.-A. Barabga, D. Hoffman, M.V. Romalis, Magnetoencephalography with an atomic magnetometer, Appl. Phys. Lett. 89 (2006) 211104.

[37] T. H. Sander, J. Preusser, R. Mhaskar, J. Kitching, L. Trahms, and S. Knappe, Magnetoencephalography with a chip-scale atomic magnetometer, Biomedical Optics Express, 3 (2012) 981-990.

[38] A. Weis, R. Wynands, R. Fenici, G. Bison, Dynamical MCG mapping with an atomic vapor magnetometer, Neurol. Clin. Neurophysiol. 38 (2004) 1–5.

[39] G. Bison, R. Wynands, and A. Weis, A laser-pumped magnetometer for the mapping of human cardio magnetic fields, Appl. Phys. B 76 (2003) 325–328.

[40] J. Belfi, G. Bevilacqua, V. Biancalana, S. Cartaleva, Y. Dancheva, L. Moi, Cesium coherent population trapping magnetometer for cardio signal detection in an unshielded environment, J. Opt Soc of America B 24 (2007) 2357–2362.

[41] L. Yao, S.-J. Xu, Long-range, high-resolution magnetic imaging of nanoparticles, Angew. Chem., Int. Ed. 48 (2009) 5679–5682.

[42] L. Yao, A.C. Jamison, S.-J. Xu, Scanning imaging of magnetic nanoparticles for quantitative molecular imaging, Angew. Chem., Int. Ed. 49 (2010) 7493–7496.

[43] L. Yao, S.-J. Xu, Force-induced remnant magnetization spectroscopy for specific magnetic imaging of molecules, Angew. Chem., Int. Ed. 50 (2011) 4407–4409.

[44] I.M. Savukov, S.J. Seltzer, M.V. Romalis, K.L. Sauer, Tunable Atomic Magnetometer for Detection of Radio-Frequency Magnetic Fields, Phys. Rev. Lett. 95 (2005) 063004.

[45] D. Budker, M.V. Romalis, Optical magnetometry, Nat. Phys. 3 (2007) 227-234.

[46] D. Budker, W. Gawlik, D.F. Kimball, S.M. Rochester, V.V. Yashchuk, A. Weis, Resonant nonlinear magneto-optical effects in atoms, Rev. Mod. Phys. 74 (2002) 1153-1202.

[47] D. Macaluso, O.M. Corbino, C.R. Hebd. Seances Acad. Sci. 127 (1898) 548-550.

[48] J. Brossel, A. Kastler, Compt. Rend. 229 (1949) 1213–1215.

[49] W. Happer, Optical Pumping, Rev. Mod. Phys. 44 (1972) 169–249.

[50] J.C. Allred, R.N. Lyman, T.W. Kornack, M.V. Romalis, High-sensitivity atomic magnetometer unaffected by spin-exchange relaxation, Phys. Rev. Lett. 89 (2002) 130801.

[51] D. Budker, D.F. Kimball, V.V. Yashchuk, M. Zolotorev, Nonlinear magneto-optical rotation with frequency-modulated light, Phys. Rev. A. 65 (2002) 055403.

[52] W. Gawlik, L. Krzemien, S. Pustelny, D. Sangla, J. Zachorowski, M. Graf, A.O. Sushkov, D. Budker, Nonlinear magneto-optical rotation with amplitude modulated light, Appl. Phys. Lett. 88 (2006) 131108.

[53] M.T. Graf, D.F. Kimball, S.M. Rochester, K. Kerner, C. Wong, D. Budker, E.B. Alexandrov, M.V. Balabas, and V.V. Yashchuk, Relaxation of atomic polarization in paraffin-coated cesium vapor cells, Phys. Rev. A 72 (2005) 023401.

[54] S.J. Seltzer, P.J. Meares, M.V. Romalis, Synchronous optical pumping of quantum revival beats for atomic magnetometry, Phys. Rev. A 75 (2007) 051407.

[55] M.V. Balabas, T. Karaulanov, M.P. Ledbetter, D. Budker, Polarized Alkali-Metal Vapor with Minute-Long Transverse Spin-Relaxation Time, Phys. Rev. Lett. 105 (2010) 070801.

[56] E.P. Corsini, T. Karaulanov, M. Balabas, D. Budker, Hyperfine frequency shift and Zeeman relaxation in alkali-metal-vapor cells with antirelaxation alkene coating, Phys. Rev. A 87 (2013) 022901.

[57] W. Happer, H. Tang, Spin-exchange shift and narrowing of magnetic resonance lines in optically pumped alkali vapors, Phys. Rev. Lett. 31 (1973) 273-276.

[58] D. Budker, V. Yashchuk, M. Zolotorev, Nonlinear magneto-optic effects with ultra-narrow widths. Phys. Rev. Lett. 81 (1998) 5788-5791.

[59] N.C. Garcia, D. Yu, L. Yao, S.-J. Xu, Optical atomic magnetometer at body temperature for magnetic particle imaging and nuclear magnetic resonance, Opt. Lett. 35 (2010) 661-663.

[60] D. Yu, S. Ruangchaithaweesuk, L. Yao, S.-J. Xu, Detecting molecules and cells labeled with magnetic particles using an atomic magnetometer, J. Nanopart. Res. 14 (2012) 1135.

[61] S.-J. Xu, S.M. Rochester, V.V. Yashchuk, M.H. Donaldson, D. Budker, Construction and applications of an atomic magnetic gradiometer based on nonlinear magneto-optical rotation, Rev. Sci. Instr. 77 (2006) 083106.

[62] S.-J. Xu., V.V. Yashchuk, M.H. Donaldson, S.M. Rochester, D. Budker, A. Pines, Magnetic resonance imaging with an optical atomic magnetometer, Proc. Natl. Acad. Sci. USA 103 (2006) 12668-12671.

[63] K.L. Corwin, Z-T. Lu, C.F. Hand, R.J. Epstein, C.E. Wieman, Frequency-stabilized diode laser with the Zeeman shift in an atomic vapor, Appl. Opt. 37 (1998) 3295-3298.

[64] V.V. Yashchuk, D. Budker, J.R. Davis, Laser frequency stabilization using linear magneto-optics, Rev. Sci. Instr. 71 (2000) 341-346.

[65] S.J. Seltzer. Developments in alkali-metal atomic magnetometry, PhD Dissertation, Princeton University, November 2008.

[66] D. Maser, S. Pandey, H. Ring, M.P. Ledbetter, S. Knappe, J. Kitching, D. Budker, Detection of a single cobalt microparticle with a microfabricated atomic magnetometer, Rev. Sci. Instrum. 82 (2011) 086112.

[67] A.J. Moule´, M.M. Spence, S-I. Han, J.A. Seeley, K.L. Pierce, S. Saxena, A. Pines, Amplification of xenon NMR and MRI by remote detection, Proc. Natl. Acad. Sci. USA 100 (2003) 9122–9127.

[68] T.G. Walker, W. Happer, Spin-exchange optical pumping of noble gas nuclei, Rev. Mod. Phys. 69 (1997) 629.

[69] E. Harel, J. Granwehr, J.A. Seeley, A. Pines, Multiphase imaging of gas flow in a nanoporous material using remote-detection NMR, Nat. Mater. 5 (2006) 321–327.

[70] C. Hilty, E.E. McDonnell, J. Granwehr, K.L. Pierce, S.I. Han, A. Pines, Microfluidic gas-flow profiling using remote-detection NMR, Proc. Natl. Acad. Sci. USA 102 (2005) 14960–14963.

[71] H.A. Stone, A.D. Stroock, A. Ajdari, Engineering flows in small devices: microfluidics toward a lab-on-a-chip, Annu. Rev. Fluid Mech. 36 (2004) 381–411.

[72] E. Harel, C. Hilty, K. Koen, E.E. McDonnell, A. Pines, Time-of-flight flow imaging of two-component flow inside a microfluidic chip, Phys. Rev. Lett. 98 (2007) 017601.

[73] I.M. Savukov, S.J. Seltzer, M.V. Romalis, Detection of NMR signals with a radio-frequency atomic magnetometer, J. Magn. Reson. 185 (2007) 227–233.

[74] J. Mispelter, M. Lupu, A. Briguet, NMR probeheads for biophysical and biomedical experiments: theoretical principles & practical guidelines, Imperial College, London, UK, **2006**.

[75] R. Turner, Gradient coil design: a review of methods, Magn. Reson. Imag. 11 (1993) 903-920.

[76] S.-J. Xu, E. Harel, D.J. Michalak, C.W. Crawford, D. Budker, A. Pines, Flow in porous metallic materials: a magnetic resonance imaging study, J. Magn. Reson. Imag. 28 (2008) 1299-1302.

[77] L.-P. Lefebvre, J. Banhart, D.C. Dunand, Porous metals and metallic foams: current status and recent developments, Adv. Eng. Mater. 10 (2008) 775–787.

[78] H. Nakajima, Fabrication, properties and application of porous metals with directional pores, Prog. Mater. Sci. 52 (2007) 1091–1173.

[79] J. Banhart, Manufacture, characterization and application of cellular metals and metal foams, Prog. Mater. Sci. 46 (2001). 559-632.

[80] P. Cognet, J. Berlan, G. Lacoste, P.L. Fabre, J.M. Jud, Application of metallic foams in an electrochemical pulsed flow reactor Part II: Oxidation of benzyl alcohol, J. Appl. Electrochem. 26 (1996) 631–637.

[81] T. Kokubo, S. Yamaguchi, Bioactive Ti metal and its alloys prepared by chemical treatments: state-of-the-art and future trends, Adv. Eng. Mater. 12 (2010) B579–B591.

[82] L.P. Lefebvre, J. Banhart, D. Dunand, Porous Metals and Metallic Foams: Current Status and Recent Developments, Adv. Eng. Mater. 10 (2008) 775-787.

[83] T.R. Bryar, C.J. Daughney, R.J. Knight, Paramagnetic Effects of Iron(III) Species on Nuclear Magnetic Relaxation of Fluid Protons in Porous Media, J. Magn. Reson. 142 (2000) 74-85.

[84] S.E. Oswald, M.A. Spiegel, W. Kinzelbach, Three-dimensional saltwater-freshwater fingering in porous media: contrast agent MRI as basis for numerical simulations, Magn. Reson. Imaging 25 (2007) 537-540.

[85] M. Pervizpour, S. Pamukcu, H. Moo-Young, Magnetic Resonance Imaging of Hydrocarbon-Contaminated Porous Media, J. Comput. Civ. Eng. 13 (1999) 96-102.

[86] P.T. Callaghan, A.A. Khrapitchev, Time-dependent velocities in porous media dispersive flow, Magn. Reson. Imaging 19 (2001) 301–305.

[87] J.D. Seymour, J.P. Gage, S.L. Codd, R. Gerlach, Magnetic resonance microscopy of biofouling induced scale dependent transport in porous media, Adv. Water Resour. 30 (2007) 1408–1420.

[88] A.J. Sederman, M.L. Johns, P. Alexander, L.F. Gladden, Structure–flow correlations in packed beds, Chem. Eng. Sci. 53 (1998) 2117–2128.

[89] P. Swider, M. Conroy, A. Pedrono. D. Ambard, S. Mantell, K. Soballe, J.E. Bechtold, Use of high-resolution MRI for investigation of fluid flow and global permeability in a material with interconnected porosity, J. Biomech. 40 (2007) 2112–2118.

[90] M. Möble, S.-I. Han, W.R. Myers, S.K. Lee, N. Kelso, M. Hatridge, A. Pines, J. Clarke, SQUID-detected microtesla MRI in the presence of metal, J. Magn. Reson. 179 (2006) 146–151.

[91] J.A. Seeley, S.-I. Han, A. Pines, Remotely detected high-field MRI of porous samples, J. Magn. Reson. 167 (2004) 282-290.

[92] J. Granwehr, E. Harel, S.-I. Han, S. Garcia, A. Pines, Time-of-flight flow imaging using NMR remote detection, Phys. Rev. Lett. 95 (2005) 075503.

[93] S.-J. Xu, C.W. Crawford, S.M. Rochester, V.V. Yashchuk, D. Budker, A. Pines, Submillimeter-resolution magnetic resonance imaging at the Earth's magnetic field with an atomic magnetometer, Phys. Rev. A 78 (2008) 013404.

[94] I.I. Rabi, J.R. Zacharias, S. Millman, P. Kusch. A new method of measuring nuclear magnetic moment, Phys. Rev. 53 (1938) 318.

[95] I.I. Rabi, S. Millman, P. Kusch, and J.R. Zacharias. The molecular beam resonance method for measuring nuclear magnetic moments. Phys. Rev. 55 (1939) 526-535.

[96] H. Kauczor, R. Surkau, T. Roberts, MRI using hyperpolarized noble gases, Eur. Radiol. 8 (1998) 820–827.

[97] B.M. Goodson, Advances in magnetic resonance: Nuclear Magnetic Resonance of Laser-Polarized Noble Gases in Molecules, Materials, and Organisms, J. Magn. Reson. 155 (2002) 157-216.

[98] C.R. Bowers, D.P. Weitekamp, Para-hydrogen and synthesis allow dramatically enhanced nuclear alignment, J. Am. Chem. Soc. 109 (1987) 5541-5542.

[99] C.-G. Joo, K.-N. Hu, J.A. Bryant, R.G. Griffin, In situ temperature jump high-frequency dynamic nuclear polarization experiments: Enhanced sensitivity in liquid-state NMR spectroscopy, J. Am. Chem. Soc. 128, (2006) 9428-9432.

[100] B. Blumich, S. Anferova, R. Pechnig, H. Pape, J. Arnold, C. Clauser, Mobile NMR for porosity analysis of drill core sections, J. Geophys. Eng. 1 (2004) 177–180.

[101] T.Z. Teisseyre, J. Urban, N.W. Halpern-Manners, S.D. Chambers, V.S. Bajaj, F. Svec, A. Pines, Remotely detected NMR for the characterization of chromatographic separation using organic polymer monoliths, Anal. Chem. 83 (2011) 6004–6010.

[102] C.A. Meriles, D. Sakellarious, A.H. Trabesinger, V. Demas, A. Pines, Zero- to low-field MRI with averaging of concomitant gradient fields, Proc. Natl. Acad. Sci. USA. 102 (2005) 1840–1842.

[103] P.L. Volegov, J.C. Mosher, M.A. Espy, R.H. Kraus, On concomitant gradients in low-field MRI, J. Magn. Reson. 175 (2005) 103–113.

[104] W.R. Myers, M. Möble, J. Clarke, Correstion of concomitant gradient artifacts in experimental microtesla MRI, J. Magn. Reson. 177 (2005) 274–284.

[105] L.-S. Bouchard, Unidirectional magnetic-field gradients and geometric-phase errors during Fourier encoding using orthogonal ac fields, Phys. Rev. B 74 (2006) 054103-054107.

[106] J.O. Nieminen, R.J. Ilmoniemi, Solving the problem of concomitant gradients in ultra-low-field MRI, J. Magn. Reson. 207 (2010) 213–219.

[107] I. Savukov, T. Karaulanov, A. Castro, P. Volegov, A. Matlashov, A. Urbatis, J. Gomez, M. Espy, Non-cryogenic anatomic imaging in ultra-low field regime: hand MRI demonstration, J. Magn. Reson. 211 (2011) 101–108.

[108] D.A. Yablonskiy, A.L. Sukstanskii, J.J. Ackerman, Image artifacts in very low magnetic field MRI: the role of concomitant gradients, J. Magn. Reson. 174 (2005) 279-86.

[109] W.R. Myers, M. Mössle, J. Clarke, Correction of concomitant gradient artifacts in experimental microtesla MRI, J. Magn. Reson. 177 (2005) 274-84.

[110] A. Mohoric, J. Stepisnik, M. Kos, G. Planinsic, Self-diffusion imaging by spin echo in earth's magnetic field, J. Magn. Reson. 136 (1999) 22-26.

[111] S.K. Lee, M. Mobetale, W. Myers, N. Kelso, A.H. Trabesinger, A. Pines, J. Clarke, SQUID-detected MRI at 132 μT with *T*(1)-weighted contrast established at 10 μT–300 mT, Magn. Reson. Med. 53 (2005) 9-14.

[112] A.N. Matlachov, P.L. Volegov, M.A. Espy, J.S. George, R.H. Kraus, SQUID detected NMR in microTesla magnetic fields. J. Magn. Reson. 170 (2004) 1-7.

[113] S. Ruangchaithaweesuk, D.S. Yu, N.C. Garcia, L. Yao, S.-J. Xu, Applications of optically detected MRI for enhanced contrast and penetration in metal, J. Magn. Reson. 223 (2012) 20–24.

[114] I.M. Savukov, S.J. Selter, M.V. Romalis, Detection of NMR signals with a radiofrequency atomic magnetometer, J. Magn. Reson. 185 (2007) 227–233.

[115] D. Janasek, J. Franzke, A. Manz, Scaling and the design of miniaturized chemical-analysis systems, Nature, London, 442 (2006) 374-380.

[116] H. Song, H.-W. Li, M.S. Munson, T.G. Van Ha, R.F. Ismagilov, On-Chip Titration of an Anticoagulant Argatroban and Determination of the Clotting

Time within Whole Blood or Plasma Using a Plug-Based Microfluidic System, Anal. Chem. 78 (2006) 4839-4849.

[117] D. Sinton, Microscale flow visualization, Microfluid. Nanofluid. 1 (2004) 2-21.

[118] E. Harel, L. Schroder, S.-J. Xu, Novel detection schemes of nuclear magnetic resonance and magnetic resonance imaging: applications from analytical chemistry to molecular sensors, Annu. Rev. Anal. Chem. 1 (2008) 133-163.

[119] C. Yi, Q. Zhang, C.-W. Li, J. Yang, J. Zhao, M. Yang, Optical and electrochemical detection techniques for cell-based microfluidic systems, Anal. Bioanal. Chem. 384, (2006) 1259-1268.

[120] P.S. Dittrich, A. Manz, Single Fluorescent Molecule Spectroscopy in Microfluidics: the Holy Grail of μTAS, Anal. Bioanal. Chem. 382 (2005) 1771-1782.

[121] K.B. Mogensen, H. Klank, J.P. Kutter, Recent developments in detection for microfluidic systems, Electrophoresis 25 (2004) 3498-3512.

[122] D. Ross, L.E. Locascio, Effect of caged fluorescent dye on the electroosmotic mobility in microchannels, Anal. Chem. 75 (2003) 1218-1220.